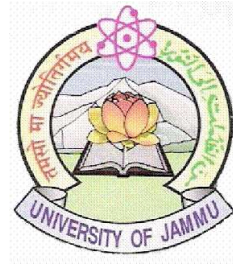


**A Study of Fluctuations in Multiplicity Distributions at Ultra-Relativistic
Heavy Ion Interactions.**



THESIS

Submitted to the University of Jammu

For the Award of the Degree of

DOCTOR OF PHILOSOPHY (Ph.D)

IN

PHYSICS

BY

NEERAJ GUPTA

P.G. Department of Physics and Electronics

University of Jammu

Jammu-180006

(INDIA)

April, 2008

THIS WORK IS
DEDICATED TO MY
LOVING
PARENTS

Certificate

I, hereby, declare that the matter embodied in this thesis is the result of investigations carried out by me in the Department of Physics, University of Jammu, Jammu, under the joint supervision of Prof. S. K. Badyal and Dr. Zubayer Ahammed. To the best of my knowledge, no part of this work has been submitted in part or full for the award of a degree in any other university.

Neeraj Gupta

Certified that:

1. the work embodied in this thesis entitled: “A Study of Fluctuations in Multiplicity Distributions at Ultra-Relativistic Heavy Ion Interactions” has been carried out by Mr. Neeraj Gupta under our joint supervision and is worthy of consideration for the award of Ph.D degree.
2. the candidate has put in the required attendance in the department during the period of research;
3. the conduct of the candidate remained satisfactory during the period of research.

Prof. S.K. Badyal

(Supervisor)

Dr. Zubayer Ahammed

(Co-supervisor)

Countersigned

Head of the Department

Acknowledgments

No body lives in complete isolation, and we accomplish nothing without the input and encouragements of those around us. Although I have asserted that the work presented in this thesis is entirely my own, it is a delight to acknowledge here the important contributions that many people have made over the past few years which have allowed me to get where I am today.

*At the onset, I take this opportunity to express my deep sense of gratitude and profound reverence to my esteemed supervisor **Prof. S. K. Badyal**, Professor in the Department of Physics, University of Jammu, for his innovative thought provoking and valuable guidance and keen supervision. I sincerely appreciate his constant involvement, easy accessibility, painstaking efforts, encouragement, ability to tackle most difficult of the problems and affectionate nature. I would like to record my debt of gratitude for the amiable and co-operative manner in which he tendered his fruitful assistance and contributions and made himself available whenever approached for the purpose. Time after time, his vast knowledge, deep insights, tremendous experience and easy grasp of physics at its most fundamental level helped me in the struggle for my own understanding. It was both a privilege and honour to work with him. I have learned various things, from him, such as the way of thinking and the way of proceeding in research and so on.*

*I am equally thankful to my co-supervisor **Dr. Zubayer Ahammed**, Scientist at Variable Energy Cyclotron Centre, Department of Atomic Energy, Kolkata. He helped me at each and every stage to complete this noble task. I really don't have the words to write about him. His in-depth knowledge and practical experiences about the experimental high energy physics field helped me not only in pursuing physics challenges which I*

came across during my research period but also helped me to initiate ideas and accomplish them successfully in my life.

I would like to express my sincere thanks to Dr. Timothy Hallman, spokesperson of STAR experiment for inviting me three times to visit Brookhaven National Laboratory, USA and fruitful scientific discussions. I would thank Dr. J. Lauret from BNL for valuable help related to STAR computing. I would also like to sincerely thank Dr. W. Christie, Dr. R. Brown, for valuable help during PMD maintenance and data taking at BNL. My sincere thanks are due to Dr. Aihong Tang and Prof. Garry Westfall for active participation in my physics analysis, fruitful suggestions and comments. I thank all the members of STAR Collaboration and the Indian PMD group for providing me an opportunity to work with them.

I express my sincere thanks to Prof. Bikash Sinha, Director of Variable Energy Cyclotron Centre (VECC) and Saha Institute of Nuclear Physics (SINP) for allowing me to do research at VECC and to use the facilities there.

My sincere thanks are due to Dr. Y. P. Viyogi, Director of Institute of Physics, Bhubaneswar for his constant encouragement, support, advice and useful suggestions whenever approached. I am especially thankful to him for his patient replies of my queries.

I express my sincere thanks to Dr. D. K. Srivastva, outstanding Scientist and Head of the Physics Group, VECC, Department of atomic energy, Kolkata for his valuable suggestions and help during my visit to VECC, Kolkata.

My regardful thanks are due to Prof. Naresh Padha, Head of the Physics Department, University of Jammu, Jammu for providing me the necessary infrastructure, help, support and other facilities during my tenure of research.

My sincere thanks also due to Prof. L.K. Mangotra (P.I. ALICE Project), Prof. V.K. Gupta, Prof. Anju Bhasin, Er. Anik Gupta, Dr. P.V.K.S Baba, Dr. S.S. Sambyal, Er. Sanjay Mahajan, Dr. Saroj Nayak and Dr. Ramni Gupta for their valuable help and suggestions during the entire tenure of research.

I am also thankful to Prof. S.K. Khosa, Prof. Rajnikant and Dr. Arun Bharti for his encouragement, good wishes and kind help whenever I approached.

I owe my grateful thanks to Dr. Subhasis Chattopadhyay Scientists at Variable Energy Cyclotron Centre, Kolkata for his fruitful discussion and encouragement.

I would also like to thanks Dr. Tapan Kumar Nayak, Dr. Bedangas Mohanty, Mr. G.S. Murthy, Mr. R.N. Singaraju, Mr. Sushant Pal, Dr. Anand Kumar Dubey and Mr. Vikas Singhal , Scientists at Variable Energy Cyclotron Centre, Kolkata for their kind support, analysis discussion, suggestion and encouragement throughout my research period.

I acknowledge Prof. M.M. Aggarwal and Prof. A.K. Bhatti of Panjub University for our good time together at BNL, USA. It was really a enjoyable and nice experience to work with them. I extend my sincere thanks to Dr. Sudhir Raniwala and Dr. Rashmi Raniwala of Rajasthan University, Dr. D.P. Mahapatra, Dr. S.C. Phatak of Institute of Physics, Bhubaneshwar, Prof. R. Varma and Prof. B.K. Nandi of IIT Mumbai for

their nice suggestions, comments and positive criticism during the collaboration meetings helped me a lot to improve my physics analysis.

I express my sincere thanks to Prof. Mohd. Irfan, Dr. Shakeel Ahmed, Dr. Nazeer Ahmed and Dr. Mohsin Khan for providing nice suggestions, guidance and blessings.

My Sincere thanks to Dr. T.H. Shah, Dr. Farooq Mir, Dr. Sunil Dutt, Dr. Rani Devi and Dr. Anita Sharma for their constant encouragement, helpful suggestions, guidance and caring attitudes.

I have special words of appreciation and praise for Mrs. Kalpana Kesar for her concern, blessings, encouragement and moral support during the entire research period.

I thank DST sponsored ALICE project for providing scholarship as well as travel support for visits to attend national and international conferences, collaborating institutes and collaborative research work.

My profound appreciation and sincere thanks are also due to my close friends especially, Mr. Sanjay Sharma, Mr. Neeraj Kohli, Mr. Mohd Aezaz, Prof. Rawan Kumar, Dr. Parvaiz Dar, Mr. S. Abass Khan, Mr. Vivek Chalotra, Mr. Vinod Joshi, Mr. Narinder Sharma, Mr. Rajneesh Sharma, and Miss Amarjeet Kour, for constant encouragement, nice company, suggestions and all the care and affection showered on me.

I heartily thankful to Miss Aarti Manhas for her nice company, inspirations, always caring and loving attitudes. She always encouraging me whenever I got disappointed.

My sincere thanks are due to my colleagues, Dr. Renu Balla, Mr. Chaman Lal, Mr. Surjeet Singh, Mr. Satish Sharma, Mr. S.M. Dogra, Miss Anita Mahajan, Miss Anju Kumari, Mr. Ranveer Singh, Mr. Joginder Singh, Mr. Qasim Mir, Mr. Mohd. Irshad, Miss. Saiqa Sadiq and Mr. Shikshit Gupta.

I gratefully acknowledge the technical staff of our high energy physics for their kind co-operation and healthy atmosphere in the section during my research period.

A word of appreciation and thanks to Sh. Rattan Lal chowkidar of physics department for his dedication, sincerity and services rendered by him during the course of my research work.

I fail to find words to express my sincere gratitude to my parents for their continuous encouragement, sacrifice blessings, support, unremitting co-operation, unparalleled inspirations and tireless efforts provided by them all the time without which it would not have been possible for me to complete this noble task. I am equally thankful to my Dear Jija ji and and my loving sister for their blessing, encouragement and kind help.

Last but not the list, I owe my special thanks to all who helped me directly or indirectly to accomplish this task. I expect to be pardoned if I have missed any such name inadvertently.

(Neeraj Gupta)

List of Publications

(1) ρ^0 photoproduction in Ultra-Peripheral Relativistic Heavy Ion Collisions at $\sqrt{S_{NN}} = 200$ GeV.

STAR Collaboration (B.I. Abelev et al.).

Phys. Rev. C 77 (2008) 34910.

(2) Measurement of transverse single-spin asymmetries for di-jet production in proton-proton collisions at $\sqrt{S_{NN}} = 200$ GeV.

STAR Collaboration (B.I. Abelev et al.).

Phys.Rev.Lett.99:142003,2007.

(3) Global polarization measurement in Au+Au collisions.

STAR Collaboration (B.I. Abelev et al.).

Phys.Rev.C76:024915,2007.

(4) Energy dependence of π^+ , π^- , p and anti-p transverse momentum spectra for Au+Au collisions at $\sqrt{S_{NN}} = 62.4$ and 200 GeV.

STAR Collaboration (B.I. Abelev et al.).

Phys.Lett.B655:104-113,2007.

(5) Partonic flow and phi-meson production in Au + Au collisions at $\sqrt{S_{NN}} = 200$ GeV.

STAR Collaboration (B.I. Abelev et al.).

Phys.Rev.Lett.99:112301,2007.

(6) Mass, quark-number, and $\sqrt{S_{NN}}$ dependence of the second and fourth flow harmonics in ultra-relativistic nucleus-nucleus collisions.

STAR Collaboration (B.I. Abelev et al.).

Phys.Rev.C75:054906,2007.

(7) Rapidity and species dependence of particle production at large transverse momentum for d+Au collisions at $\sqrt{S_{NN}} = 200$ GeV.

STAR Collaboration (B.I. Abelev et al.).

Phys.Rev.C76:054903,2007.

(8) Longitudinal double-spin asymmetry and cross section for inclusive jet production in polarized proton collisions at $\sqrt{S_{NN}} = 200$ GeV.

STAR Collaboration (B.I. Abelev et al.).

Phys.Rev.Lett.97:252001,2006.

(9) Neutral kaon interferometry in Au+Au collisions at $\sqrt{S_{NN}} = 200$ GeV.

STAR Collaboration (B.I. Abelev et al.).

Phys.Rev.C74:054902,2006.

(10) Strange particle production in p+p collisions at $\sqrt{S_{NN}} = 200$ GeV.

STAR Collaboration (B.I. Abelev et al.).

Phys.Rev.C75:064901,2007.

(11) Transverse momentum and centrality dependence of high-p(T) non-photonic electron suppression in Au+Au collisions at $\sqrt{S_{NN}} = 200$ GeV.

By STAR Collaboration (B.I. Abelev et al.).

Phys.Rev.Lett.98:192301,2007.

(12) Delta phi Delta eta Correlations in Central Au+Au Collisions at $\sqrt{S_{NN}} = 200$ GeV.

Star Collaboration (J. Adams et al.).

Phys.Rev.C75:034901,2007.

(13) The Multiplicity dependence of inclusive p(t) spectra from p-p collisions at $\sqrt{S_{NN}} = 200$ GeV.

STAR Collaboration (J. Adams et al.).

Phys.Rev.D74:032006,2006.

(14) Scaling Properties of Hyperon Production in Au+Au Collisions at $\sqrt{S_{NN}} = 200$ GeV.

STAR Collaboration (J. Adams et al.).

Phys.Rev.Lett.98:062301,2007.

*(15) Energy and system size dependence of photon production at forward rapidities at RHIC.

Monika Sharma (Panjab Univ.) , Sunil Dogra, Neeraj Gupta (Jammu Univ.).

Int.J.Mod.Phys.E16:1845-1851,2007.

(16) Identified baryon and meson distributions at large transverse momenta from Au+Au collisions at $\sqrt{S_{NN}} = 200$ GeV.

STAR Collaboration (B.I. Abelev et al.).

Phys.Rev.Lett.97:152301,2006.

(17) The Energy dependence of p(t) angular correlations inferred from mean-p(t) fluctuation scale dependence in heavy ion collisions at the SPS and RHIC.

STAR Collaboration (J. Adams et al.).

J.Phys.G33:451-466,2007.

(18) Strange baryon resonance production in $\sqrt{S_{NN}} = 200$ GeV p+p and Au+Au collisions.

STAR Collaboration (John Adams et al.).

Phys.Rev.Lett.97:132301,2006.

(19) Direct observation of dijets in central Au+Au collisions at $\sqrt{S_{NN}} = 200$ GeV.

STAR Collaboration (J. Adams et al.).

Phys.Rev.Lett.97:162301,2006.

(20) Forward neutral pion production in p+p and d+Au collisions at $\sqrt{S_{NN}} = 200$ GeV.

STAR Collaboration (John Adams et al.).

Phys.Rev.Lett.97:152302,2006.

(21) Identified hadron spectra at large transverse momentum in p+p and d+Au collisions at $\sqrt{S_{NN}} = 200$ GeV.

STAR Collaboration (John Adams et al.).

Phys.Lett.B637:161-169,2006.

(22) Strangelet search at RHIC.

STAR Collaboration (B.I. Abelev et al.).

Phys.Rev.C76:011901,2007.

(23) Multiplicity and pseudorapidity distributions of charged particles and photons at forward pseudorapidity in Au + Au collisions at $\sqrt{S_{NN}} = 62.4$ GeV.

STAR Collaboration (John Adams et al.).

Phys.Rev.C73:034906,2006.

(24) Proton - lambda correlations in central Au+Au collisions at $\sqrt{S_{NN}} = 200$ -GeV.

STAR Collaboration (John Adams et al.).

Phys.Rev.C74:064906,2006.

(25) Directed flow in Au+Au collisions at $\sqrt{S_{NN}} = 62$ GeV.

STAR Collaboration (John Adams et al.).

Phys.Rev.C73:034903,2006.

(26) Transverse-momentum p(t) correlations on (eta, phi) from mean-p(t) fluctuations in Au-Au collisions at $\sqrt{S_{NN}} = 200$ GeV.

STAR Collaboration (John Adams et al.).

J.Phys.G32:L37-L48,2006.

Paper Presented in Conferences/Symposiums

*(1) Systematic Study of Photon Production in Cu+Cu interactions at $\sqrt{S_{NN}} = 62.4$ GeV in the STAR Experiment at RHIC.

Neeraj Gupta (STAR Collaboration).

Presented in the DAE Nuclear Physics Symposium at M.S. University of Baroda, India 2006.

*(2) Kaon to Pion Ratio Fluctuation on an Event by Event Basis in Cu+Cu Interactions in the STAR Experiment at RHIC.

Neeraj Gupta and Zubayer Ahammed (STAR Collaboration).

Presented in the DAE Nuclear Physics Symposium at M.S. University of Baroda, India 2006.

*(3) Event by Event Fluctuations in K/π ratio in the STAR Experiment at RHIC.

Neeraj Gupta and Zubayer Ahammed (STAR Collaboration).

Presented in the DAE High Energy Physics Symposium at IIT Khargpur, India 2006.

*(4) Systematic Study of Photon Production At Forward Rapidity in STAR.

Neeraj Gupta (STAR Collaboration)

Presented in the International Conference on Nucleus-Nucleus Collision (Quark Matter), 2008. Jaipur, India.

* Results from these are included in this thesis.

SYNOPSIS

From the onset of the formulation of the quark model and the first understanding of the nature of the binding and confining potential between quarks about 30 years ago it has been conjectured that a state of matter characterized by a large density of quarks and gluons (together called partons) might be created for a fleeting moment after the birth of the universe. This high energy density state would be characterized by a strongly reduced interaction between its constituents, the partons, such that these would exist in a nearly free state. This proposed state of matter has been designated as Quark-Gluon plasma (QGP) phase. It is now been generally thought that the early universe was initially in a QGP state until its energy density had decreased sufficiently as a result of the expansion of the universe, that it could make the transition to ordinary (confined) matter.

The only way of studying matter under extreme conditions of density and temperature which may consequently lead to the deconfined state of matter (Quark-Gluon Plasma) is to organise ultra-relativistic heavy-ion collisions. Such experimental facilities are available at various accelerator sites of the world, notable among them are Nuclear Research Center (CERN) Geneva and Brookhaven National Laboratory (BNL) USA. Variety of ultra-relativistic ion beams have been used for high energy physics experimentation. A wide spectrum in energy, charge, mass, projectile and target systems have been studied using various analysis techniques. The experimental data has been analyzed and interpreted in literature in terms of various physics variables and correlations functions. A large number of Monte Carlo (MC) based simulation models, are available to help interpretation of experimental data.

One of the signal of Quark-Gluon Plasma (QGP) phase transition could be a strong

modification in the fluctuations of specific observables measured on event-by-event basis in a collision. Enhanced production of strangeness has been predicted to be a signature of phase transition and has been observed through kaon to pion ratio at CERN SPS and RHIC BNL energies. Here, we present event-by-event fluctuations in K/π ratio for central Cu+Cu interactions at $\sqrt{S_{NN}} = 62.4$ and 200 GeV recorded by Time Projection Chamber (TPC) in STAR experiment at RHIC, BNL, USA. Time Projection Chamber in STAR experiment records the tracks of particles, measures their momenta and identifies the particles by measuring their ionization energy loss. TPC acceptance covers ± 1.8 units of pseudorapidity with full azimuthal coverage. In STAR experiment, TPC is placed inside a large solenoidal magnet designed with a uniform maximum field of 0.5 T. The TPC is a fully pixelized drift chamber with Multi-Wire Proportional Chambers (MWPC) at both ends for readout. There are 136,608 readout pads. These pads provide x and y coordinate information and upto 512 time buckets which provide z-position information for each hit. The TPC is a gas detector having 10% methane and 90% argon. Using particle identification by the energy loss (dE/dx) of the produced particle in the STAR Time Projection Chamber (TPC), the ratio of kaons and pions is determined.

Important information about the dynamics of particle production and the evolution of the system formed in the ultra-relativistic heavy-ion collisions can be obtained from various global observables, such as the multiplicity and pseudorapidity distribution of produced particles. Multiplicity distributions have been used to understand the particle production mechanism based on participant scaling, and recently by invoking the Color Glass Condensate (CGC) model. Various studies have been undertaken on the measurements of charged particles produced in heavy-ion collisions covering complete pseudorapidity region, but very limited measurements are available for photons multiplicity distributions in the forward rapidity region. The only measurements of photon

multiplicity distributions in the forward rapidity region reported to date are from a preshower detector (WA93, WA98 experiment) at the Super Proton Synchrotron (SPS) at CERN, and Solenoidal Tracker (STAR) at relativistic heavy-ion collider (RHIC) at Brookhaven National Laboratory (BNL), USA. The photons are considered as one of the most valuable probes of the dynamics and properties of the matter formed in the heavy-ion collisions as they interact only electromagnetically. Photons have a large mean free path and hence carry the first hand information of their origin. Here, pseudorapidity distributions of photon multiplicity are studied in Cu+Cu interactions at $\sqrt{S_{NN}} = 62.4$ GeV. The data was recorded in Photon Multiplicity Detector (PMD) in STAR experiment in the forward rapidity region $2.3 \leq \eta \leq 3.8$.

The Photon Multiplicity Detector (PMD) is one of the detector of hybrid STAR experiment located at 5.4 meters away from the center of the Time Projection Chamber (TPC) along the beam axis. PMD consists of two planes one is charged particle veto and second is preshower plane of an array of cellular gas proportional counters using *Ar* and *CO*₂ gas mixture. A lead plate of three radiation length thickness placed between the two planes is used as photon converter. A photon produces an electromagnetic shower on passing through the lead converter. These shower particles produce signals in several cells of the sensitive volume of the detector. Charged hadrons usually affect only one cell and produce a signal resembling those of Minimum Ionizing particles (MIP).

The thesis includes the measurement of event-by-event fluctuations in the kaon to pion (K/π) ratio in central Cu+Cu interactions at $\sqrt{S_{NN}} = 62.4$ and 200 GeV recorded by Time Projection Chamber (TPC) and systematic studies of photon multiplicity distribution and their fluctuations at $\sqrt{S_{NN}} = 62.4$ GeV in the forward rapidity $2.3 \leq \eta \leq 3.8$ region recorded by Photon Multiplicity Detector (PMD) in STAR experiment at BNL,

USA. The thesis comprises six chapters in the following scheme.

In the first chapter titled as Introduction, a brief overview of the subject matter is presented. The goals of high energy physics are outlined. The Standard Model, possibilities of recreation of the Quark-Gluon Plasma (QGP) phase transitions and space time evolution of heavy-ion collisions are presented. Various projected signals of QGP are presented along with their theoretical as well as experimental status at CERN, SPS and BNL, RHIC energies. Gauging of fluctuations in multiplicity distributions which form core of experimental data analysis is discussed. The scientific plan of the studies to segregate the fluctuations of dynamic origin is presented.

In second chapter the experimental details about the STAR experiment setup and its operation at Relativistic Heavy-Ion Collider (RHIC) at Brookhaven National Laboratory (BNL), USA are discussed. The STAR experimental setup consists of several types of detectors, each specializing in detecting certain types of particles or characterizing their motion. These detectors work together in an advanced data acquisition and subsequent physics analysis that allows final statements to be made about the collision.

Third chapter of the thesis is devoted to the description of Photon Multiplicity Detector (PMD) as part of STAR experiment. The principal of operation, hardware details, fabrication and quality control parameters of data are discussed. The STAR simulation framework used in the context of PMD is also outlined.

The fourth chapter of the thesis comprise the analysis of data on event-by-event basis for fluctuations in the kaon to pion (K/π) ratio for central Cu+Cu interactions at $\sqrt{s_{NN}} = 62.4$ and 200 GeV. Results are discussed, based on two different measures of fluctua-

tions providing information on dynamical fluctuations after correcting for the statistical component. The statistical fluctuations are estimated using mixed event technique. The fluctuations strength measured by the quantity called $\nu_{dynamic}$ is also discussed. The centrality and energy dependence of fluctuations strength and comparison with theoretical model predictions are described. An attempt also has been made to compare the observed K/π dynamical fluctuations in central Cu+Cu system with the measurements of NA49 collaboration in the central Pb+Pb interactions at $\sqrt{S_{NN}} = 6.3, 7.6, 8.8, 12.3$ and 17.3 GeV and with the earlier measurements of STAR collaboration in central Au+Au interactions at $\sqrt{S_{NN}} = 20, 62.4, 130$ and 200 GeV.

The data analysis in central Cu+Cu interactions at $\sqrt{S_{NN}} = 62.4$ GeV in the forward rapidity $2.3 \leq \eta \leq 3.8$ are presented in the fifth chapter. Photon pseudorapidity distributions as a function of collision centrality are presented. The observed experimental pseudorapidity distributions of photons are compared with the results obtained from theoretical model (HIJING). The limiting fragmentation hypothesis has been examined for photon multiplicities. Chapter also includes photon fluctuations measurements using $\nu_{dynamic}$ variable through sub-event method.

In chapter sixth results from the data analysis are summarised. The kaon to pion ratio (K/π) fluctuations in terms of variable σ_{dyn} for TPC data (Au+Au and Cu+Cu interactions at RHIC energies) is not observed to show any definite trend or variation. This observation is however in contrast with NA49 experiment results at low energies. The data are in agreement with Torrieri statistical hadronization model fitted with $\gamma_q > 1$. The variable $\nu_{dyn}(K\pi)$ shows inverse dependence on impact parameter. Similar observations are made in the context of pseudorapidity density ($dN/d\eta$) parameter. This behaviour is observed to be independent of the energy and mass value of the colliding

nuclei. A Multiphase Transport (AMPT) code which takes care of rescatterings can reasonably reproduce the experimental results. Interesting behaviour of scaled parameters is discussed.

The photon multiplicity per participant in the experimental data is compared with the predictions from model. HIJING model reproduces experimental results for high centrality events. The limiting fragmentation behaviour has been examined for the data. The fluctuations in the multiplicity distributions are studied with variable ν_{dyn} using sub-event method. Results on scaling properties of parameters have been examined.

(Neeraj Gupta)

Contents

1	Introduction	1
1.1	Introduction	1
1.2	Quantum Chromodynamics (QCD) and Phase Transition	5
1.3	Space Time Evolution	9
1.4	The Bag Model	13
1.5	Quark Gluon Plasma (QGP) and its Signatures	13
1.5.1	Transverse Momentum Distribution	14
1.5.2	Photons and Dileptons Production	16
1.5.3	Suppression of the J/Ψ Production	18
1.5.4	Fluctuations and Correlations	22
1.5.5	Jet Quenching	26
1.5.6	Flow	27
1.5.7	Production of Strange Particles	29
1.6	Rapidity and Pseudorapidity Variables	33
1.7	Theoretical Models in Relativistic Heavy-Ion Collisions	35
1.7.1	Heavy-Ion Jet Interaction Generator (HIJING) Model	35
1.7.2	A Multi-Phase Transport (AMPT) Model	36
1.8	Statement of the Problem	37

2	STAR Experiment at RHIC	44
2.1	Relativistic Heavy-Ion Collider (RHIC)	44
2.2	Different Experiments at RHIC	47
2.2.1	PHOBOS Experiment	49
2.2.2	PHENIX Experiment	49
2.2.3	BRAHMS Experiment	50
2.3	STAR Experiment	51
2.3.1	Objectives of STAR	51
2.3.2	STAR Magnet	52
2.4	STAR's Detector	54
2.4.1	Time Projection Chamber (TPC)	54
2.4.1.1	Design of TPC	56
2.4.1.2	Hit Resolution and Tracking Efficiency	59
2.4.1.3	Vertex and Momentum Resolution	61
2.4.1.4	Particle Identification	62
2.4.2	Silicon Vertex Tracker (SVT)	64
2.4.3	Forward Time Projection Chamber (FTPC)	65
2.4.4	Silicon Strip Detector (SSD)	66
2.4.5	Zero Degree Calorimeter (ZDC)	66
2.4.6	Central Trigger Barrel (CTB)	67
2.4.7	Barrel Electromagnetic Calorimeter (BEMC)	68
2.4.8	Beam Beam Counter (BBC)	68
2.4.9	Photon Multiplicity Detector (PMD)	69
2.5	Data Acquisition System (DAQ) and Triggering in STAR	70
2.6	Collision Centrality Selection in STAR	70

3	Photon Multiplicity Detector (PMD)	77
3.1	Introduction	77
3.2	Physics Goals of STAR PMD	78
3.3	Working Principle of PMD	79
3.4	Designing and construction of PMD	81
3.4.1	Detector and its components	83
3.4.2	Support Structure of PMD	89
3.4.3	PMD Electronics and Readout	89
3.4.4	Trigger and Data Acquisition	93
3.5	PMD Gas System	94
3.6	Detector Performance	96
3.6.1	Response to Charged Particles	96
3.6.2	Preshower Characteristics	98
3.7	Photon Clustering	100
3.8	STAR Simulation	103
4	Event-by-Event Fluctuations in Kaon to Pion ratio (K/π) at RHIC	109
4.1	Introduction	109
4.2	Earlier Measurements and Motivation	110
4.3	Data Analysis	113
4.3.1	Data Set Used	113
4.3.2	Data Quality Cuts	113
4.4	Dynamical Fluctuations in Cu+Cu	115
4.4.1	Comparison with NA49 (SPS) and Au+Au (STAR RHIC)	118
4.4.2	Comparison with Statistical Hadronization Model	123
4.5	$\nu_{dyn}(K\pi)$ Variable Study in Cu+Cu	123
4.5.1	Comparison with Au+Au (STAR) and NA49 (SPS)	128

4.5.2	$\nu_{dyn}(K\pi)$ Variable Study From Theoretical Model	130
4.5.3	$\nu_{dyn}(K\pi)$ Comparison with HIJING and AMPT Model	132
4.5.4	$\nu_{dyn}(K\pi)$ for Same and Opposite signs	132
4.5.5	$\nu_{dyn}(K\pi)$ Scaled results	133
5	Photon Multiplicity Distributions in Forward Rapidity Region	142
5.1	Introduction	142
5.2	Some Earlier measurements	144
5.3	Preshower Configuration During Data Taking	146
5.4	Data Set Selection for Analysis	146
5.5	Discrimination and Gain Calibration	148
5.6	Efficiency and Purity	150
5.7	Detector Acceptance Factor	151
5.8	Photon Multiplicity Distributions	153
5.8.1	Centrality Wise Photon Pseudorapidity Distributions	156
5.8.2	Comparison with Model Predictions (HIJING)	157
5.8.3	Photon Production as a function of N_{Part}	159
5.8.4	Limiting Fragmentation in Photon Production	159
5.8.5	Fluctuations in Photon Production	162
6	Conclusions	171
6.1	Event-by-Event K/π Ratio Fluctuations	171
6.2	Photon Pseudorapidity Distributions	173
6.3	Summary	174

List of Figures

1.1	Shows the hallmarks in the development of energy-mass conversion, nucleonic synthesis, neutral bulk matter etc. after the Big Bang in relevant time and temperature scenario.	4
1.2	A schematic phase diagram of nuclear matter. Heavy-Ion collisions at Relativistic Heavy Ion Collider (RHIC) are thought to be at low baryon chemical potential and temperatures greater than or equal to 170 MeV.	8
1.3	The possible scenario for a relativistic heavy-ion collision evolution.	11
1.4	Schematic behaviour of the average transverse momentum ($\langle P_t \rangle$) as a function of the energy density for matter in the hadronic phase, in a transition region and in the Quark-Gluon Plasma phase	15

1.5	The invariant direct-photon multiplicity as a function of the transverse momentum (P_t) in central Pb+Pb interactions at 17.2 GeV. The figure is taken from [11]. The errors bars indicate the combined statistical and systematic uncertainties. The data points with downward arrows indicate unbounded 90% CL limits on the direct photon yield. The WA98 data points are compared with scaled p+p, p+C results, pQCD calculation and scaled parametrization of direct-photon yields in p+p collisions.	19
1.6	The anomalous suppression as a function of the energy density reached in the collision for different experiments. Suppression is obtained from the measured cross-sections divided by the values expected from nuclear absorption. It is observed that in Pb+Pb interactions J/Ψ is suppressed normally, i.e. according to pure nuclear absorption, for energy densities lower than $2.2 \text{ GeV}/fm^3$. For higher density values, a peculiar abnormal suppression pattern is observed, as can be expected from charmonium due to deconfinement.	20
1.7	The Comparison between the NA50 Pb+Pb data and several conventional calculations of J/Ψ suppression.	21
1.8	Energy dependence of the event-by-event dynamical fluctuations from K/π ratio in Pb+Pb collisions studied by NA49 experiment at SPS. The systematic errors of the measurements are shown as grey bands.	25

1.9	Elliptic Flow (v_2) coefficient for all charged particles measured by STAR and PHENIX in minimum bias Au+Au collisions at 130 GeV and compared to hydrodynamical calculations corresponding to equations of state (EOS) with (Q) and without (H) phase transition [57].	28
1.10	Hyperon and anti-Hyperon yields per number of wounded nucleons, expressed in units of corresponding yield per collision in p-Be reactions, measured at SPS 17.3 GeV by NA57.	31
1.11	Mid-rapidity K/π ratio versus $\sqrt{S_{NN}}$. The curves are parameterizations to $p + p$ data [66]. The error are statistical.	33
2.1	Aerial view of Brookhaven National Laboratory (BNL), Upton, New-York, USA.	46
2.2	The Relativistic Heavy Ion Collider (RHIC) accelerator complex at Brookhaven National Laboratory. Nuclear beams are accelerated from the Tandem Van de Graaff, through the transfer line into the AGS Booster and AGS prior to injection into RHIC.	48
2.3	Schematic view of the STAR detector at Relativistic Heavy-Ion Collider (RHIC), BNL, USA.	53
2.4	Schematic view and positions of different detectors in STAR experiment.	55
2.5	The STAR Time Projection Chamber (TPC) surrounds a beam-beam interaction region at RHIC. The collisions take place near the center of the TPC.	57
2.6	Particles identification in STAR Time Projection Chamber (TPC).	63

2.7	Beam’s eye view of a central event in the STAR Time Projection Chamber (TPC). This event was drawn by the STAR level 3 online display.	71
2.8	The minimum-bias distribution of the charge particles for Cu+Cu collisions at $\sqrt{s_{NN}} = 62.4$ and 200 GeV. The arrows represent the various centrality classes.	73
3.1	Schematic view and Position of Photon Multiplicity Detector in STAR relative to central detector TPC. The PMD is located at 540 cm from vertex and kept outside the STAR magnet.	80
3.2	The working principle of Photon Multiplicity Detector.	82
3.3	(a) Unit cell schematic with cross-section showing the dimensions and the cathode extension, (b) Layout of the STAR PMD. Thick lines indicate supermodule boundaries. There are 12 supermodules each in the preshower plane and the veto plane. Divisions within a supermodule denote unit modules.	84
3.4	Components of a unit module: Copper honeycomb, placed between two PCBs. The top PCB is seen with connectors and a FEE board. The cathode extension on the inside of the bottom PCB and the island separating the anode wire with the cathode is visible through the honeycomb. The photograph was taken with unassembled components.	86
3.5	Schematic cross-section of a supermodule showing the boundary walls, gas flow channels, high voltage connection and gas-tight sealings.	88

3.6	PMD support structure mechanism. The inner hexagonal part shows the two halves joined during data taking operation. The two halves, when separated for servicing, look as shown on the right and left.	90
3.7	Front-End Electronics (FEE) board with four GASSIPLEX chips.	92
3.8	(a) Pedestal Minimum values (in mV) for 5000 chips and (b) pedestal minimum vs. pedestal spread for these chips. Lines are drawn to suggest the grouping of chips for a uniform chain.	93
3.9	Schematic layout of Gas system for Photon Multiplicity Detector (PMD) in STAR experiment.	95
3.10	(a) Typical MIP spectra for cells with -1500 V, fitted with Landau distribution, (b) Distribution of the number of cells hit by MIP, it is seen that MIP is contained mostly in one cell.	97
3.11	Distribution of gain (top) and efficiency (bottom) for randomly selected 40 cells from the prototype chamber.	99
3.12	(left panel) Typical cluster size for preshower expressed in terms of the cells affected by electron, (right panel) filled circles represent energy deposition (in terms of cluster ADC) spectra for electrons with three energies, open circles represent the simulated energy deposition (in KeV) for electrons with corresponding energies. Width of simulated spectra is smaller compared to test data.	100
3.13	Flow chart showing the steps in generating simulated events. . .	104
3.14	Layout of Photon Multiplicity Detector (PMD) in GSTAR framework.	106

4.1	The multiplicity distributions for real and mixed events for Cu+Cu interactions at $\sqrt{S_{NN}} = 62.4$ GeV. The mean multiplicity values for both data and mixed events are in close agreement.	119
4.2	The multiplicity distributions for real and mixed events for Cu+Cu interactions at $\sqrt{S_{NN}} = 200$ GeV. The mean multiplicity values for both data and mixed events are in close agreement.	120
4.3	The event-by-event k/π ratio for Cu+Cu interactions at $\sqrt{S_{NN}} = 62.4$ GeV compared with the same quantity calculated from mixed events.	121
4.4	The event-by-event k/π ratio for Cu+Cu interactions at $\sqrt{S_{NN}} = 200$ GeV compared with the same quantity calculated from mixed events.	122
4.5	Measured dynamical K/π fluctuations in terms of σ_{dyn} for central Cu+Cu interactions at $\sqrt{S_{NN}} = 62.4$ and 200 GeV and compared with the earlier measurements as a function of beam energy. . .	124
4.6	The measured dynamical K/π fluctuations in terms of σ_{dyn} for central Cu+Cu interactions at $\sqrt{S_{NN}} = 62.4$ and 200 GeV compared with results from NA49, STAR Au+Au and statistical hadronization (SH) model.	125
4.7	The measured dynamical K/π fluctuations in terms of $\nu_{dyn}(K\pi)$ for Cu+Cu interactions at $\sqrt{S_{NN}} = 62.4$ and 200 GeV as a function of number of participating nucleons (N_{part}). The solid line is drawn from fit function $a+b/N_{part}$	129

4.8	The measured dynamical K/π fluctuations in terms of $\nu_{dyn}(K\pi)$ for Cu+Cu interactions at $\sqrt{S_{NN}} = 62.4$ and 200 GeV as a function of pseudorapidity density ($dN/d\eta$). The solid line is drawn from fit function $c+d/dN/d\eta$	129
4.9	The measured dynamical K/π fluctuations in terms of $\nu_{dyn}(k\pi)$ for Cu+Cu interactions at $\sqrt{S_{NN}} = 62.4$ and 200 GeV as a function of pseudorapidity density ($dN/d\eta$) and their comparison with STAR Au+Au and NA49 Pb+Pb results.	130
4.10	Shows the measured dynamical K/π fluctuations in terms of $\nu_{dyn}(K\pi)$ for Cu+Cu interactions at $\sqrt{S_{NN}} = 62.4$ and 200 GeV as a function of number of participating nucleons (N_{part}) from theoretical model (HIJING).	131
4.11	Shows the measured dynamical K/π fluctuations in terms of $\nu_{dyn}(K\pi)$ for Cu+Cu interactions at $\sqrt{S_{NN}} = 62.4$ and 200 GeV as a function of pseudorapidity density ($dN/d\eta$) from theoretical model (HIJING).	131
4.12	The measured dynamical K/π fluctuations in terms of $\nu_{dyn}(K\pi)$ for Cu+Cu interactions at $\sqrt{S_{NN}} = 62.4$ and 200 GeV as a function of pseudorapidity density ($dN/d\eta$) compared with HIJING and AMPT Model.	132
4.13	Measured dynamical K/π fluctuations in terms of $\nu_{dyn}(K\pi)$ for Cu+Cu interactions at $\sqrt{S_{NN}} = 62.4$ GeV for different combinations as a function of pseudorapidity density ($dN/d\eta$) from real data.	134

4.14 Measured dynamical K/π fluctuations in terms of $\nu_{dyn}(K\pi)$ for Cu+Cu interactions at $\sqrt{S_{NN}} = 200$ GeV for different combinations as a function of pseudorapidity density ($dN/d\eta$) from real data.	134
4.15 Shows the measured dynamical K/π fluctuations in terms of $\nu_{dyn}(K\pi)$ for Cu+Cu interactions at $\sqrt{S_{NN}} = 62.4$ GeV for different combinations as a function of pseudorapidity density ($dN/d\eta$) from HIJING.	135
4.16 Shows the measured dynamical K/π fluctuations in terms of $\nu_{dyn}(K\pi)$ for Cu+Cu interactions at $\sqrt{S_{NN}} = 200$ GeV for different combinations as a function of pseudorapidity density ($dN/d\eta$) from HIJING.	135
4.17 Measured dynamical K/π fluctuations in terms of $\nu_{dyn}(K\pi)$ for Cu+Cu interactions at $\sqrt{S_{NN}} = 62.4$ and 200 GeV scaled with pseudorapidity density ($dN/d\eta$) and their comparison with Au+Au study as a function of pseudorapidity density ($dN/d\eta$).	136
4.18 Measured dynamical K/π fluctuations in terms of $\nu_{dyn}(K\pi)$ for Cu+Cu interactions at $\sqrt{S_{NN}} = 62.4$ and 200 GeV scaled with pseudorapidity density ($dN/d\eta$) and their comparison with HIJING and AMPT model as a function of pseudorapidity density ($dN/d\eta$).	136
4.19 Measured dynamical K/π fluctuations in terms of $\nu_{dyn}(K\pi)$ for Cu+Cu interactions at $\sqrt{S_{NN}} = 62.4$ GeV scaled with pseudorapidity density ($dN/d\eta$) for K/π , K^+/π^+ , K^-/π^- , K^+/π^- , K^-/π^+ as a function of pseudorapidity density ($dN/d\eta$).	137

4.20	Measured dynamical K/π fluctuations in terms of $\nu_{dyn}(K\pi)$ for Cu+Cu interactions at $\sqrt{S_{NN}} = 200$ GeV scaled with pseudorapidity density ($dN/d\eta$) for K/π , K^+/π^+ , K^-/π^- , K^+/π^- , K^-/π^+ as a function of pseudorapidity density ($dN/d\eta$).	137
4.21	Measured dynamical K/π fluctuations in terms of $\nu_{dyn}(K\pi)$ for Cu+Cu interactions at $\sqrt{S_{NN}} = 62.4$ GeV scaled with pseudorapidity density ($dN/d\eta$) for K/π , K^+/π^+ , K^-/π^- , K^+/π^- , K^-/π^+ as a function of pseudorapidity density ($dN/d\eta$) from theoretical model calculations	138
4.22	Measured dynamical K/π fluctuations in terms of $\nu_{dyn}(K\pi)$ for Cu+Cu interactions at $\sqrt{S_{NN}} = 200$ GeV scaled with pseudorapidity density ($dN/d\eta$) for K/π , K^+/π^+ , K^-/π^- , K^+/π^- , K^-/π^+ as a function of pseudorapidity density ($dN/d\eta$) from theoretical model calculations	138
5.1	Schematic view of preshower plane, numbering and layout of the Supermodules (13-24) and FEE chains (25-48) during RHIC Run V.	147
5.2	The isolated cell ADC distribution for one of the supermodule in the preshower plane	149
5.3	The Relative cell to cell gain distribution for one of the supermodule in the preshower plane.	149
5.4	Photon reconstructed efficiency (ϵ_γ) as a function of pseudorapidity (η) window for different centrality classes in Cu+Cu interactions at $\sqrt{S_{NN}} = 62.4$ GeV.	152

5.5	Purity (f_p) of Photon sample as a function of pseudorapidity (η) window for different centrality classes in Cu+Cu interactions at $\sqrt{S_{NN}} = 62.4$ GeV.	152
5.6	Two dimensional picture of Preshower plane.	153
5.7	Supermodule in preshower plane that used in the present analysis.	154
5.8	Pseudorapidity (η) wise geometrical acceptance factor for the preshower plane.	154
5.9	Minimum Bias N_γ Multiplicity Distributions for Cu+Cu interactions at $\sqrt{S_{NN}} = 62.4$ GeV. The N_γ multiplicity for top 10% central events are shown in open circles. The solid curve is the Gaussian fit to the data points.	156
5.10	Experimental measured photon pseudorapidity ($dN_\gamma/d\eta$) distributions for different centrality classes as a function of pseudorapidity (η).	158
5.11	Comparison of experimental measured photon pseudorapidity ($dN_\gamma/d\eta$) distributions for different centrality classes as a function of pseudorapidity (η) with HIJING predictions.	158
5.12	Measured variation in N_γ per participant pair as a function of number of participant nucleons (N_{part}) and their comparison with HIJING.	160
5.13	Photon pseudorapidity distributions per participant pair, $(dN_\gamma/d\eta)/0.5*N_{part}$ for different centrality classes as a function of η and their comparison with HIJING predictions.	160
5.14	Measured photon pseudorapidity distributions scaled to number of participant nucleons($(dN_\gamma/d\eta)/0.5*N_{part}$) as a function of $\eta - Y_{beam}$	162

5.15	Pseudorapidity (η) distribution recorded by Photon Multiplicity Detector(PMD) for Cu+Cu interactions at $\sqrt{S_{NN}} = 62.4$ GeV. .	165
5.16	$\nu_{dyn}(\gamma_1, \gamma_2)$ as a function of pseudorapidity density ($dN/d\eta$) for Cu+Cu interactions at $\sqrt{S_{NN}} = 62.4$ GeV compared with HIJING model predictions.	165
5.17	$\nu_{dyn}(\gamma_1, \gamma_2)$ as a function of number of participant nucleons (N_{part}) for Cu+Cu interactions at $\sqrt{S_{NN}} = 62.4$ GeV compared with HIJING model predictions.	166
5.18	Scaled $\nu_{dyn}(\gamma_1, \gamma_2)$ with pseudorapidity density ($dN/d\eta$) as a function of number of $dN/d\eta$ for Cu+Cu interactions at $\sqrt{S_{NN}} = 62.4$ GeV compared with HIJING model predictions.	166

List of Tables

1.1	Quarks and their some properties.	6
2.1	Some basic parameters for the Time Projection Chamber (TPC) in STAR experiment and its associated hardware.	59
3.1	Basic parameters of STAR Photon Multiplicity Detector.	79
4.1	Data quality cuts used for analysis.	114
4.2	Average Pion and Kaon multiplicities values for Cu+Cu inter- actions at $\sqrt{s_{NN}} = 62.4$ GeV from real and mixed event data. .	116
4.3	Average Pion and Kaon multiplicities values for Cu+Cu inter- actions at $\sqrt{s_{NN}} = 200$ GeV from real and mixed event data. . .	117
4.4	Listed fitting parameter.	128

Chapter 1

Introduction

1.1 Introduction

The questions about how the material world is put together and of what fundamental entities it is made of, have long occupied the thoughts of humanity.

Historically, the familiar system was developed in which everything known was seen in some combination of just four elements i.e., earth, fire, air and water. This theory, was the first serious attempt to find a scheme that is both simple and explains the observed complexity of the world. John Dalton (1808) atomic theory put the atomic entities of different species of elements on elementary footing. Mendeleev (1869) classification of elements with similar properties falsified this notion. The discoveries of atomic nucleus (Rutherford scattering experiment) in 1911 and nuclear constituents such as electrons (J.J. Thomson through his work on cathode rays in 1897, discovered the electron and its subatomic nature, which destroyed the concept of Dalton atoms as being indivisible units), protons (Ernest Rutherford in 1919) and neutrons (James Chadwick in 1932) opened up possibilities of discovering a complete regime of elementary particles.

Presently, our understanding of elementary particles, embodied in the theory called the “Standard Model (SM)” has taken precise shape over the last 30 years. The SM provides an organized framework for the known elementary particles. These consist of “matter particles” which are grouped into “families or generations” and “force particles”. The first family includes the electron, two kinds of quarks (called “up” and “down”), and a neutrino, a particle released when atomic nuclei undergo radioactive decay. There are two more families consisting of progressively heavier pairs of quarks and a corresponding lepton and neutrino. All normal, tangible matter is made up only of particles from the first family, since the others live for very short times. The matter particles exert forces on one another that are understood as resulting from the exchange of the force carrying particles.

The four fundamental interactions: Strong, electromagnetic, weak and gravitational account for all the physical processes and structures in the universe on all scales of size from atoms and nuclei to galaxies of stars. Electric and magnetic forces arise when particles exchange photons. The strong force that hold quarks together to form protons and neutrons comes from the exchange of gluons. The weak forces that cause radioactive decay are created by massive W and Z particles (the photon and gluon have no mass). These three forces (strong, electromagnetic and weak) have been successfully described by quantum theories that have remarkably similar structures.

In order to localize the investigations to the very small scales of distance associated with the elementary constituents, one requires radiation of the smallest possible wave length and highest possible energy. Also many of the fundamental constituents have large masses and require correspondingly high energies for their creation and study[1].

High Energy Physics searches for the fundamental particles and forces which build the world around us. Like all matter is made from atoms, all atoms are made from even smaller particles. Physicists discovered that similar to the periodic system of atoms, there is a list of subatomic particles. We create those particles (which are not a normal part of matter we encounter everyday) by using the famous ‘Einstein Law’ that relates energy and matter: $E = mc^2$. Compared to natural processes on earth, like the creation of a lightning or the energy released in a nuclear decay, the energy per particle is many magnitudes higher. The main objective of the experimental high energy physics is to search for new physics and to explore the predictions of the standard model to unprecedented accuracy.

In the 20th century it is now almost universally accepted that the matter surrounding us presently was created billions of years ago in an explosion termed the Big Bang. Figure 1.1 shows the life transitions of universe from birth to present stage. It is believed that after the occurrence of the Big Bang the universe expanded and cooled to become what we are currently observing. However, if we were to observe the Universe a millisecond after the Big Bang, our observations would be very different. The temperature of what was then the Universe is thought to have been on the order of trillions of degrees Kelvin, and the dominating state of matter was a soup of weakly interacting or non-interacting elementary particles including quarks and gluons, which we call the Quark-Gluon Plasma (QGP). The challenge of creating and studying such a new state of matter has been the stimulus behind the high energy heavy-ion programme.

As the universe cooled, quarks and gluons became bound in hadrons, baryon (three quark) or meson (quark-antiquark pair). So in this way we encounter quarks today, in our every day, ordinary cold nuclear matter. In order to understand the picture of the

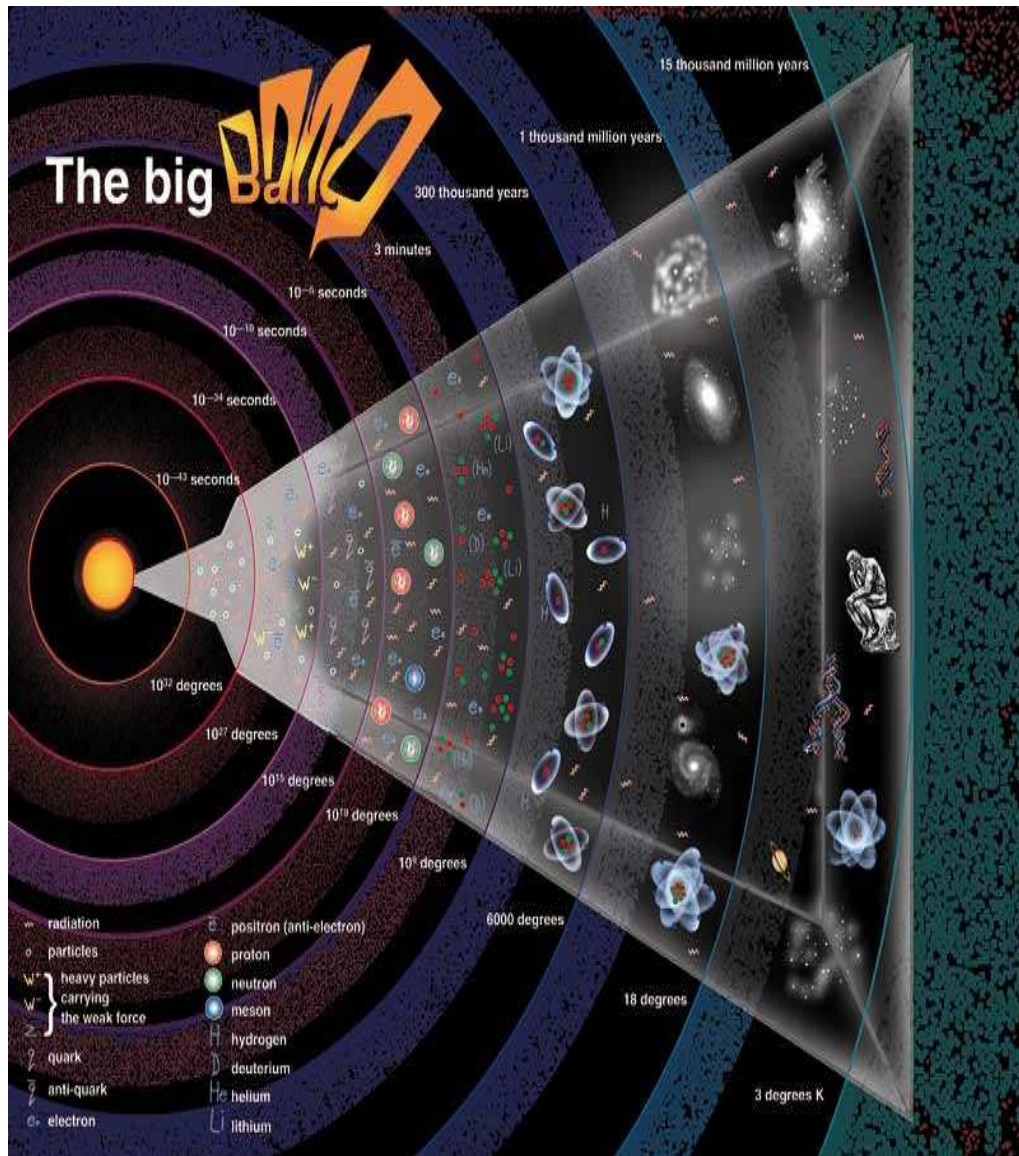


Figure 1.1: Shows the hallmarks in the development of energy-mass conversion, nucleonic synthesis, neutral bulk matter etc. after the Big Bang in relevant time and temperature scenario.

universe appeared just after the Big Bang and to study quark properties, we must first understand what makes the quarks bind to make hadrons (baryon and mesons), and what conditions must be met in order for quarks to become unbound.

1.2 Quantum Chromodynamics (QCD) and Phase Transition

In the Standard Model, particles can be classified as leptons, quarks or interaction mediators. The leptons are the light particles and are described by the three leptonic quantum numbers and electric charge, while quarks (constituents of hadrons) are described by their flavor (the equivalent of the leptonic quantum number), charge, and color, an additional quantum number. A quark can have one of three colors, R (red), G (green), and B (blue). Hadrons are colorless, because either they composed of a quark and an anti-quark of the same color, or are made up of three RGB quarks (anti-quarks). All quarks are fermions (have a spin of $1/2$), and if not for color, the Pauli's exclusion principle would forbid three-quark states of the same flavor. The color (RGB) quantum number enables us to describe states of three quarks of the same flavor, such as the Δ^{++} baryon, made up of three-quark u (up) quarks. In Table 1.1 are listed all the six quarks, their masses and charges [2].

Since quarks are confined inside hadrons, quark masses cannot be measured directly but instead they can be determined indirectly through their influence on hadronic properties.

We know nucleus of an atom is a composite of many nucleon system and the force

Quark	Charges	Mass (MeV)	Spin
u (up)	$+\frac{2}{3}$	1.5-3.0	1/2
d (down)	$-\frac{1}{3}$	3-7	1/2
s (strange)	$-\frac{1}{3}$	95 ± 25	1/2
c (charm)	$+\frac{2}{3}$	1250 ± 90	1/2
b (bottom)	$-\frac{1}{3}$	4200 ± 70	1/2
t (top)	$+\frac{2}{3}$	174200 ± 3300	1/2

Table 1.1: **Quarks and their some properties.**

which binds the nucleons together inside the atomic nuclei is the strong force. The gluons are the mediators for the strong force. The theory of Quantum Chromodynamics (QCD) has been developed to describe the strong force interactions of quarks and gluons which in many respects is similar to Quantum Electrodynamics (QED). However, there is an important difference. The “charge” in QCD is color. Gluons, which act as color mediators, make up a color octet. Because gluons carry color, they can self-interact. This introduces a peculiar condition. The strong force between two quarks does not decrease with distance, but grows stronger. The potential between two quarks can be written as:

$$V(r) = -\frac{4\alpha_s}{3r} + kr \quad (1.1)$$

where α_s is the coupling constant, $\frac{4}{3}$ is the color factor, r is the distance between two quarks, and k is a constant, experimentally determined to be about 16 tons [3]. At large distances the first term in the r.h.s in the above equation becomes negligible and the equation becomes linearly dependent on r . Thus it is clear that the energy of the field between two quarks can grow arbitrary large with increasing distances. This

is what is known as “confinement” - the quarks cannot be separated by being pulled apart; as the quarks separate, it becomes energetically favourable to produce a quark and anti-quark pair from the vacuum to reduce the original two-quark potential [4]. This means that it is not possible to separate two quarks over a large distance scale, and thus the quarks are confined. However, since the small distance scale is governed by the term proportional to $\frac{1}{r}$, deconfinement of quarks is possible if α_s approaches to a small value faster than r . Partons behave almost as free particles when they are very close to each other. This surprising phenomenon called “asymptotic freedom”, honored by a Nobel Prize awarded to David J. Gross, H. David Politzer, Frank Wilczek in 2004, has led to our current QCD theory describing interactions of particles.

At very high densities and energies, asymptotic freedom leads to the predicted existence of a Quark-Gluon Plasma (QGP) phase of matter. The phenomenon expected to lead to a QGP in heavy-ion collisions is the Debye Screening of the color charge at high partonic densities. This is analogous to the Debye Screening of an electric charge in Quantum Electrodynamics (QED). Compressed quark matter at high densities is predicted to produce a color conducting system of deconfined quarks and gluons referred to as the QGP phase. It is believed that in heavy-ion collisions at relativistic energies the deconfinement conditions can be reached due to the high energy densities produced in the collision region. Also the QGP has long been thought to be a state of equilibrated matter, where asymptotic freedom has been established.

How does one go about creating the Quark Gluon Plasma (QGP) in the laboratory? Looking at the schematic diagram of the phases of nuclear matter [5] is shown in figure 1.2. In figure 1.2, it is observed that the early universe conditions included zero baryo-chemical potential, μ_B (an equal amount of quarks and anti-quarks), and

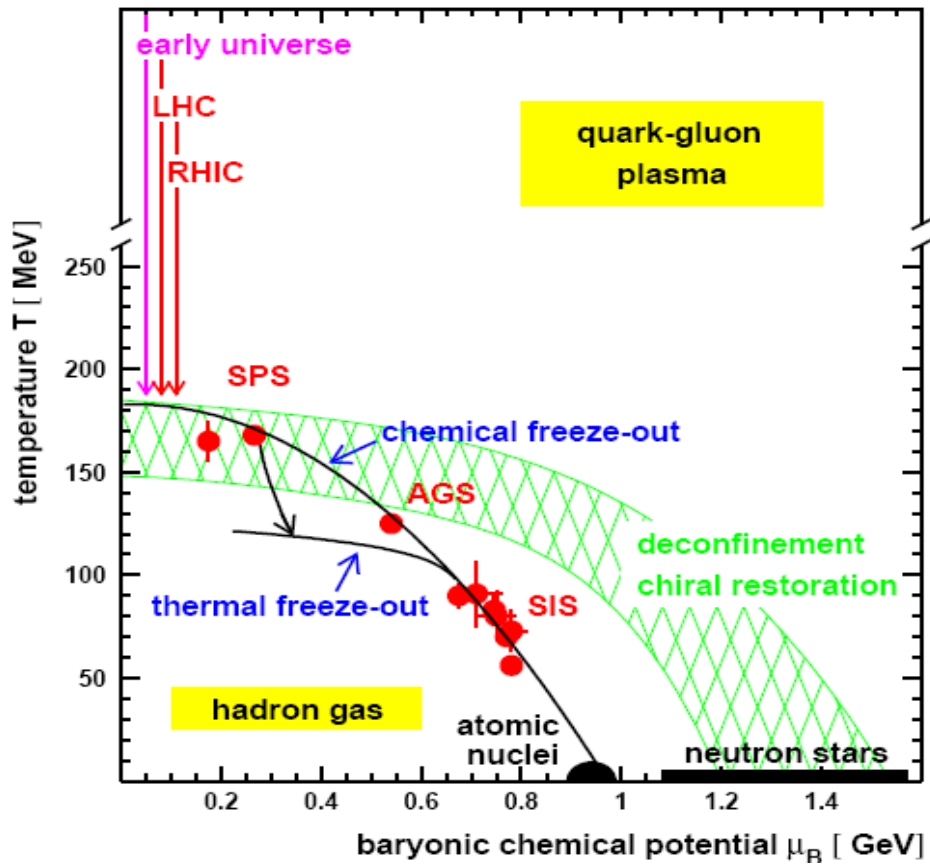


Figure 1.2: A schematic phase diagram of nuclear matter. Heavy-Ion collisions at Relativistic Heavy Ion Collider (RHIC) are thought to be at low baryon chemical potential and temperatures greater than or equal to 170 MeV.

very high temperatures. A QGP might already exist in neutron stars and supernovae, made entirely of baryonic matter (high μ_B), with extremely high baryon densities and temperatures much lower than the 170 MeV shown in the figure (the number comes from the critical temperature at $\mu_B = 0$ in calculations on a two and three quark lattice, and is thought to be about 170 MeV). However, these are inaccessible for study. Thus we attempt to approximate the μ_B condition, which is similar to that of the Big Bang, in a laboratory. To do this, facilities were built to collide heavy-ions at very high energy in hopes of creating a new state of matter i.e. QGP with partonic degrees of freedom.

The field of relativistic heavy-ion collisions has been in existence for over thirty years. The phase transition diagram shown in figure 1.2 also indicates the $T - \mu_B$ phase space accessible to facilities used for relativistic heavy-ion in the past: Superconducting Synchrotron (SIS), Alternating Gradient Synchrotron (AGS), and Super Proton Synchrotron (SPS). In the recent past studies on ultra-relativistic heavy-ion collisions undertaken to confirm the existence of new state of matter. Conclusively the experimental results regarding the QGP state need to be verified at forthcoming Large Hadron Collider (LHC) facilities at CERN (European Organization for Nuclear Research), Switzerland, Geneva. Studies reported in this thesis have been conducted on the data obtained at the Relativistic Heavy-Ion Collider (RHIC) in STAR experiment at the Brookhaven National Laboratory (BNL), USA. The details about STAR experimental setup will be described in chapter two.

1.3 Space Time Evolution

The formation of a Quark-Gluon Plasma (QGP) at very high energy collisions of heavy nuclei has been studied in various theoretical models. In collision process, the energy

and baryon densities are expected to increase and reach critical values where the quark constituents of the incident nucleons, bound in nuclei, form an extended volume of freely interacting quarks, anti-quarks and gluons. The system must sustain these conditions for a time longer than the transition time of the two interacting nuclei in order for QGP phase to form without dilution by subsequent interactions. These high baryon and energy densities necessary for the formation of a QGP state may best be reached in collisions of heavy nuclei at very high energies given adequate thermalization.

The space-time evolution of the system formed in the heavy-ion collisions is shown in the figure 1.3. In high energy heavy-ion collision two accelerated nuclei approach each other with velocities very close to the velocity of light and thus Lorentz-contracted. In figure 1.3 the nuclei are represented by orange pancake-like ellipses. As these “pancakes” collide, the most energetic interactions form the earliest probes: quarkonia (pairs of heavy quarks and anti-quarks) are thought to be created, as well as “jets”, a result of large momentum transfer hard scattering processes that produce high energy partons liberated from their respective nucleons. In vacuum, these partons fragment into hadrons, produced in a signature light cone. Jets and heavy quarks make especially valuable probes of matter created, since they are produced before the formation of the medium. As they traverse the medium, possible modifications to the jet and heavy quark yields and spectra may occur. When detected after the collision, they can offer significant insight into the nature of the medium. This can be done by comparing unmodified (in-vacuum) jet and quarkonia yields and spectra to those which have passed through the medium.

One important question in relativistic heavy-ion physics is whether the matter reaches equilibrium during the collision process or not. If there is a QGP formation

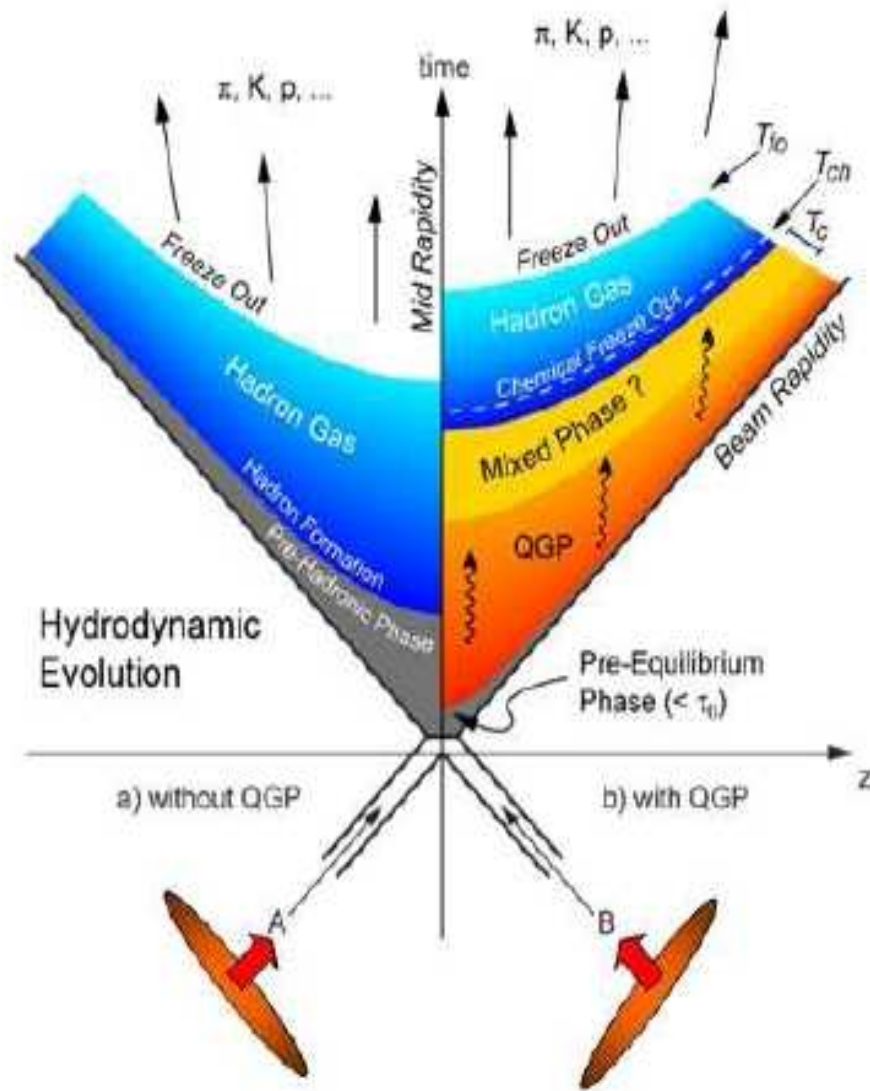


Figure 1.3: The possible scenario for a relativistic heavy-ion collision evolution.

and the system is in equilibrium state, then thermodynamics can be used to describe the system. In this case, the particle yields and their spectra will reflect the equilibrium conditions. However, mainly, there are two different types of equilibrium which are commonly discussed, one is called chemical and other is thermal equilibrium. The chemical equilibrium occurs when the creation and annihilation of the particles, reach their equilibrium values. The resulting particle abundances no longer change on average. The thermal equilibrium occurs when the whole system reaches the same temperature after which the particle spectra no longer change. More precisely, when the system starts expanding the mean distance between the particles and the time between interactions increase. When the interaction cease, this leads to freeze-out because probability of further interaction is very small. The inelastic cross section determines, when the chemical freeze-out would occur while the total cross section determines the time for thermal freeze-out. Since inelastic cross sections are always smaller than the total cross section, the inelastic reactions that change the particle species cease leading to a chemical freeze-out at an earlier time than the change in kinematics and temperature resulting in a thermal freeze-out.

After the initial collision phase, two scenarios are possible. In the first scenario we would observe formation of a hadron (mostly pion) gas. This scenario could almost be linked to a superposition of many binary collisions of nucleons, such as $p + p$. The formation of hadrons would be followed by kinetic freeze-out (because hadrons will stop interacting), which fixes the shape of particle momentum spectra. In the other scenario the initial stage would be followed by an equilibrated plasma state, gradually becoming a mixed phase of partons and hadrons as the plasma cools. Once, the mixed phase is over and chemical freeze-out of the resultant particles occurs, the fireball becomes a hadron gas, also followed by kinetic freeze-out, as in the former scenario.

1.4 The Bag Model

The bag model provides a useful phenomenological description of quarks being confined inside hadrons. In this model quarks are treated as massless particles inside a bag of finite dimension. They are infinitely massive outside the bag. Quarks confinement in the model is the result of the balance of the bag pressure B , which is directed inward and the stress arising from the kinetic energy of the quarks. Here, the bag pressure B is a phenomenological quantity introduced to take into account the nonperturbative effects of Quantum Chromodynamics (QCD). If the quarks are confined in the bag, the gluons should also be confined in the bag. Therefore, the total color charge of the matter inside the bag must be colourless. Since there are three different types of color, the bag model would imply that the allowable hadronic bags should include colorless baryon (qqq) and mesons ($q\bar{q}$) states.

1.5 Quark Gluon Plasma (QGP) and its Signatures

The understanding of the equation of new state of nuclear, hadronic and partonic matter is an interdisciplinary interest to particle physics, nuclear physics, astrophysics and cosmology. It is also the main motivation for studying relativistic heavy-ion collisions which are primarily searching for the so-called Quark-Gluon Plasma (QGP). QGP is a state in which quarks and gluons, the fundamental constituents of matter, are no longer confined within the dimensions of the nucleon, but are free to move around over a volume in which a high enough temperature and/or density prevails. A quark-hadron phase transition is believed to have occurred at about ten microseconds after the Big

Bang when the universe was at a temperature of approximately 150 to 200 MeV. The QGP may also exist in the cores of dense stars at high baryon densities $\sim 1\text{GeV}/\text{fm}^3$.

Further experimental investigations of QGP phase require the identification of appropriate experimental tools for observing its formation and for studying its properties. There is a serious problem in the detection of QGP phase because of its limited size and lifetime. A Variety of signatures have been proposed for the identification of Quark Gluon Plasma (QGP) state through analysis of produced particles in ultra-relativistic heavy-ion collisions. The most widely accepted are transverse momentum distribution, photons and dileptons production, suppression of the J/Ψ production, fluctuations and correlations, jet quenching, flow and production of strange particles. In the following section the above mentioned signatures are described in details.

1.5.1 Transverse Momentum Distribution

Important information about the dynamics of particle production and the evolution of the system formed in the collision can be obtained from various global observables, such as the multiplicity, transverse energy and transverse momentum (P_t). The momentum spectra of the emitted particles give insight into the kinetic freeze-out stage of the system. At this stage hadrons are no longer interacting and their momenta do not change. The experimentally measured spectra of hadronic particles thus reflect the state of the system at freeze-out. This gives the information, whether the new state of matter (Quark-Gluon Plasma phase), i.e. an equilibrated state of quarks and gluons, was created at some stage during the evolution of the system [6]. It has been suggested that, the correlation between mean transverse momentum ($\langle P_t \rangle$) and multiplicity of the produced particles may serve as a probe for the equation of state of the hot hadronic

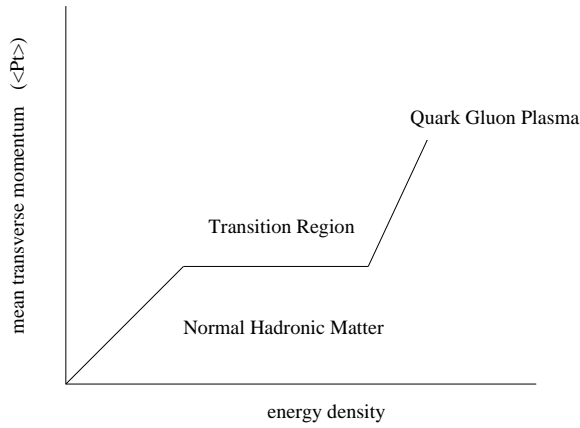


Figure 1.4: **Schematic behaviour of the average transverse momentum ($\langle P_t \rangle$) as a function of the energy density for matter in the hadronic phase, in a transition region and in the Quark-Gluon Plasma phase .**

matter and by making use of these two variables one can look into the structure of the Temperature - Energy ($T - \varepsilon$) diagram [7]. From Landau's hydrodynamical model [8] we observe that the rapidity density (dN/dy), reflects the entropy, whereas the mean transverse momentum ($\langle P_t \rangle$) reflects the temperature. The rapidity density (dN/dy) linearly scales with the mean transverse momentum ($\langle P_t \rangle$), except at the phase transition points. If the phase transition is of first order, then the temperature remains constant at the point of phase transition from hadron gas to Quark-Gluon Plasma phase thereby increasing the entropy density. So the mean transverse momentum ($\langle P_t \rangle$) will show a plateau while entropy will go on increasing. Hence the observables like rapidity density (dN/dy) and mean transverse momentum ($\langle P_t \rangle$) of charged particles will give some information about the Quark-Gluon Plasma phase and also the order of phase transition.

Transverse momentum (P_t) distribution as a signature of quark-gluon plasma were studied in various experiments (UA1, WA80, NA34 and NA38). The JACEE collaboration observed significantly large values of average transverse momentum ($\langle P_t \rangle$) of the

charged particles at very high energy cosmic ray interactions with nuclear emulsion in comparison to $\langle\langle P_t \rangle\rangle$ values measured at lower energies [9]. Average transverse momentum $\langle\langle P_t \rangle\rangle$ as a function of rapidity density (dN/dy) and energy density respectively shows a some sort of saturation and after that there is rapid increase of $\langle\langle P_t \rangle\rangle$. UA1 collaboration also have the simliar observations at the CERN antiproton-proton collider at 540 GeV. Van Hove [7] and Shuryak and Zhurov [10] have suggested that a rapid increase of $\langle\langle P_t \rangle\rangle$ could be due to the formation of Quark-Gluon Plasma phase. Figure 1.4 shows a small increase in average transverse momentum $\langle\langle P_t \rangle\rangle$ for small value of energy density, corresponding to normal hadronic matter, a transition region in a sort of saturation/plateau and a rapid increase which due to the formation of the Quark-Gluon Plasma phase. Hence studies of transverse momentum (P_t) distribution provide important and useful information on deconfined state of nuclear matter.

1.5.2 Photons and Dileptons Production

Direct photons, as well as dileptons, are important probes for Quark-Gluon Plasma (QGP) phase formation. In QGP phase thermal photons are produced either by annihilation process of quark, anti-quark pairs ($q + \bar{q} \rightarrow \gamma + g$) or by compton scattering process of quark and anti-quark with gluons ($q + g \rightarrow \gamma + q$). Once produced, they interact with the surrounding matter only electromagnetically, resulting in a long mean free path and therefore, it may not suffer a collision after it is produced. The rate of photon production and its momentum distribution depends on the momentum distributions of the quarks, anti-quarks, and gluons in the plasma. Thus, photons can escape from the system immediately after their production, storing in memory the history of the early stages of the collisions. Also, there are predictions of more direct photon production associated to Quark-Gluon Plasma formation [11]. In addition lots of photons

are produced from neutral pion (π^0) and η mesons decays.

The measurement of prompt photons is challenging due to the huge background from neutral pion (π^0) and η decays. The WA98 collaboration has reported an observation of direct photon excess production in ultra-relativistic heavy-ion collisions in Pb+Pb interactions [11]. Figure 1.5 shows the invariant direct photon yield as a function of transverse momentum (P_t) in central Pb+Pb collisions at 17.2 GeV. In the same plot, the WA98 data have been compared with the p+p and p+C results obtained from the other experiments, scaled by the average number of inelastic nucleon-nucleon collisions. Results of a perturbative QCD calculation are also shown in the figure for comparison. Comparing the results to pA interactions at 200 GeV, properly rescaled to 158 GeV, are also shown. One observes that the direct photon production excess in central Pb+Pb interactions stands beyond the expected from proton-induced reactions up to very high transverse momentum (P_t).

Yet other ways in which a Quark-Gluon Plasma (QGP) phase could manifest itself is the anomalies in the dilepton production. In the QGP the dileptons would be created in a $q + \bar{q} \rightarrow l^+ + l^-$ reaction [4]. Since leptons are light particle and therefore cannot interact strongly. Thus, dilepton pairs are thought to carry information about their production conditions (the temperature of the plasma) past the final freeze-out, where they can be detected. Measuring an excess of dilepton pairs in the 1-4 GeV/ c^2 region of the dilepton invariant mass should indicate the temperature of the medium that produced them. The measurement is not trivial and the accuracy of the conclusions are highly dependent on the temperature of the plasma. The method seems to be valid for plasma temperatures above 300 MeV, as the QGP formed dilepton yields will start to surpass the Drell-Yan yields in a narrow part of the dilepton spectrum. Thus looking

for dilepton signature has proved to be difficult experimental observable, but there is a continued effort to improve the sensitivity of the measurements.

1.5.3 Suppression of the J/Ψ Production

J/Ψ suppression as a signature of Quark-Gluon Plasma (QGP) state was predicted by T. Matsui and H. Satz in 1986 [12]. They suggested that the production of J/Ψ is suppressed when there is a phase transition from confined to the deconfined phase of quarks and gluons. In a QGP the color of a quark is subject to screening due to the presence of quarks, anti-quarks and gluons in the plasma i.e., Debye screening. J/Ψ is the bound state of $c\bar{c}$ pair, a charm quark and its anti-quark, would in a quark-gluon plasma medium be unable to form a J/Ψ resonance because of the Debye screening of the confining potential. Therefore J/Ψ production in a Quark-Gluon Plasma state will be suppressed. This signature is particularly interesting because the $c\bar{c}$ states, composed of heavy quarks, can only be produced at the earliest times in the collision evolution, in hard processes (gluon fusion) that happen early enough to probe the formation of the Quark-Gluon Plasma state. Besides, tightly bound states as the J/Ψ meson are not easy to break in the relatively soft interactions they may suffer while crossing the surrounding (hadronic) matter. Finally, the dimuons resulting from the decay of the J/Ψ mesons are not affected by the strong interactions that reign during hadronization, flying through and bringing to the detectors an undistorted image of the earlier phases.

NA50 collaboration extensively measured J/Ψ suppression for central Pb+Pb collisions at SPS energies which has given evidence for Quark-Gluon Plasma state formation [13, 14, 15]. Anomalous J/Ψ suppression was observed in figure 1.6 [15] for Pb+Pb interactions. Figure 1.7 [15] shows ratio $B_{\mu\mu}\sigma(J/\Psi)/\sigma(DY)$ as a function of E_T , for the

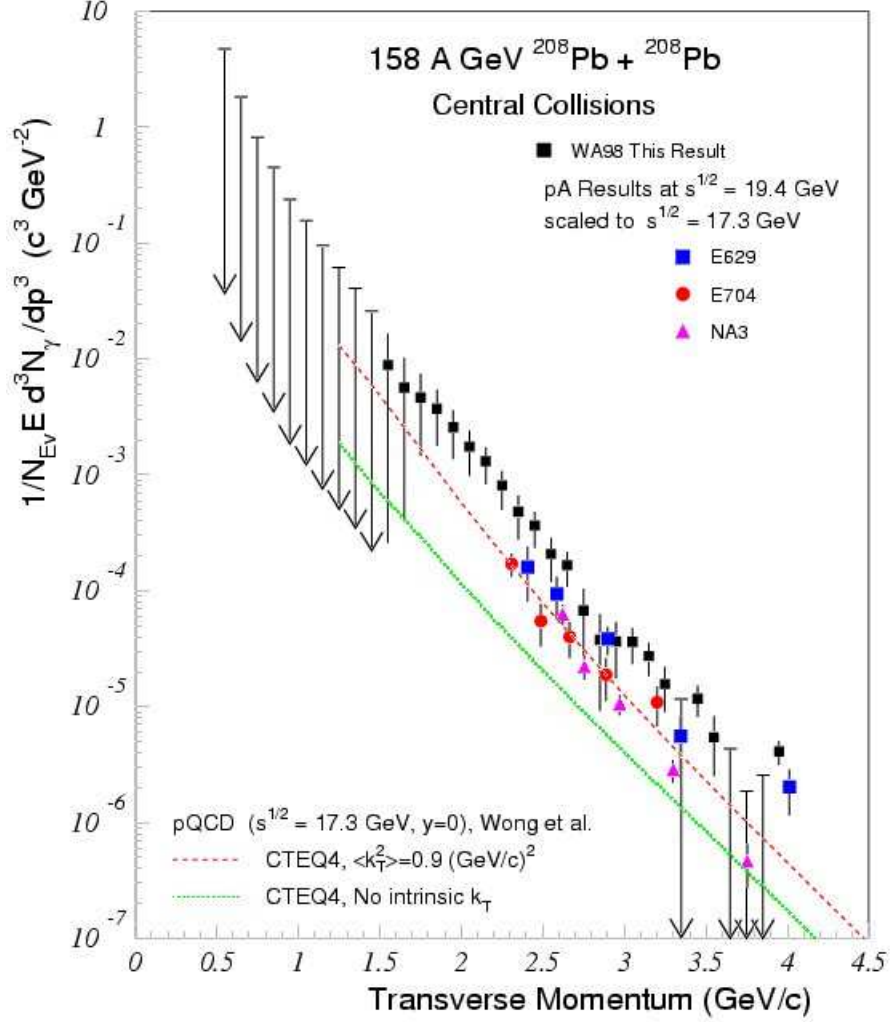


Figure 1.5: The invariant direct-photon multiplicity as a function of the transverse momentum (P_t) in central Pb+Pb interactions at 17.2 GeV. The figure is taken from [11]. The errors bars indicate the combined statistical and systematic uncertainties. The data points with downward arrows indicate unbounded 90% CL limits on the direct photon yield. The WA98 data points are compared with scaled p+p, p+C results, pQCD calculation and scaled parametrization of direct-photon yields in p+p collisions.

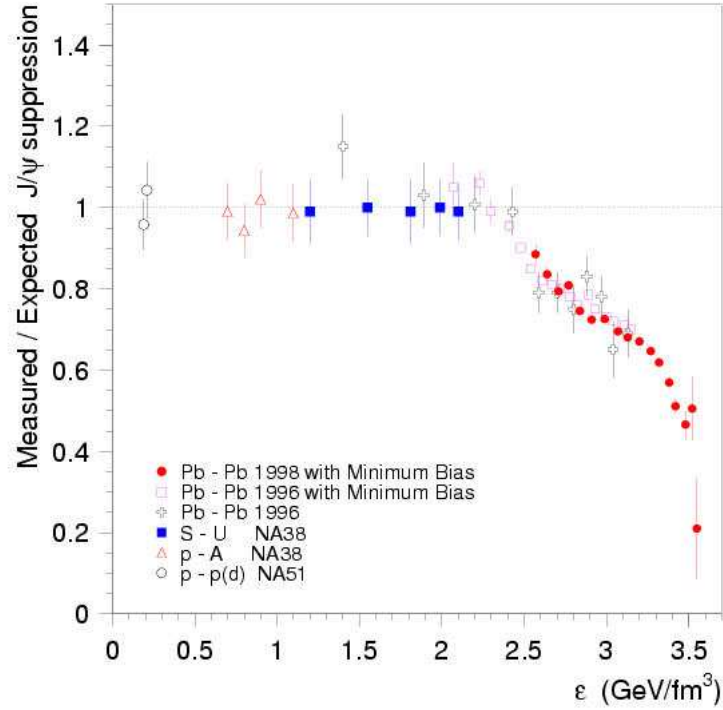


Figure 1.6: The anomalous suppression as a function of the energy density reached in the collision for different experiments. Suppression is obtained from the measured cross-sections divided by the values expected from nuclear absorption. It is observed that in Pb+Pb interactions J/Ψ is suppressed normally, i.e. according to pure nuclear absorption, for energy densities lower than $2.2 \text{ GeV}/fm^3$. For higher density values, a peculiar abnormal suppression pattern is observed, as can be expected from charmonium due to deconfinement.

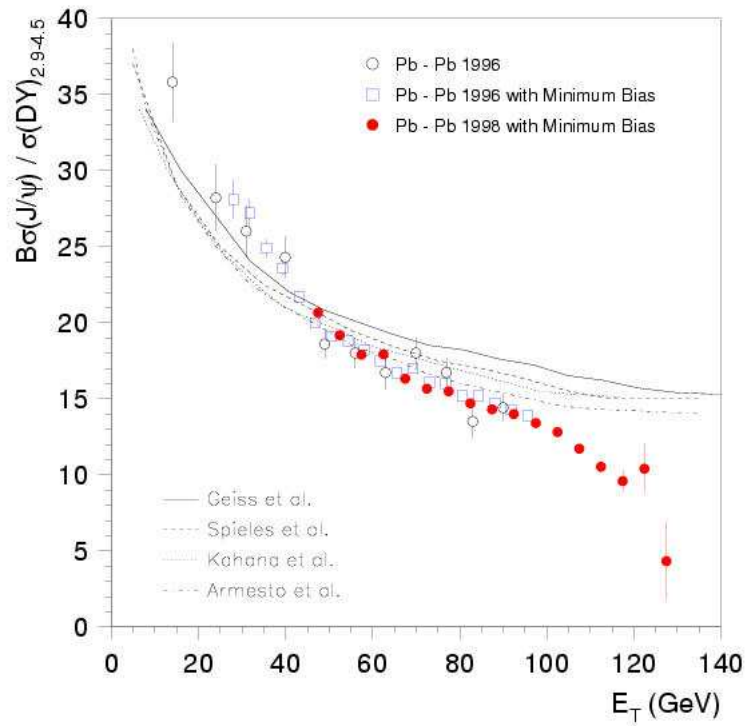


Figure 1.7: The Comparison between the NA50 Pb+Pb data and several conventional calculations of J/Ψ suppression.

Pb+Pb data taken in different years by the NA50 collaboration at SPS energies and their comparison with several conventional calculations. The continuous line stands for normal absorption of J/Ψ in nuclear matter. Also the results suggest that there is an onset of a new physical process for energy densities higher than $2.2 \text{ GeV}/fm^3$. On one hand, the J/Ψ production rate exhibit a sudden departure from the nuclear absorption regime and on the other hand, the deviation from this regime increases steadily with increasing energy density. These two features are incompatible with explanations based on conventional hadronic physics mechanisms, as reflected from figure 1.7. These can be naturally understood in the framework of charmonia melting due to quark-gluon phase formation, where a stepwise pattern is expected. The signal of deconfinement predicted several years ago by T. Matsui and H. Satz seems to have been observed.

1.5.4 Fluctuations and Correlations

The study of correlations and fluctuations can provide evidence for the production of the Quark-Gluon plasma (QGP) in relativistic heavy-ion collisions. A physical system is well characterized by studying fluctuations and correlations. In general, one can distinguish between several classes of fluctuations. On the most fundamental level there are quantum fluctuations, which arise if the specific observable does not commute with the Hamiltonian of the system under consideration. These fluctuations probably play less a role for the physics of heavy-ion collisions. Second, there are dynamical fluctuations reflecting the dynamics and responses of the system. A system evolving near a phase boundary should develop significant dynamical fluctuations away from the mean thermodynamic properties of the matter. For high-energy heavy-ion collisions, it has been predicted that the general study of two particles and event-wise fluctuations might provide evidence for the formation of matter with partonic degrees of freedom [16, 17].

Fluctuations are also closely related to phase transitions. The well known phenomenon of critical opalescence is a result of fluctuations at all length scales due to a second order phase transition. First order transitions, on the other hand, give rise to bubble formation, i.e. density fluctuations at the extreme. In addition, nonstatistical correlations and fluctuations may be introduced by incomplete equilibrium [18]. Also the dynamical fluctuations help to characterize the properties of the bulk (semi-classical) description of the system. Examples are density fluctuations, which are controlled by the compressibility of the system. Finally, there are “trivial” fluctuations induced by the measurement process itself, such as finite number statistics etc. These need to be understood, controlled and subtracted in order to access the dynamical fluctuations which tell us about the properties of the system.

There are various methods [19, 20] to look for fluctuations in the system but the event-by-event fluctuations is the most efficient way to investigate the fluctuations of a system in a heavy-ion collisions, wherein a given observable is measured on an event-by-event basis and the fluctuations are studied over the ensemble of the event.

Event-by-Event Fluctuations: In event-by-event studies, it is expected that one would find events which would carry the signature of the Quark-Gluon Plasma (QGP) state. Pioneering experiments in this direction have been carried out by the NA49 collaboration [21]. The NA49 collaboration has measured event-by-event fluctuations of the mean transverse momentum (P_t) as well as the kaon to pion ratio [22] at the CERN SPS energies at slightly forward rapidities.

The event-by-event dynamical fluctuations studied by NA49 collaboration in the kaon to pion ratios [23] in central Pb+Pb collisions at 20-158 A GeV are shown in the

figure 1.8. The observed strength of dynamical fluctuations in the kaon to pion ratio are positive and decrease with beam energy [23, 24]. Also in the figure 1.8 the observed signal of fluctuations were compared with the string-hadronic cascade model UrQMD [25]. In this model, by construction, no fluctuations due to a potential phase transition are present. The energy dependence fluctuations signal of the event wise kaon to pion ratio, cannot be reproduced by the cascade model. UrQMD gives an energy independent fluctuations signal. Since the relative contribution of resonances changes dramatically with incident beam energy [26], therefore in the case of kaon to pion ratio resonances do not give a significant contribution to the fluctuations signal. The magnitude of fluctuation signal in UrQMD model can be attributed to correlated particle production due to conservation laws. Also in the data a significantly smaller magnitude of dynamical fluctuations is observed at the highest beam energies under study as compared to cascade model calculations. Towards lower beam energies, a steep increase of the fluctuation signal is observed. The increase in fluctuation signal goes significantly beyond the values predicted in a hadronic cascade model at lower energies, indicating the onset of a new source of fluctuations.

On the other hand the transverse momentum (P_t) fluctuations should be sensitive to temperature/energy fluctuations [27, 28] and also provide a measure of the heat capacity of the system [29]. Since quantum chromodynamics (QCD) phase transition is associated with a maximum of the specific heat, the temperature fluctuations should exhibit a minimum in the excitation function and it has also been suggested [16, 30] that these fluctuations may provide a signal for the long range fluctuations associated with the tri-critical point of the QCD phase transition. In the vicinity of the critical point the transverse momentum fluctuations should increase, leading to a maximum of the fluctuations in the excitation function. Experimentally NA49 collaboration at

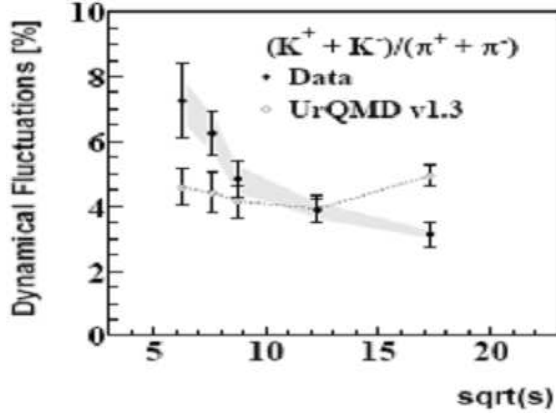


Figure 1.8: **Energy dependence of the event-by-event dynamical fluctuations from K/π ratio in Pb+Pb collisions studied by NA49 experiment at SPS. The systematic errors of the measurements are shown as grey bands.**

SPS energies [21] and, PHENIX collaboration at RHIC [31] energies observed no significant non-statistical transverse momentum (P_t) fluctuations. In contrast to NA49 and PHENIX, the CERES collaboration [32] at SPS energies and also STAR experiment at RHIC energies report significant deviations from mixed events [33].

Charge fluctuations among produced particles in a collision is expected to signify deconfined state as QGP is a system of fractional charges [34, 35]. PHENIX [31] and STAR [36] experiments at RHIC observed that charge fluctuations are consistent with a resonance gas scenario. Similar observations are reported by CERES [37] and NA49 [38] at SPS energies. However, at the SPS energies the overall rapidity distribution is rather narrow, and the correlation effect of the resonance might get lost when correcting for charge conservation [39]. But certainly, none of the measurements is even close to the predictions for the QGP state. These findings have prompted ideas, that possibly a constituent quark plasma, without gluons, has been produced [40]. However, the mea-

surement of additional observables would be needed in order to distinguish this from a hadronic gas.

On theoretical plane the event-by-event fluctuations has recently gained considerable interest. The influence of hadronic resonances and possible phase transition has been investigated [30, 41]. All the theoretical predictions assume that the observed fluctuations will be Gaussian and thus the physics information will be in the width of the Gaussian, which is controlled by 2-particle correlations [42].

In the framework of statistical physics, which appears to describe the bulk properties of heavy-ion collisions up to RHIC energies, fluctuations measure the susceptibilities of the system. These susceptibilities also determine the response of the system to external forces. For example, by measuring fluctuations, of the net electric charge in a given rapidity interval, one obtains information on how this system would respond to applying an external (static) electric field.

1.5.5 Jet Quenching

Jet Quenching as a signature [43, 44, 45] of Quark-Gluon Plasma (QGP) phase transition is the suppression of partonic jets and their high transverse momentum (P_t) hadronic debris due to energy loss of the jets in the medium. High P_t quark and gluon jets, materialize very early during the collision. While propagating through the dense medium these partons will experience the strong interaction with the medium in the process losing energy through gluon radiation. This energy loss is supposed to be larger in a medium of deconfined color charges than in normal hadronic matter. This effect is known as Jet Quenching and could show up as a depletion in the yield of high P_t hadrons making it a

potential probe for the study of a high density deconfined phase transition [46, 47, 48]. In order to measure the high P_t hadron suppression in relativistic heavy-ion collisions, a comparison of the hadron P_t spectrum in nucleus-nucleus collisions with reference data from pp or $p\bar{p}$ collisions at the same energy is undertaken.

1.5.6 Flow

The measurement of an azimuthal anisotropy in the emission of particles with respect to the reaction plane [49] i.e. the plane formed by the beam direction and the direction of vector connecting the center of the two colliding nuclei is sensitive to the early times. When one approaches the phase transition region the equation of state (EOS) becomes very soft and only a small increase of the transverse flow velocity is expected. When the energy density significantly exceeds that needed for QGP formation, the collective flow is expected to increase again [50]. Calculations of hydrodynamic expansion with a bag model type EOS predicts three stages with rapid, modest and again rapid increase in transverse flow with the increase in beam energy. The existence of some plateau in the middle is the consequence of softness of EOS in the mixed phase. Detailed numerical studies in context of the hydrodynamical model have shown that this characteristic feature is rather weak in realistic models which do not include a rehadronization process [51, 52].

In non-central nucleus-nucleus collisions, the event in the plane perpendicular to the beam axis exhibits an azimuthally anisotropic shape. Only the interactions between constituents generate a pressure gradient which transforms the initial coordinate space anisotropy into a momentum space anisotropy. The momentum anisotropy manifests itself most strongly in the azimuthal distribution of transverse momenta (with respect

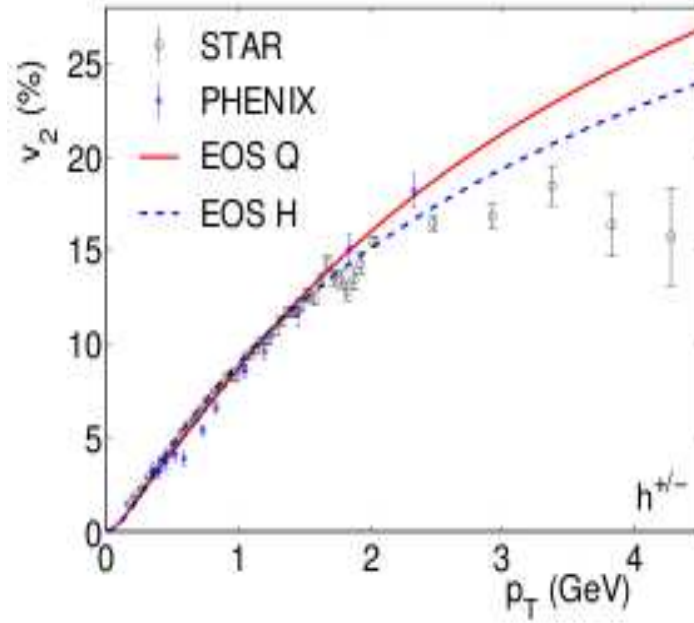


Figure 1.9: Elliptic Flow (v_2) coefficient for all charged particles measured by STAR and PHENIX in minimum bias Au+Au collisions at 130 GeV and compared to hydrodynamical calculations corresponding to equations of state (EOS) with (Q) and without (H) phase transition [57].

to the reaction plane [53] which can be quantified by the coefficients of an azimuthal fourier decomposition of the distribution. The first harmonic coefficient is called the directed flow and the second harmonic coefficient v_2 is called the elliptic flow. The spatial anisotropy is largest early in the collision, but as the elliptic flow develops, the matter begins to expand more rapidly in the initially short direction than in the long one. Therefore the spatial deformation disappears and the buildup of flow anisotropies from pressure gradients stops. That's why the magnitude of the elliptic flow should reflect the pressure, i.e. the extent of the rescattering, at relatively early time. The magnitude of elliptic flow has been found to increase from AGS [54] to SPS [55] and RHIC [56] where it reaches the values predicted by hydrodynamical models [57], as shown in figure 1.9, where the elliptic flow (v_2) of charged hadrons measured in PHENIX and STAR is shown as a function of P_t . This suggests that very fast thermalization occurs [57, 58].

1.5.7 Production of Strange Particles

The enhancement of strange and multi-strange particle yield in nucleus-nucleus reactions with respect to hadronic interactions (proton-proton or proton-nucleus) collisions has been suggested as one of the sensitive signature for Quark-Gluon Plasma (QGP) phase formation [59]. The basic argument for strangeness enhancement in the QGP state is that it is energetically favourable to produce strange particles on a partonic level rather than in a hadron gas. In hadronic interactions, the production of particles containing strange quarks are normally suppressed due to the higher mass of the strange quark ($m_s \simeq 60 - 170 MeV/c^2$) as compared to up (u) and down (d) quarks. In the Quark-Gluon Plasma phase, the temperature is of the order of the s-quark mass and rapid filling of the phase space available for up (u) and down (d) quark should favour the production of $s\bar{s}$ pairs in interactions of two gluons [59, 60]. This should be reflected in

an enhancement in the production of multi-strange baryons and strange antibaryons if a QGP is formed when compared to a purely hadronic scenario at the same temperature. Since strange hadrons interact strongly, their final-state interactions can be modeled in detail and comparison of strange particle yields can be carried out.

In a pure hadronic scenario (at least in a hot and dense hadron gas at equilibrium), the difficulty to form strange baryons increases with the strangeness content (or the mass) of the baryon. Direct production of strange particles is gradually suppressed, when going from Λ to Ξ and then to Ω particles, because of increasing energy thresholds. The production of multi-strange baryons, by means of a chain of rescattering processes, is characterized by a long equilibrium time compared to the lifetime of the fireball. This equilibration time also increases with the strangeness content of the baryon (~ 100 fm/c for the Ω), hence the higher the strangeness content, the larger the suppression.

In Quark-Gluon Plasma (QGP) phase scenario, strange quark-antiquark pairs are easily created, predominantly in gluon-gluon interactions. The gluon fusion processes, associated with partial restoration of chiral symmetry which lowers the mass of the strange quark, lead to a fast (a few fm/c) chemical equilibration of strangeness. As a result, the production of all hyperons, even the heaviest, is favoured. Therefore, strangeness enhancement with respect to a hadronic scenario is expected in the QGP phase i.e. the relative hyperon and anti-hyperon yields, with respect to their values measured in hadronic references, should increase with the hyperon mass. Such type of observations have been made by WA97 [61] and NA57 [62] collaboration at SPS energies.

Figure 1.10 (left and right) [62], shows hyperon and anti-hyperon yields observed in Pb+Pb interactions per event and per wounded nucleon and normalized to their corre-

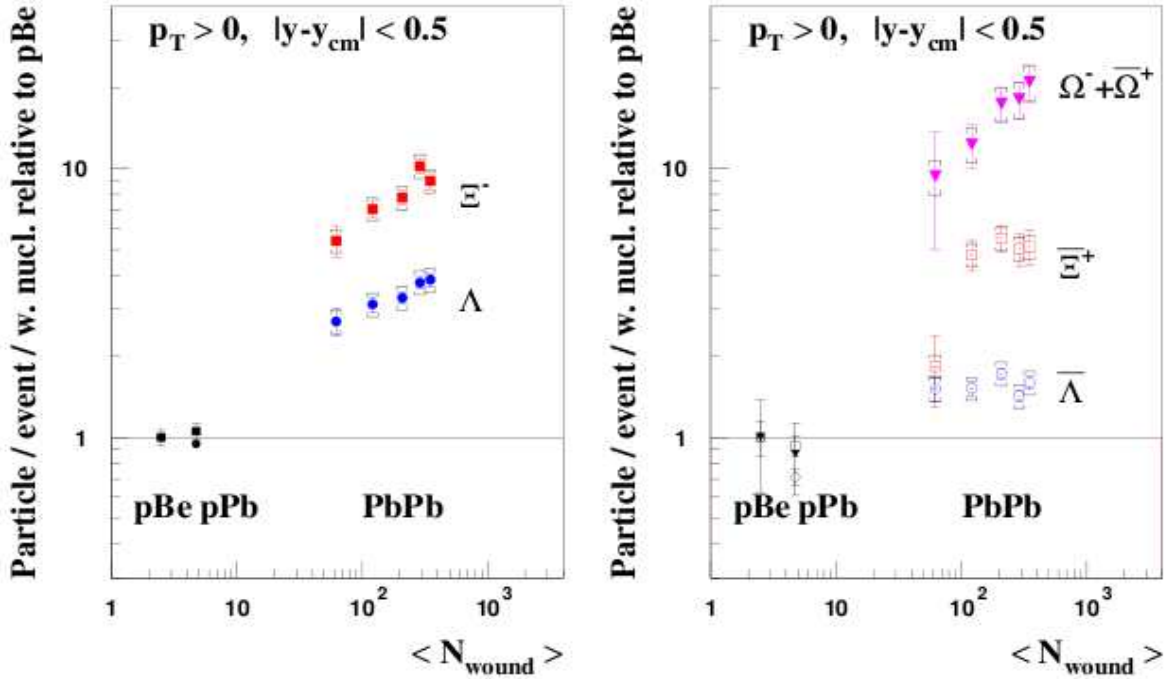


Figure 1.10: Hyperon and anti-Hyperon yields per number of wounded nucleons, expressed in units of corresponding yield per collision in p-Be reactions, measured at SPS 17.3 GeV by NA57.

sponding values in the hadronic reference p-Be interactions as a function of centrality, given by the average number of wounded nucleons. This effect has been considered as a strong footprint of the QGP phase because the observed enhancement (for Ω in the most central bin) was found to be in good agreement with the values expected in the case of QGP phase formation.

Also Rafelski and Danos [63] suggest that one should look for strange particles with relatively large transverse momentum (say P_t greater than 1 GeV/c), as these are ex-

pected to originate from the early conditions of the Quark-Gluon Plasma (QGP), these should be more favourable to the observation of the QGP phase than in the entire range of transverse momentum (P_t), because of the large number of low P_t particles produced during the hadronization phase. In this context E802 experiment measured ratio of K^\pm to π^\pm in Si+Au central interactions at 14.5 GeV/nucleon [64] and observed net enhancement of K^+/π^+ relative to $p+p$. It was observed that the enhancement is more pronounced in K^+/π^+ than in K^-/π^- and increases with transverse momentum (P_t). The NA34 experiment measured the K^\pm and π^\pm transverse momentum and transverse mass spectra in $S+W$ interactions at 200 GeV/nucleon in the rapidity range of 1-1.3 and P_t range 0.15-0.45 GeV/c [65]. The spectrum of K^+ was observed to be flatter than the K^- , it could be due to an enhancement of the K^+/π^+ in the ions collisions relative to proton-proton collision. Also the transverse mass spectra of K^+ is flatter than the K^- spectrum, because it should reflect the behaviour of transverse momentum (P_t). Both E802 and NA34 experiments have measured K/π ratios, but E802 observed the excess of K/π relative to proton-proton at low value of P_t , outside the range of NA34 experiment.

Strangeness enhancement has been studied at the AGS, SPS and RHIC energies. The ratio of kaon to pion (K/π) production is often used to quantify the strangeness enhancement. The STAR experiment at RHIC studied the K/π ratio at mid-rapidity [67] shown in figure 1.11 as a function of collision energy in p+p and A+A collisions. There is a rapid increase in K^+/π^+ ratio from AGS to SPS energy. Then the ratio saturates and practically remains constant from $\sqrt{s_{NN}} \sim 10$ GeV to 130 GeV. The ratios are large in A+A collisions compared to p+p collisions at similar energies, which shows the strangeness enhancement.

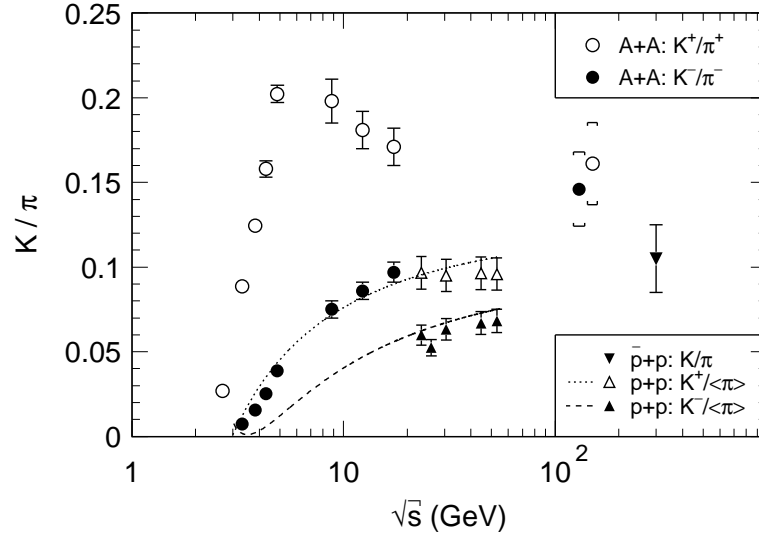


Figure 1.11: Mid-rapidity K/π ratio versus $\sqrt{S_{NN}}$. The curves are parameterizations to $p + p$ data [66]. The error are statistical.

1.6 Rapidity and Pseudorapidity Variables

Rapidity is related to velocity, as the name implies. It is dimensionless, and describes the rate at which a particle is moving with respect to a reference point on the line of motion. Rapidity is often used as one of the kinetic variables in high-energy collisions. It has the advantage of being additive under Lorentz transformations. Mathematically rapidity (y) is defined as [4]:

$$\text{rapidity } (y) = \frac{1}{2} \ln \left[\frac{E+p_z}{E-p_z} \right] \quad (1.2)$$

where E is the total energy of the particle and p_z is the z component of the momentum. Unlike velocity, rapidity is not a 3 dimensional vector; it is a scalar quantity associated with the z -axis. E and p_z can be expressed in terms of rapidity as follows:

$$E^2 = p^2 + E_0^2 = m_t^2 + p_z^2 \quad (1.3)$$

where:

$$p^2 = p_x^2 + p_y^2 + p_z^2 \quad (1.4)$$

$$m_t^2 = E_0^2 + p_x^2 + p_y^2 \quad (1.5)$$

we can see that m_t , the transverse mass, is Lorentz invariant, since p_x and p_y are perpendicular to the beam axis and E_0 is a constant. Finally, from the above relations we are able to express E and p_z in rapidity with the relations:

$$E = m_t \cosh y \quad (1.6)$$

$$\text{and } p_z = m_t \sinh y \quad (1.7)$$

equation (1.2) can be rewritten as:

$$y = \frac{1}{2} \ln \left[\frac{1 + \beta \cos \theta}{1 - \beta \cos \theta} \right] \quad (1.8)$$

where β is defined as the velocity divided by the speed of light i.e. $\beta = v/c$ and θ is the particle emission angle with respect to the beam axis.

In the limit of equation (1.8) as $\beta \rightarrow 1$, we derive a related quantity called the pseudorapidity (η):

$$\eta = -\ln \tan \left[\frac{\theta}{2} \right] \quad (1.9)$$

In practice, it is much easier to measure the pseudorapidity (η) of a particle since one only need knowledge of the angle of emission, while rapidity requires knowledge of the particle's angle and velocity.

1.7 Theoretical Models in Relativistic Heavy-Ion Collisions

In order to understand the real data in relativistic heavy-ion collisions, it is necessary to compare the experimental data with the corresponding results from theoretical models. Starting from the particle production in from Monte Carlo code of a model till the particle gets detected, one has to simulate all possible interactions taking place in the experiment to obtain simulated data which can be analysed for comparison with experimental data. There are various models (event generators) like AMPT (A Multi-Phase Transport) [68], UrQMD (string hadronic cascade model) [25], HIJING (Heavy-Ion Jet Interaction Generator) [69, 70] etc which are used to study the particle production and their final properties. Every event generator has its own physics goal and suitable for different energies scenario. For analysis presented in this thesis Heavy Ion Jet Interaction Generator (HIJING) version 1.38 and A Multi-Phase Transport (AMPT) model are used.

1.7.1 Heavy-Ion Jet Interaction Generator (HIJING) Model

HIJING is a Monte-Carlo based event generator for parton and particle production in high energy hadronic and nuclear collisions [69, 70]. In high energy heavy-ion collisions, it is expected that hard or semihard parton scatterings with transverse momenta of a few GeV/c will dominate. HIJING is based on QCD-inspired models for multiple jet production with Lund model [71] for jet fragmentation, in particular to study the jet and mini-jet production together with associated particle in high energy pp , pA and AA collisions. This model incorporates mechanisms such as multiple minijet production, soft excitation, nuclear shadowing of parton distribution functions and jet interactions in dense hadronic matter. HIJING is very useful in reproducing many inclusive spectra,

two particle correlations, and explains the observed flavor and multiplicity dependence of the average transverse momentum at Relativistic Heavy-Ion Collider (RHIC) energies. However, this event generator doesn't include the secondary interactions.

1.7.2 A Multi-Phase Transport (AMPT) Model

A Multi-Phase Transport (AMPT) model has been developed to study high energy heavy-ion collisions at SPS, RHIC and even higher energies such as the LHC. The AMPT model consists of four main components: the initial condition, partonic interactions, the conversion from partonic matter to hadronic matter, and hadronic interactions. The initial condition, which includes the spatial and momentum distributions of minijet partons and soft string excitations, are obtained from the HIJING model [69, 70, 72, 73]. The scatterings among partons are modeled by Zhang's parton cascade (ZPC) [74]. The Lund string fragmentation model [75, 76] as implemented in JET-SET/PYTHIA to convert the excited strings to hadrons in the default model or a simple quark coalescence model to convert partons into hadrons in the case of string melting and the extended relativistic transport (ART) model [77] for describing interactions among hadrons. AMPT model has been used to study various observables in heavy-ion collisions at SPS and RHIC energies and to address the relative importance of partonic and hadronic effects on these observables. In particular, the AMPT has been used to study the rapidity distributions of particles such as pions, kaons, protons and antiprotons, their ratios, their transverse momentum spectra, the elliptic flow and the interferometry of two identical mesons. Also the AMPT model can be extended to include hydrodynamic evolution at the early stage when local thermalization is likely, in order to conveniently study the equation of state of the partonic matter and help us to learn from relativistic heavy ion collisions the properties of the Quark-Gluon Plasma (QGP) state formed during the

early stage of the collisions.

1.8 Statement of the Problem

It has been argued that measurement of fluctuations in the produced particles in ultra-relativistic heavy-ion collisions can be a useful probe to understand the physics in high nuclear compression and temperature scenario. Besides these fluctuations are also a good indicator of the onset of de-confined state of nuclear matter. The present results from contemporary experiments at energies studied are not conclusive. It is therefore, useful to analyse data on the latest beam energies available.

The enhancement of strangeness production in the produced particles in ultra-relativistic heavy-ion collisions has been extensively studied as a possible signal for the production of deconfined state of matter in a variety of collisions systems and at different available energies. The results have been compared to hadron-hadron and hadron-nucleus data and positive results have been reported at SPS energies in many experiments. In the present analysis we have used data for Cu+Cu interactions at $\sqrt{S_{NN}} = 62.4$ and 200 GeV recorded by Time Projection Chamber (TPC) as a part of STAR (Solenoidal Tracker at RHIC) experiment at Brookhaven National Laboratory (BNL), New-York, USA. The strength of fluctuations in the produced charged particles has been measured on event-by-event basis. The analysis is done using sigma dynamic ($\sigma_{dynamic}$) and $\nu_{dynamic}$ variables. The centrality and energy dependence strength of fluctuations has been studied in detail in the context of model predictions. The studies have resulted in useful conclusions. The fluctuations quantum of dynamic origin do not seem to be significant for the collision analysed at RHIC energies.

Also Photon Multiplicity Detector (PMD) is installed as a part of the STAR exper-

iment at BNL, New-York, USA. We measured photon multiplicities in Cu+Cu interactions at $\sqrt{s_{NN}} = 62.4$ GeV in the forward rapidity region $2.3 \leq \eta \leq 3.8$. Systematic studies have been undertaken to gauge the fluctuations of data on event-by-event basis. HIJING Monte Carlo code and CERN GEANT codes have been used to generate events and simulate detector geometry to produce simulated data for comparison. The model calculations reasonably reproduce the experimental data on photon multiplicity distributions.

Bibliography

- [1] Introduction to Particle Physics by Donald H. Perkins.
- [2] W. M. Yao et al. (Particle Data Group Collaboration), Review of particle physics, J. Phys. G33, 1 (2006).
- [3] D. J. Griffiths, Introduction to Elementary Particles (Wiley, New York, US, 1987).
- [4] C. Y. Wong, Introduction to high-energy heavy ion collisions, Singapore, Singapore: World Scientific (1994) 516 p.
- [5] P. Braun-Munzinger, Chemical equilibration and the hadron-QGP phase transition, Nucl. Phys. A681, 119 (2001), nucl-ex/0007021.
- [6] D. H. Rischke, Nucl. Phys. A 698, 153-163 (2002).
- [7] L. Van Hove, Phys. Lett. B 118, 138 (1982).
- [8] L. D. Landau, Izv. Akad. Nauk SSSR Ser. Fiz. 17, (1953) 51; Collected papers, Ed. D. Ter Haar (Pergamon, Oxford, 1965) p.569.
- [9] T.H. Burnett et al., Phys. Rev. Lett. 57 (1986) 3249.
- [10] E.V. Shuryak and O. Zhirov, Phys. Lett. B171(1986) 99.
- [11] M. M. Aggarwal et al., Phys. Rev. Lett. 85, 3595 (2000).
- [12] T. Matsui and H.Satz, Phys. Lett. 178 B (1986) 416.

- [13] M. Gonin et al., Nucl. Phys. A 610, 404c (1996).
- [14] M.C. Abreu et al., Nucl. Phys. A 661, 93 (1999).
- [15] M.C. Abreu et al., Phys. Lett. B 477, 28 (2000).
- [16] M. Stephanov, K. Rajagopal, and E. Shuryak, Phys. Rev. Lett. 81 (1998) 4816.
- [17] Q. Liu and T. Trainor, Phys. Lett. B567 (2003) 184.
- [18] M. Gazdzicki and St. Mrowczynski, Z. Phys. C54 (1999) 127.
- [19] S. Mrowczynski, Phys. Lett., B430 (1998) 9; Phys. Lett. B459, (1999) 13; M. Gazdzicki and S.Mrowczynski, Z.Phys., C54 (1992) 127.
- [20] S. A. Voloshin et al., Phys. Rev. C60(1999) 204901.
- [21] H. Appelshauser et al., (NA49 Collaboration) Phys. Lett. B459(1999) 679-686;S.V. Afanasev et al(NA49 collaboration), hep-ex/0009053
- [22] S. V. Afanasev et al.,(NA49 Collaboration), Phys. Rev. Lett. 86, 1965 (2001), [arXiv:hep-ex/0009053].
- [23] C. Roland, (for the NA49 Collaboration) J. Phys. G: Nucl. Part. Phys. 30 (2004) S1381-S1384.
- [24] C. Roland, (for the NA49 Collaboration), J.Phys. G: Nucl. Part. Phys. 31 (2005) S1075-S1078.
- [25] Bleicher M et al. 1999 J. Phys. G25 1859.
- [26] Gazdzicki M (for the NA49 Collaboration) 2004 Preprint nucl-ex/0403023.
- [27] L. Stodolsky, Phys. Rev. Lett. 75, 1044 (1995).
- [28] E. V. Shuryak, Phys. Lett. B423, 9 (1998), [arXiv:hep-ph/9704456].

- [29] L. Landau and L. Lifshitz, Statistical Physics (Pergamon Press, New York, 1980).
- [30] K. Stephanov, K. Rajagopal, and E. Shuryak, Phys.Rev.D60(1999) 114028.
- [31] PHENIX, K. Adcox et al., Phys. Rev. C66, 024901 (2002).
- [32] D. Adamova et al., (CERES Collaboration) Nucl. Phys. A727, 97 (2003).
- [33] J. Adams et al., (STAR Collaboration), [arXiv:nucl-ex/0308033].
- [34] M. Asakawa, U. W. Heinz, and B. Muller, Phys. Rev. Lett. 85, 2072 (2000).
- [35] S. Jeon and V.Koch, Phys. Rev. Lett. 85, 2076 (2000).
- [36] J. Adams et al., Phys. Rev. C68, 044905 (2003).
- [37] H. Appelshauser et al., (CERES Collaboration), Nucl. Phys. A 752, 394 (2005).
- [38] C. Blume et al., (2002), [arXiv:nucl-ex/0208020].
- [39] J. Zaranek, Phys. Rev. C66, 024905 (2002), [arXiv:hep-ph/0111228].
- [40] A. Bialas, Phys. Lett. B532, 249 (2002), [arXiv:hep-ph/0203047].
- [41] Henning Heisenberg, nucl-th/0003046.
- [42] A. Bialas and V. Koch, Phys. Lett. B456 (1999) 1.
- [43] X-N. Wang and M. Gyulassy, Phys. Rev. Lett. 68, 1480 (1992).
- [44] M. Gyulassy and M. Plumer, Phys. Lett. B 243, 432 (1990).
- [45] M. gyulassy and X-N. Wang, Nucl. Phys. A 590, 511C (1995).
- [46] M. Gyulassy, Nucl. Phys. B571, 197 (2000).
- [47] M. Gyulassy, Nucl. Phys. A661, 637 (1999).

- [48] C. Adler et al ., Phys. Rev. Lett. 89, 202301 (2002).
- [49] A. Poskanzer and S. Voloshin, Phys. Rev. C 58, 1672 (1998).
- [50] Introduction to Relativistic Heavy Ion Collisions, L. P. Csernai.
- [51] N.S. Amelin, E. F. Staubo, L. P. Csernai, V. D. Toneev, K. K. Gudima and D. Strottman, Phys. Rev. Lett, 67, 1523 (1992).
- [52] L. P. Csernai and J. I. Kapusta, Phys. Rev. Lett, 69, 737 (1992).
- [53] J.Y. Ollitrault, Phys. Rev. D46 (1992) 229. See also J.Y. Ollitrault, Nucl. Phys. A638 (1998) 195c .
- [54] J. Barrette et al. (E877 collaboration), Phys. Rev. C55 (1997) 1420 .
- [55] A.M. Poskanzer and S.A. Voloshin and the NA49 collaboration, Nucl. Phys. A661 (1999) 341c .
- [56] C. Adler et al. (STAR collaboration), Phys. Rev. Lett. 87 (2001) 182301 .
- [57] P.F. Kolb and U. Heinz, hep-ph/0204061 .
- [58] U. Heinz and P.F. Kolb, Nucl. Phys. A 702 (2002) 269 .
- [59] P. Koch, B. Muller and J. Rafelski, Phys. Rep. 142 (1986) 167.
- [60] J. Rafelski, Phys. Rept. 88, 331 (1982).
- [61] E. Anderson and the WA97 Collaboration, Phys. Lett. B449 (1999) 401.
- [62] V. Manzari for the NA57 Collaboration, Nucl. Phys. A715 (2003) 140c.
- [63] J. Rafelski and M. Danos, Phys. Lett. B192 (1987) 432.

- [64] S.G Steadman et al., E802 Collaboration, Hadronic Matter in collision 1988, Tucson, Arizona, USA., October 6-12, 1988, P. Carruthers and J. Rafelski (World Scientific, 1989) P. 607.
- [65] G. London et al., NA34 Collaboration, Proceedings of the Int. Europhysics Conf. on High Energy Physics, Madrid, Spain, September 6-13, 1989 (North Holland, Amsterdam, in the press).
- [66] A.M. Rossi et al., Nucl.Phys. B 84, 269 (1975); J.L. Bailly et al. (NA23 Collaboration), Phys. Lett. B 195, 609 (1987).
- [67] C. Adler et al., STAR Collaboration, Phys. Lett. B 595, 143 (2004).
- [68] B. Zhang, C. M. Ko, B. A. Li, and Z. Lin, Phys. Rev. C 61, 067901 (2000).
- [69] M. Gyulassy and X. N. Wang, Comput. Phys. Commun. 83, 307 (1994).
- [70] X. N. Wang, Phys. Rev. D 43, 104 (1991).
- [71] B. Anderson et al., Phys. Rep. 97, 13 (1983).
- [72] X. N. Wang and M. Gyulassy, Phys. Rev. D 44, 3501 (1991).
- [73] X. N. Wang and M. Gyulassy, Phys. Rev. D 45, 844 (1992).
- [74] B. Zhang, Comput. Phys. Commun. 109, 193 (1998).
- [75] B. Andersson, G. Gustafson and B. Soderberg, Z. Phys. C 20, 317 (1983).
- [76] B. Andersson, G. Gustafson, G. Ingelman and T. Sjostrand, Phys. Rept. 97, 31 (1983).
- [77] B. A. Li and C. M. Ko, Phys. Rev. C 52, 2037 (1995).

Chapter 2

STAR Experiment at RHIC

2.1 Relativistic Heavy-Ion Collider (RHIC)

Experimental attempts to create the Quark-Gluon Plasma (QGP) state in the laboratory and measure its properties have been carried out for more than two decades, by studying collisions of heavy nuclei and analyzing the fragments and produced particles emanating from such collisions. During this period, center of mass energies per pair of colliding nucleons have risen steadily from the $\sqrt{s_{NN}} \sim 1$ GeV domain of the Bevalac at Lawrence Berkeley National Laboratory (LBNL), to energies of $\sqrt{s_{NN}} = 5$ GeV at the AGS at Brookhaven National Laboratory (BNL), and to $\sqrt{s_{NN}} = 17$ GeV at the SPS accelerator at CERN, Geneva. No decisive proof of QGP formation was found in the experiments at these energies, although a number of positive signals were observed suggesting the formation of a very dense state of matter, possibly partonic, were found at the SPS [1, 2]. With the Relativistic Heavy Ion Collider (RHIC), at Brookhaven National Laboratory (BNL), the center of mass energy in central collisions between Au+Au, Cu+Cu nuclei at 100 A GeV + 100 A GeV is almost 40 TeV, the largest so far achieved in nucleus-nucleus collisions under laboratory conditions. This energy is so large that conversion of a sizeable fraction of the initial kinetic energy into matter production cre-

ates many thousands of particles in a limited volume leading to unprecedented large energy densities and thus presumably ideal conditions for the formation of the Quark Gluon Plasma state.

Figure 2.1 shows the aerial view of the Brookhaven National Laboratory (BNL). It is situated on the long-island at Upton in New-York, USA. BNL is a multipurpose research institution and was established in 1947 for the peacetime exploration of science. It is funded primarily by the Office of Science of the U.S. Department of Energy (DOE), the laboratory houses large scale instruments and facilities -some available nowhere else in the world. Upto date six Noble-Prize winning discoveries and countless other advances have their origins at the lab. Scientists from all over the world used the BNL facilities to develop into the basic mysteries of physics, chemistry, biology, materials science, energy and the environment.

A Relativistic heavy-ion Collider (RHIC) is the world class particle accelerator at Brookhaven National Laboratory (BNL), USA where physicists are exploring the most fundamental forces and properties of matter and the early universe, with important implications for our understanding of the world around us. A schematic diagram of the Relativistic Heavy Ion Collider (RHIC) complex at BNL are displayed in figure 2.2.

RHIC at Brookhaven National Laboratory, USA is the first Hadron accelerator and collider. RHIC's ring has six interaction points where its two rings of accelerating magnets cross, allowing the particle beams to collide. The collisions produce the fleeting signals that, when captured by one of RHIC's experimental detectors, provide physicists with information about the most fundamental working of nature. The RHIC's ring have a clock face, where the STAR is located at 6 o'clock, PHENIX at 8 o'clock, PHOBOS



Figure 2.1: Aerial view of Brookhaven National Laboratory (BNL), Upton, New-York, USA.

at 10 o'clock and BRAHMS at 2 o'clock.

The RHIC having two rings of superconducting magnets, the Alternating Gradient Synchrotron (AGS), the Booster Synchrotron, and the Tandem Van de Graaff (TVDG). The construction of RHIC begun during 1991 and was completed in 1999. Approximately \$ 500 million was spend for constructing such a big collider ring. As of present times RHIC is the world's foremost facility for basic research in nuclear and particle physics. It is designed in such a way to operate at high collision luminosity over a wide range of beam energies and with particle species ranging from polarized protons to heavy ions. RHIC has the capability of accelerating and colliding different combination of ion species such as: p+p, d+Au, Au+Au and Cu+Cu over a range of energies (upto 250 GeV for protons and 100 GeV/nucleon for heavy-ions). Each ion can be accelerated to nearly the speed of light. Each RHIC rings have a circumference of 3.8 Km, which accelerator, focus and guide the beams.

2.2 Different Experiments at RHIC

Relativistic Heavy-Ion Collider (RHIC) presents a formidable environment in which head-on symmetrical collisions of two large nuclei (Au,Cu etc) produce around 1000 particles per unit pseudorapidity. RHIC's 3.8 km rings have six interaction points where the two beams collide. These collisions provide physicists working at the experimental detectors with information about fundamental nuclear phenomena. There are currently three experiments namely Solenoidal Tracker at RHIC (STAR) [3], Pioneering High Energy Nuclear Interaction Experiment (PHENIX) [4] and Broad Range Hadron Magnetic Spectrometers (BRAHMS) [5] operating at RHIC taking various approaches to search for Quark Gluon Plasma [6]. The PHOBOS (named after moon of Mars) [7] experiment

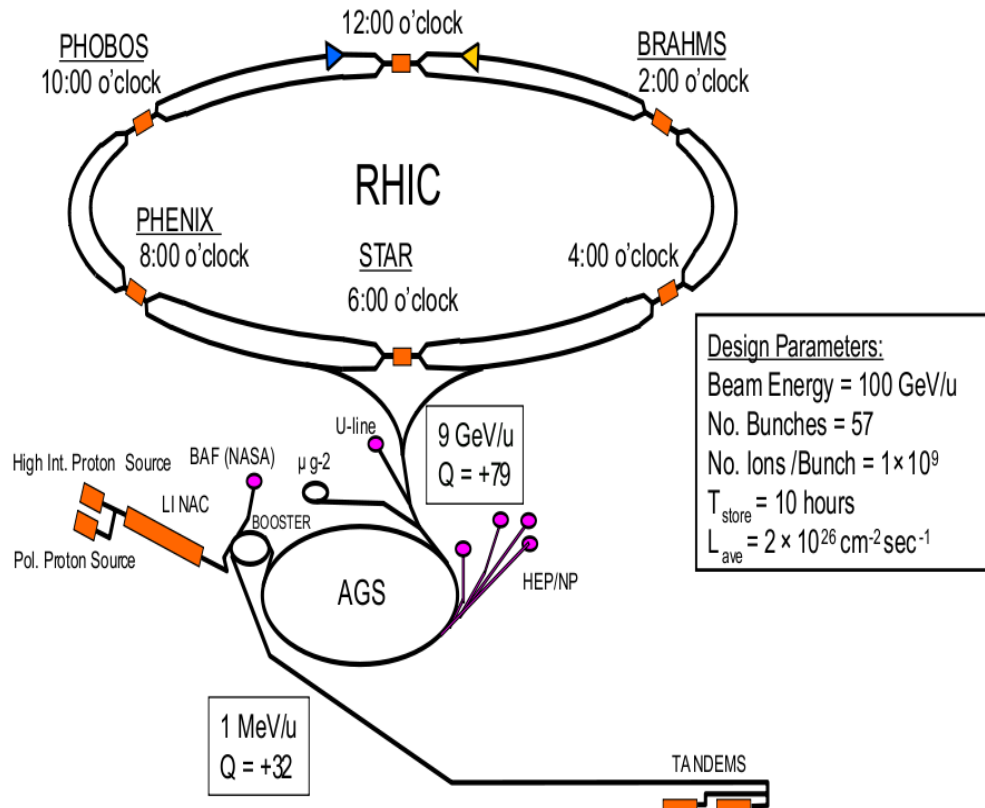


Figure 2.2: The Relativistic Heavy Ion Collider (RHIC) accelerator complex at Brookhaven National Laboratory. Nuclear beams are accelerated from the Tandem Van de Graaff, through the transfer line into the AGS Booster and AGS prior to injection into RHIC.

completed its data taking in the year 2005.

2.2.1 PHOBOS Experiment

The PHOBOS experiment named after a moon of Mars. It consisted of a two-arm magnetic spectrometer as its central detecting system and a series of silicon detectors surrounding the interaction region. The PHOBOS concepts was based on the premise that interesting collisions will be rare but that when they do occur the new physics will be readily identified. Thus the PHOBOS detector was designed to be able to examine and analyze a very large number of unbiased collisions (Au+Au, Cu+Cu Collisions). For each collision the detector gives a global picture and detailed information about a small subset of the nuclear fragments ejected from the high energy density region. The PHOBOS detector was able to measure quantities such as the temperature, size and density of the fireball produced in the collision. It also studied the ratios of the various particles produced in the collision. PHOBOS collaboration at RHIC reports measurement of charged particle multiplicity at mid-rapidity [8, 9, 10].

2.2.2 PHENIX Experiment

Pioneering High Energy Nuclear Interaction Experiment (PHENIX), is an exploratory experiment for the investigation of high energy collisions of heavy ions and protons. PHENIX is designed specifically to measure direct probes of the collisions such as electron, muons, and photons. The primary goal of PHENIX is to discover and study a new state of matter called the Quark-Gluon Plasma (QGP). PHENIX records many different particles emerging from RHIC collisions including: photons, electrons, muons and hadrons. Photons and leptons are not affected by the strong force, which binds

quarks and gluons together into hadrons. These particles can emerge unchanged from the interior of a collision, providing information about processes within the collision. It consists of a large acceptance charged particle detector and four spectrometer arms—a pair of which is used for detecting electrons, photons and hadrons at mid-rapidity, the other pair of spectrometers detecting muons at forward rapidity. There are also additional sub detectors for event characterization, which provide the information about the collision. There is a beam-beam counter which consists of two arrays of quartz Cherenkov telescopes surrounding the beam. There is a multiplicity and vertex detector composed of concentric barrels of silicon strip detectors together with end-caps of silicon pad detectors. PHENIX has also electromagnetic calorimeters mounted outside each of the two central arms.

At RHIC energies, the PHENIX experiment has observed significant yield of direct photons in Au+Au collisions at $\sqrt{s_{NN}} = 200$ GeV and find out the increase of $dN_{ch}/d\eta$ at mid-rapidity [11].

2.2.3 BRAHMS Experiment

The Broad Range Hadron Magnetic Spectrometers (BRAHMS) Experiment at RHIC consists of a two-arm magnetic spectrometer, one in forward direction for detecting high momentum particles but with small solid angle and other on the side of the collision point at mid-rapidity. Both the arms are moveable to variable settings to cover a wide ranges of kinematical regions. One of the physics goals of BRAHMS experiment is to study the reaction mechanisms of the relativistic heavy-ion reactions at RHIC energies and the properties of the highly excited nuclear matter formed in these reactions. The amount of stopping will be studied through the net baryon distributions. Some infor-

mation concerning the space-time characteristics of the system will be obtained from interferometry measurements in a limited rapidity and P_t range.

2.3 STAR Experiment

The Solenoidal Tracker at RHIC (STAR) is a major experiment, handled by 52 institutions from 12 countries, with a total of 594 collaborators. The STAR setup is a multi-detector system comprising of a large number of different type of detectors each dedicated to detecting certain types of particles and characterizing their motion. The STAR experiment [12] has been designed to investigate the behaviour of strongly interacting matter at high energy density and to search for signatures of Quark-Gluon Plasma (QGP) formation. The schematic layout of the STAR detector [13] is shown in figure 2.3. It is a large acceptance cylindrical detector system with a complete azimuthal coverage over a central rapidity region. The entire detector system is located within a 0.5 Tesla solenoidal analysing magnet. The solenoidal magnet [14] provides uniform magnetic field for charged particle momentum analysis.

2.3.1 Objectives of STAR

Solenoidal Tracker at RHIC (STAR) experiment measures many observables simultaneously to study signatures of a possible phase transition from hadronic matter to Quark-Gluon Plasma (QGP) state and to understand the space-time evolution of the collision process in ultra-relativistic heavy-ion collisions. The objective of STAR is to obtain a fundamental understanding of the microscopic structure of these hadronic interactions at high energy densities and temperature.

In relativistic heavy-ion collisions, the high track multiplicities allow for the extraction of the global observables such as centrality, temperature, reaction plane, and mean transverse energy. STAR experiment [12] has the capability to measure hadron production over a large solid angle, featuring detector systems for high precision tracking, momentum analysis, and particle identification at the center of mass rapidity. The large acceptance of STAR detector makes it particularly well suited for event-by-event characterizations of heavy-ion collisions and for the detection of hadron jets [3]. In addition STAR is also capable of investigating extreme peripheral collisions of nuclei at different relativistic energies [15].

2.3.2 STAR Magnet

The STAR magnet system was designed by R.D. Schlueter of Lawrence Berkeley National Laboratory [16]. The present design of the magnet produces a near uniform field over the operating range $0.25 < |B_z| < 0.5$ T parallel to the beam direction (z-direction) over the entire Time Projection Chamber (TPC) (described in next section) volume. The mapping of magnetic field was performed before the TPC installation. The radial component of the magnetic field (B_r) is measured at both ends of the TPC and the obtained value is approximately ± 25 Gauss for the half-field ($|B_z| = 0.25$ T) operation. The azimuthal component (B_ϕ) is less than ± 1.5 Gauss over the TPC volume.

The magnet is roughly cylindrical in geometry and consists of 30 flux return bars (backlegs), four end rings and two poletips. The 6.85 m long flux return bars are trapezoidal in cross section and weigh 18 tons each. They form the outer wall of the cylinder which encloses the main and space trim coils and are attached to an inner and outer end ring pair at each end of the magnet. The inner end rings have an inner diameter of

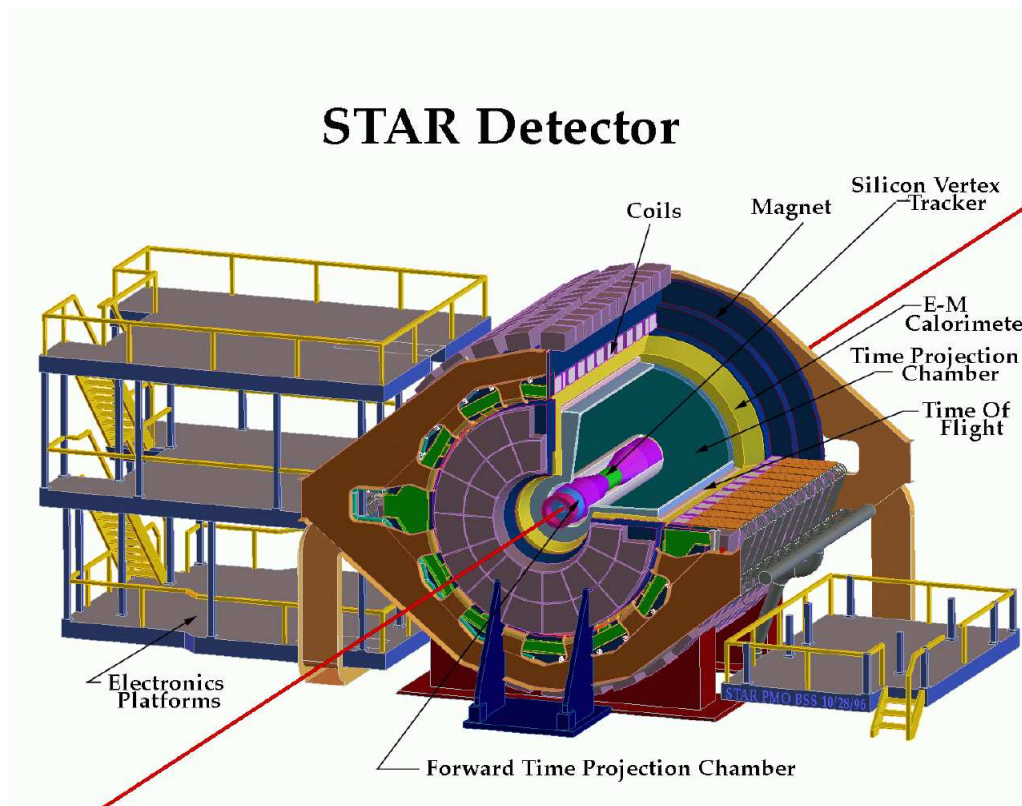


Figure 2.3: Schematic view of the STAR detector at Relativistic Heavy-Ion Collider (RHIC), BNL, USA.

5.27 m with 30 chord surfaces on the 6.28 m outer diameter to fix the azimuth location of each flux return bar. The outer rings are the structural connection between the ends of the flux return bars and have the same inner diameter as the inner rings with a 7.32 m outer diameter and 203 mm axial thickness, weighing 35 tons each. To maintain magnetic field quality, deflections in the magnet structure are minimized to less than 1 mm. The magnetic components were precision fabricated and mating connections used high strength bolts and pinned connections. More details of the magnet can be seen in [14].

2.4 STAR's Detector

The figure 2.4 shows the schematic cutway side view of the STAR's detector as configured for the RHIC runs. STAR experiment accommodated several detectors around the main tracking chamber. This includes Time Projection Chamber (TPC), Forward Time Projection Chamber (FTPC), Silicon Vertex Tracker (SVT), Silicon Strip Detector (SSD), Forward Pion Detector (FPD), Beam Beam Counter (BBC), Barrel Electromagnetic Calorimeter (BEMC), Endcap Electromagnetic Calorimeter (EEMC) and Photon Multiplicity Detector (PMD). These detectors greatly enhance the capabilities of STAR experiment to detect and identify high energy and rare short-lived particles. The data set used for present physics analysis is taken using the Time Projection Chamber (TPC) and Photon Multiplicity Detector (PMD) of STAR experiment. Details about TPC will be described in the following section and PMD will be described in chapter three.

2.4.1 Time Projection Chamber (TPC)

Time Projection Chamber is one of the most important tracking detectors in STAR experiment [17, 18, 19]. The TPC records the tracks of charged particles, measures their momenta and identifies the particles by measuring their ionization energy loss (dE/dx).

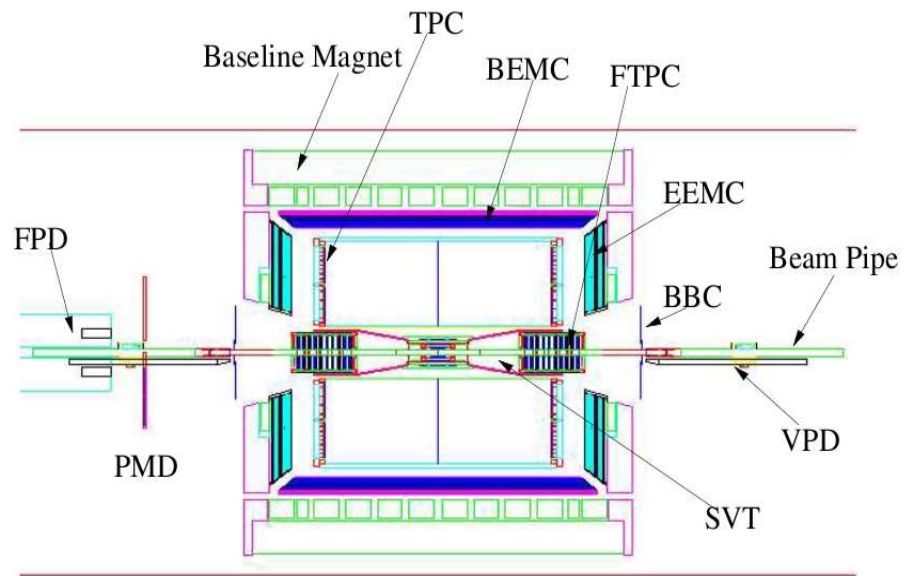


Figure 2.4: Schematic view and positions of different detectors in STAR experiment.

TPC acceptance covers ± 1.8 units of pseudorapidity through the full azimuthal angle. In STAR TPC with a magnetic field of 0.5 T, the particles are identified over a momentum range from 100 MeV/c to greater than 1 GeV/c and momenta are measured over a range of 100 MeV/c to 30 GeV/c.

2.4.1.1 Design of TPC

The figure 2.5 shows the schematically view of Time Projection Chamber (TPC). In STAR experiment, TPC is placed inside a large solenoidal magnet and is designed for a uniform maximum field of 0.5 T [16]. The TPC diameter is 4 m and 4.2 m long. It is an empty volume of gas in a well defined uniform electric field of ~ 135 V/cm. The paths of primary ionizing particles passing through the gas volume are reconstructed with high precision from the released secondary electrons which drift to the readout end caps at the ends of the chamber. The uniform electric field which is required to drift the electrons is defined by a thin conductive Central Membrane (CM) at the center of the TPC with identical concentric field cage cylinders and readout end caps on both sides. The uniformity of electric field is critical since track reconstruction precision is within few mm and electron drift paths are upto 2 m.

The TPC is a fully pixelized drift chamber with Multi-Wire Proportional Chambers (MWPC) at both ends for readout. The drifting electrons avalanche in the high fields at the 20 μm anode wires providing an amplification of 1000 to 3000. The positive ions created in the avalanche induce a temporary image charge on the readout pads which disappears as the ions move away from the anode wire. The image charge is measured by a preamplifier/shaper/waveform digitizer system. The induced charge from an avalanche is shared over several adjacent pads, so the original track position can be reconstructed

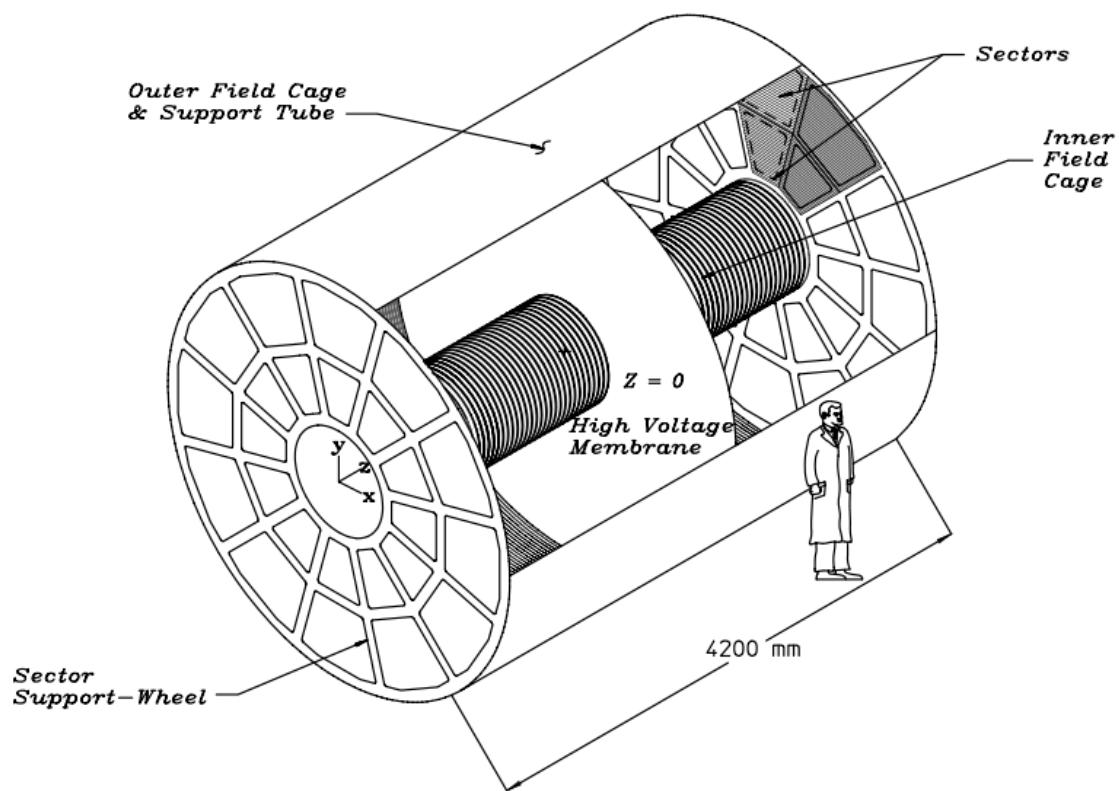


Figure 2.5: The STAR Time Projection Chamber (TPC) surrounds a beam-beam interaction region at RHIC. The collisions take place near the center of the TPC.

to a small fraction of a pad width. There are 136,608 readout pads. The x and y coordinates of a hits are determined by the charge measured on adjacent pads in a single pad row while the z coordinate of a point inside the TPC is determined by measuring the time of drift of a cluster of secondary electrons from the point of origin to the anodes on the endcap and dividing by the average drift velocity. The arrival time of the cluster is calculated by measuring the time of arrival of the electrons in “time buckets” and weighting the average by the amount of charge collected in each bucket.

The TPC is filled with P10 gas (10% methane and 90% argon) regulated at 2 *mbar* above atmospheric pressure [20]. It’s primary attribute is a fast drift velocity which peaks at a low electric field [21]. Operating on the peak of the velocity curve makes the drift velocity stable and insensitive to small variations in temperature and pressure. Low voltage greatly simplifies the field cage design. Charged particles can be detected in drift chambers because they ionize the gas along their flight path. The energy required for ionization is very small, typically few KeV per cm. When a charged particle traverses the TPC volume, it ionizes gas atoms and molecules in every few tenths of a millimeter along its path and leaving behind a cluster of electrons. Under the influence of an externally applied electric field, the electron clusters drift at a constant average velocity to the readout electronics where their time of arrival and location are recorded.

In table 2.1 some basic parameters for the Time Projection Chamber (TPC) in STAR experiment are listed for quick reference. Diffusion of the drifting electrons and their limited number defines the position resolution. Ionization fluctuations and finite track length limit the dE/dx particle identification. The design specifications were adjusted accordingly to limit cost and complexity without seriously compromising the potential for tracking precision and particle identification.

Item	Dimension	Comment
Length of the TPC	420 cm	Two halves, 210 cm long
Outer Diameter of Drift Volume	400 cm	200 cm radius
Inner Diameter of Drift Volume	100 cm	50 cm radius
Distance: Cathode to Ground Plane	209.3 cm	Each side
Cathode	400 cm diameter	At the center of the TPC
Cathode Potential	28 kV	Typical
Drift Gas	P10	10% methane, 90% argon
Pressure	Atmospheric +2 mbar	Regulated at 2 mbar
Drift Velocity	5.45 cm/ μ s	Typical
Number of Anode Sectors	24	12 per end
Number of Pads	136,608	
Magnetic Field	0, ± 0.25 T, ± 0.5 T	Solenoidal

Table 2.1: **Some basic parameters for the Time Projection Chamber (TPC) in STAR experiment and its associated hardware.**

2.4.1.2 Hit Resolution and Tracking Efficiency

The inner and outer sub-sectors have different size pads and so their two-hit resolutions are different. The efficiency depends on whether the track segment is observed in the inner or the outer sub-sectors. The efficiency is the ratio of the distributions of the distance separating two hits from the same event and two hits from different events. Two hits can be completely resolved when they are separated in the padrow direction (i.e. along the x axis) by at least 0.8 cm in the inner sector and 1.3 cm in the outer

sector. Similarly, two hits are completely resolved when they are separated in the drift direction (i.e. along the z axis) by 2.7 cm in the inner sector and 3.2 cm in the outer sector.

The TPC tracking efficiency depends on the acceptance of the detector, the electronics detection efficiency, as well as the two hit separation capability of the system. The acceptance of the TPC is 96% for high momentum tracks traveling perpendicular the beamline. The 4% inefficiency is caused by the spaces between the sectors which are required to mount the wires on the sectors. The software also ignores any space points that fall on the last two pads of a pad row. This fiducial cut is applied to avoid position errors that result from tracks not having symmetric pad coverage on both sides of the track. It also avoids possible local distortions in the drift field. The fiducial cut reduces the total acceptance to 94%.

The detection efficiency of the electronics is essentially 100% except for dead channels and the dead channel count is usually below 1% of the total. However, the system cannot always separate one hit from two hits on adjacent pads and this merging of hits reduces the tracking efficiency. The software also applies cuts to the recorded data. For example, a track is required to have hits on at least 10 pad rows because shorter tracks are too likely to be broken track fragments. But this cut can also remove tracks travelling at a small angle with respect to the beamline and low momentum particles that curl up in the magnetic field. Since the merging and minimum pad rows effects are non-linear, we can't do a simple calculation to estimate their effects on the data. We can simulate them, however.

In order to estimate the tracking efficiency, we embed simulated tracks inside real

events and then count the number of simulated tracks that are in the data after the track reconstruction software has done its job. The technique allows us to account for detector effects and especially the losses related to a high density of tracks. The simulated tracks are very similar to the real tracks and the simulator tries to take into account all the processes that lead to the detection of particles including: ionization, electron drift, gas gain, signal collection, electronic amplification, electronic noise, and dead channels.

2.4.1.3 Vertex and Momentum Resolution

The primary vertex can be used to improve the momentum resolution of the tracks and the secondary vertices can be separated from the primary vertices if the vertex resolution is good enough. Many of the strange particles produced in heavy ion collisions can be identified this way. The primary vertex is found by considering all of the tracks reconstructed in the TPC and then extrapolating them back to the origin. The global average is the vertex position. The primary vertex resolution is calculated by comparing the position of the vertices that are reconstructed using each side of the TPC, separately. As expected, the resolution decreases as the square root of the number of tracks used in the calculation. A resolution of nearly $350 \mu\text{m}$ is achieved when there are more than 1,000 tracks.

The transverse momentum (P_t), of a track is determined by fitting a circle through the x, y coordinates of the vertex and the points along the track. The total momentum is calculated using this radius of curvature and the angle that the track makes with respect to the z axis of the TPC. This procedure works for all primary particles coming from the vertex, but for secondary decays, such as λ or K_s , the circle fit must be done without reference to the primary vertex. The embedding technique is used to estimate

the momentum resolution. The track simulator was used to create a track with a known momentum. The track was then embedded in a real event in order to simulate the momentum smearing effects of working in a high track density environment.

2.4.1.4 Particle Identification

The details of the particle production and spectra are best understood when experiments provide results sorted by particle type. In order to provide particle identification, experiments must distinguish between particles with different masses. Charged particles passing through the Time Projection Chamber (TPC) lose energy via ionization. The total ionized charge collected from each hit on a track is proportional to the energy loss (dE/dx) of the particle.

Energy lost in the TPC gas is a valuable tool for identifying particle species. It works especially well for the low momentum particles but as the particle energy rises, the energy loss becomes less mass dependent and it is hard to separate particles with velocities greater than $0.7c$. In STAR experiment TPC is designed to be able to separate pions and protons up to $1.2 \text{ GeV}/c$ [21]. For a track crossing the entire TPC we obtain 45 dE/dx samples (coming from energy deposition in 45 layers), which are distributed according to the Landau probability distribution. The length over which the particle energy loss is measured is too short to average out ionizations fluctuations. Indeed, the particles lose energy going through the gas in frequent collisions with atoms where a few tens of eV are released [22]. Thus, it is not possible to accurately measure the average dE/dx . Instead, the most probable energy loss is measured. It is done by removing the largest ionization clusters. The truncated mean where a given fraction (about 30%) of the clusters having largest signal are removed. This is an efficient tool to measure the

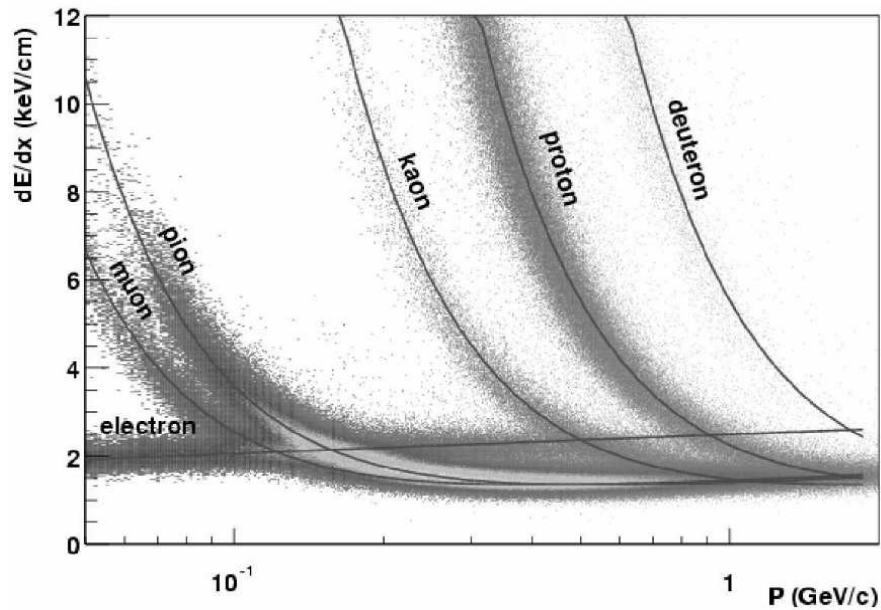


Figure 2.6: **Particles identification in STAR Time Projection Chamber (TPC).**

most probable dE/dx . However, fitting the dE/dx distribution including all the clusters associated to a given track has also been found to be more effective. It also allows one to account for the variation of the most probable energy loss with the length of the ionization samples (dx) [21].

Figure 2.6 shows the energy loss (dE/dx) for different produced particles in heavy ion collisions recorded in the Time Projection Chamber (TPC) as a function of the particle momentum. The charged pions and kaons can be identified upto about 0.75 GeV/c momentum and protons and deuteron can be identified upto 1.1 GeV/c. The data have been corrected for signal and gain variations and the data are plotted using a 70% truncated mean. The particles shown in figure 2.6 includes both primary and secondary particles. The prominent proton, deuteron, and muon bands come from secondary interactions in the beam pipe, and from pion and kaon decays.

In order to precisely identify a particle y , we define the variable $N_{\sigma y}$ (in the case of charged pion we write π in place of y) as:

$$N_{\sigma y} = \left[\frac{dE}{dx_{meas.}} - \langle \frac{dE}{dx} \rangle_y \right] / \left[\frac{0.55}{\sqrt{N}} \frac{dE}{dx_{meas.}} \right]$$

where N is the number of hits for a track in the TPC, $\frac{dE}{dx_{meas.}}$, is the measured energy loss of a track and $\langle \frac{dE}{dx} \rangle_y$ is the average energy loss for a particle type. In order to identify charged pion, kaon, proton and anti-proton, we can have similar definition of $N_{\sigma\pi}$, $N_{\sigma k}$, $N_{\sigma p}$. One can now apply suitable cuts on the variables $N_{\sigma\pi}$, $N_{\sigma k}$, $N_{\sigma p}$ etc to select different particles species[41].

2.4.2 Silicon Vertex Tracker (SVT)

In STAR experiment the detector closest to the primary collision is the Silicon Vertex Tracker (SVT) [24]. The SVT has the capability to enhance the primary vertexing, the two track separation resolution and the energy loss (dE/dx) measurement of STAR TPC. Apart from this, it also enables the reconstruction of very short-lived particles through secondary vertexing close to the interaction zone. The SVT covers the pseudorapidity range of $\eta \leq 1$ with full azimuthal coverage. It is a micro-vertex detector implemented in the novel drift detector technology. The SVT consists of 216 Silicon Drift Detectors containing over 13 million pixels multiplexed onto just 1300 readout channels. The Silicon Drift Detectors are arranged in three cylindrical layers at distances of about 7, 11 and 15 cm from the beam axis. The Silicon Drift Detectors has the pixel-like readout which created the high multiplicity environment in heavy-ion collisions at RHIC energies. It also expands the kinematical acceptance for primary particles to very low momentum

by using independent tracking in the SVT alone for charged particles that do not reach the active volume of the TPC due to the applied magnetic field. The SVT is based on silicon drift technology in order to handle the expected high charge multiplicities and to minimize the number of readout channels [25, 26].

2.4.3 Forward Time Projection Chamber (FTPC)

The Forward Time Projection Chamber (FTPC) was designed to extend STAR tracking capability in the forward region ($2.5 < \eta < 4.0$) with complete azimuthal coverage [27]. It consists of two identical chambers located within the TPC inner field cage, close to the beam pipe at ± 1.5 m from the center of the TPC (defined as $z=0$). The FTPC has a cylindrical structure, 75 cm in diameter and 120 cm long. The FTPC is similar to the STAR TPC, with the exception that the drift direction of the electrons is radial as opposed to axial, with respect to the beam axis. This radial drift configuration was chosen in order to optimize the two-track separation in the region close to the beam pipe where the particle density is highest [28]. The field cage is formed by the inner HV-electrode, a thin metalized plastic tube, and the outer cylinder wall at ground potential. The field region at both ends is closed by a planer structure of concentric rings, made of thin aluminum pipes. In FTPC the Front-End electronics (FEE), which amplifies and digitizes the signals, is mounted on the back of the readout chambers. The FTPC is a gas detector used Argon and Carbon Dioxide in the ratio of 50:50 was meticulously selected as it is non-flammable and shows no or little ageing effect in comparison to hydrocarbons. In FTPC the construction of the tracks is done by calculating the tracks points from the charged distribution measured by the readout electronics. The design of the front end electronics closely follows that of the TPC [29].

2.4.4 Silicon Strip Detector (SSD)

The Silicon Strip Detector (SSD) [30, 31] enhance the capabilities of STAR detector by measuring accurately the two dimensional hit position and energy loss of charged particles. It constitutes the fourth layer of the inner tracking system. It has been installed between the Silicon Vertex Tracker (SVT) and the Time Projection Chamber (TPC). It also helps in improving the extrapolation of TPC tracks through SVT hits and measuring the average number of space points measured near the collision thus increasing the detection efficiency of long-lived meta-stable particles. The SSD is built into two half barrels allowing a clamshell structure of the ensemble [32]. It consists total 4,91,520 readout channels which are divided into four sectors, two clamshells shared in two (the p and the n) side of the SSD. It is placed at a distance of 23 cm from the beam axis covering a pseudorapidity range of $\eta < 1.2$, which leads to a total required silicon surface close to $1m^2$ [31]. The SSD has 20 space frame carbon beams each supporting 16 detection modules. Each module is composed of one double-sided SDD and two hybrid circuits equipped with analogue readout electronics. At the arrival of a trigger, the readout board freezes the data in the Front-End electronics (FEE). It then reads all the Front-End channels and sends the data via an optical fiber to the DAQ receiver board. When the slow control needs to access the Front-End borads, it reconfigures the readout board such that no trigger is accepted.

2.4.5 Zero Degree Calorimeter (ZDC)

In Relativistic Heavy-Ion Collider (RHIC) experiment a pair of Zero Degree Calorimeter (ZDC) detectors [33] is constructed to provide the accelerators operators a common tool for monitoring interactions at each region. These are placed at nearly identical positions along the beamlines on either side of the intersection regions. In the zero degree

region produced particles and other secondaries deposit negligible energy when compared with that of the beam fragmentation neutrons. The Zero Degree Calorimeters (ZDCs) is designed to detect neutrons emitted within the cone ($|\theta| < 2$ milliradians) along both beam directions and measure their total energy. The energy measured by the Zero Degree Calorimeters (ZDCs) is proportional to the neutron multiplicity, which is known to be correlated with the event geometry and can be used to measure collision centrality. The Zero Degree Calorimeters (ZDCs) are hadronic calorimeters using layers of tungsten absorbers together with Cherenkov fibres. Light generated in the fibres is directed to three Photo-Multiplier Tubes (PMT) [33]. The Zero Degree Calorimeters (ZDCs) operate as fast detectors and also used for beam monitoring, triggering and locating interaction vertices. The hadronic minimum bias trigger requires a coincidence between the two STAR ZDCs of summed signals greater than $\sim 40\%$ of a single neutron signal. Comparison of the times from ZDC east and ZDC west gives a measure of the interaction location.

2.4.6 Central Trigger Barrel (CTB)

The Central Trigger Barrel (CTB) is designed to be part of the trigger system for the STAR detector. The CTB measures the charged particle multiplicity. The CTB is made up of 240 scintillator slats placed around the exterior of the Time Projection Chamber (TPC), resulting in a pseudorapidity coverage of $-1 < \eta < 1$. Each scintillator slat is 1 cm thick by 21 cm wide. Each slat consists of a radiator, light guide and mesh dynode Photo-Multiplier Tube (PMT). The PMT tubes are attached to the radiators using ultraviolet transmitting acrylic plastic light guides. Each PMT is powered by a channel of LeCroy 1440 high voltage and has an independent light emitting diode (LED)

attached to the far end of the slat for calibration purposes.

2.4.7 Barrel Electromagnetic Calorimeter (BEMC)

The Barrel Electromagnetic Calorimeter (BEMC) [34] is installed in the STAR experiment to look for high P_t processes like: jets, leading hadrons, direct photons, heavy quarks etc. The calorimeter permits the reconstruction of the neutral pion's from their decay photons at relatively high $P_t \sim 25\text{-}30$ GeV/c. Further, it is capable of identifying single electrons and electrons pairs in dense hadron backgrounds from heavy vector mesons, W and Z decays. All these measurements require precise electromagnetic shower reconstruction with high spatial resolution. The BEMC is a sampling calorimeter using lead and plastic scintillators. The BEMC electronics includes trigger, readout of phototubes and shower maximum detector (SMD), high voltage system for phototubes, low voltage power, slow controls functions, calibration controls and interfaces to the STAR trigger system.

2.4.8 Beam Beam Counter (BBC)

The role of Beam Beam Counter (BBC) in the STAR experiment is to provide a crucial minimum bias trigger for $p + p$ collision. In terms of the trigger, the main difference between $p + p$ and $Au + Au$, $Cu + Cu$ collisions is the multiplicity. Apart from providing a minimum bias trigger for $p + p$ collisions, BBC coincidences were used to reject beam gas events, to measure the absolute beam luminosity with 15% precision, and to measure the relative luminosities for different proton spin orientations with high precision.

The STAR Beam-Beam Counters (BBC) consists of large and small hexagonal scin-

tillator tiles. They are mounted around beam pipe on the east and west sides outside the pole-tip of the STAR magnet at ± 3.7 m from the interaction point. The 2×18 array of small hexagonal tiles cover a full ring of 9.6 cm inner and 48 cm outer diameter, corresponding to the pseudorapidity region of $3.4 < |\eta| < 5.0$. The small hexagon in the center of the BBC is reserved for the beam pipe. The 2×18 arrays of large hexagonal tiles span a ring of 38 cm to 193 cm in diameter, corresponding to the pseudorapidity region of $2.1 < |\eta| < 3.6$. Each scintillator tile has four wavelength shifting (WLS) optical fibres inserted into circular groves inscribed within the hexagonal scintillator to collect scintillation light. The timing difference between the two counters is used to locate the primary vertex position.

2.4.9 Photon Multiplicity Detector (PMD)

The Photon Multiplicity Detector (PMD) in the STAR experiment is dedicatedly constructed to detect photons in the forward rapidity region in nucleus-nucleus collisions at RHIC energies [35, 36]. It consists of two plane one is charge particle veto (CPV) and second is preshower plane of an array of cellular gas proportional counters using *Ar* and *CO₂* gas mixture. Both the planes are separated by a converter consisting of a 15 mm thick Pb plane and a stainless steel support structure in the form of a 5 mm thick plate. The PMD enhances the phase space coverage of the STAR experiment by covering a pseudorapidity region $2.3 \leq \eta \leq 3.8$ with full azimuthal coverage. This region has been selected to minimize the effect of upstream materials and to maximize the overlap with the coverage of the Forward Time Projection Chamber (FTPC) [37]. The detector is mounted on the east side of the STAR Wide Angle Hall (WAH) and is located at 540 cm from vertex and kept outside the STAR magnet. Details about physics objectives, design and working described in chapter three.

2.5 Data Acquisition System (DAQ) and Triggering in STAR

Data acquisition system [38] in STAR experiment is fast and flexible. It receives data from multiple detectors and these detectors have a wide range of readout rates. The event size is of order 200 MB and the events are processed at input rates up to 100 Hz. The STAR Trigger system [39] is a 10 MHz pipelined system which is based on input from fast detectors to control the event selection for the much slower tracking detectors. The trigger system is functionally divided into different layers with level 0 being the fastest while level 1 and level 2 are slower but they apply more sophisticated constraints on the event selection. STAR detector has a third level trigger [40] which performs complete online reconstruction of the events in a dedicated CPU farm. The level 3 trigger can process central Au+Au, Cu+Cu collisions including simple analysis of physics observables such as particle momentum and rate of energy loss. The level 3 trigger system includes an online display so that individual events can be visually inspected in real time. Figure 2.7 shows beam's eye view of a central event in the STAR Time Projection Chamber (TPC). The events in figure 2.7 was drawn by the STAR level 3 online display. The fast detectors that provide input to the trigger system are a central trigger barrel (CTB) and Zero Degree Calorimeters (ZDC).

2.6 Collision Centrality Selection in STAR

In relativistic heavy-ion collisions experiments one of the challenges is to measure the impact parameter of the two colliding nuclei. Because the impact parameter for each collision is never the same rather it varies from zero to sum of the radii of the colliding nuclei. In real experiment it is not feasible to measure the impact parameter of the

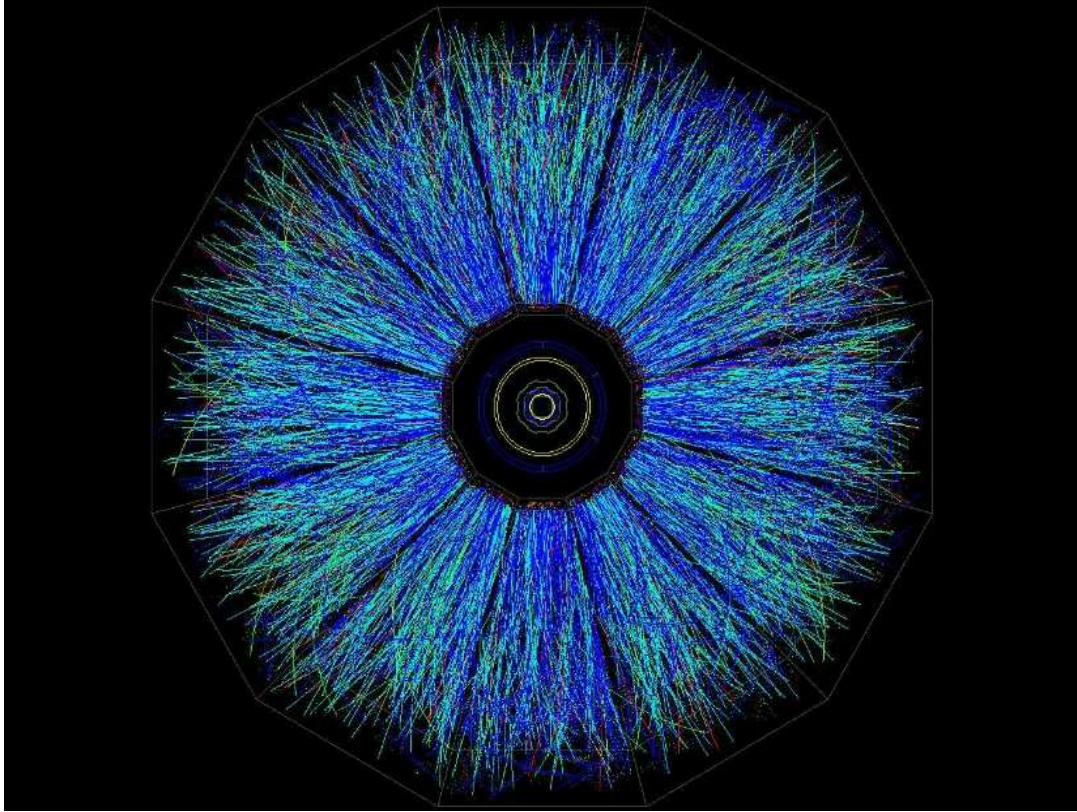


Figure 2.7: Beam's eye view of a central event in the STAR Time Projection Chamber (TPC). This event was drawn by the STAR level 3 online display.

colliding nuclei. So in heavy-ion collisions experiment we use the term centrality to define the impact parameter of the colliding nuclei. In general centrality is defined as the overlap region of the two colliding nuclei or classifying the events according to the number of participants. The central collision means that the two nuclei have suffered head-on collision and the overlap volume is maximum. On the other hand if the number of participants in the overlap region of two colliding nuclei is very less it is termed as peripheral collision. With the increase of the centrality of a collision, the size of the fireball produced by the collision, the energy density, the total transverse energy and the total multiplicity of that events increases. Therefore by knowing the centrality of the collision we can study the centrality dependence behaviour of the different global observables.

In STAR experiment the centrality of the collision is determined by counting the total charge particles event-by-event in the Time Projection Chamber (TPC) within the $|\eta| < 0.5$ coverage. Figure 2.8 shows the minimum bias distribution of the charge particles over a large number of events recorded by Time Projection Chamber (TPC) in Cu+Cu interactions at $\sqrt{S_{NN}} = 62.4$ and 200 GeV. The arrows show the number of charged particles used for defining each centrality class. The total % of events used with the minimum bias trigger condition for the present analysis of the real data and centrality determination for Cu+Cu collisions at $\sqrt{S_{NN}} = 62.4$ and 200 GeV was $\sim 60\%$. This number was not 100% because of the triggering inefficiency and vertex determination inefficiency in the low multiplicity events.

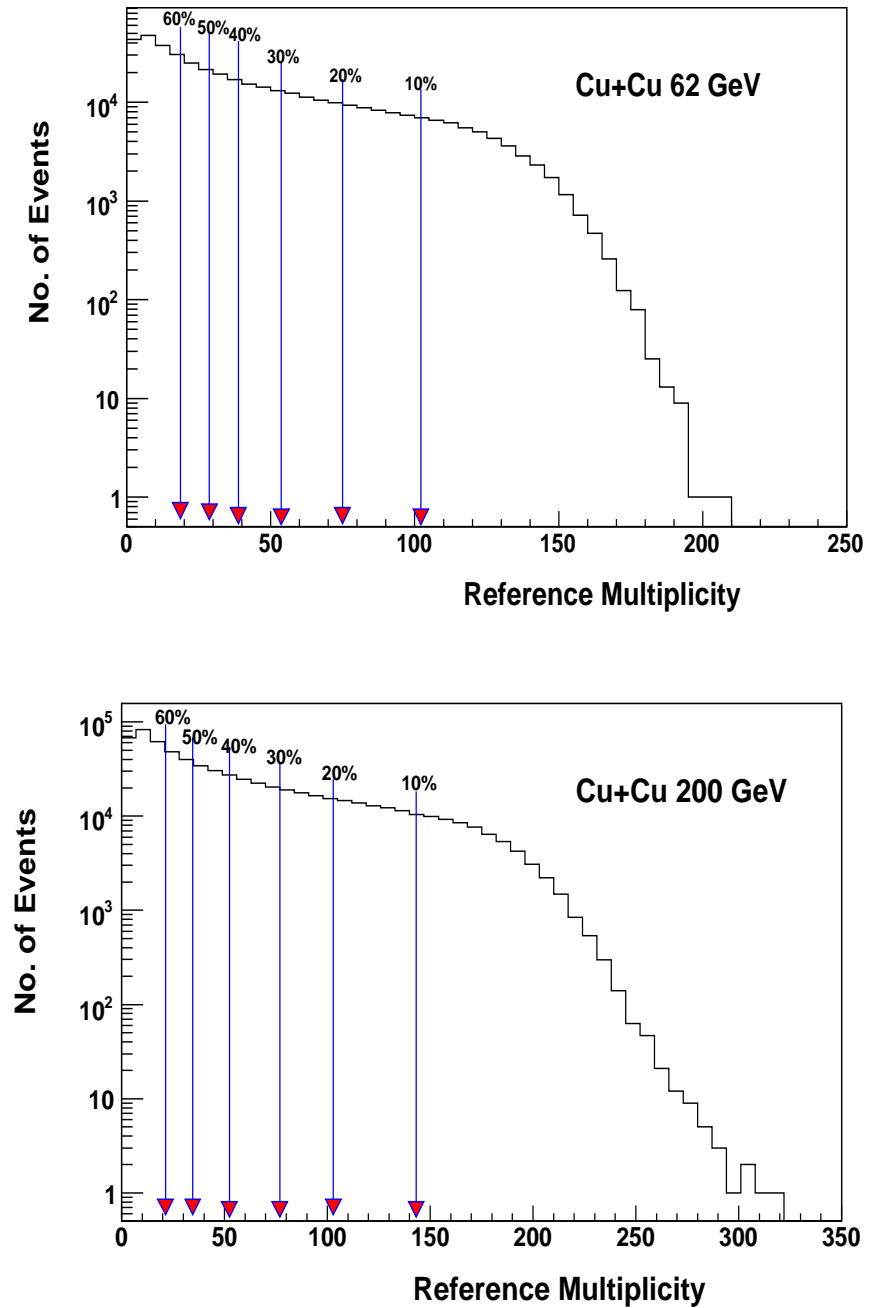


Figure 2.8: The minimum-bias distribution of the charge particles for Cu+Cu collisions at $\sqrt{S_{NN}} = 62.4$ and 200 GeV. The arrows represent the various centrality classes.

Bibliography

- [1] P. F. Kolb and U. Heinz, in Quark Gluon Plasma 3, eds. R.C. Hwa and X.N. Wang (World Scientific, Singapore, 2003); nucl-th/0305084.
- [2] M. Gyulassy, I. Vitev, X.N. Wang and B.W. Zhang, in Quark Gluon Plasma 3, eds. R.C. Hwa and X.N. Wang (World Scientific, Singapore, 2003), nucl-th/0302077; R. Baier, D. Schi, B.G. Zakharov, Ann. Rev. Nucl. Part. Sci. 50 (2000) 37.
- [3] STAR Collaboration (K.H. Ackermann et al.) Nucl.Instrum.Meth. A499, 624(2003).
- [4] K. Adcox et al., Nucl. Instr. Meth. A 499, (2003) 469.
- [5] M. Adameczyk et al., Nucl. Instr. Meth. A 499, (2003) 437.
- [6] "<http://www.bnl.gov/RHIC>", "<http://www.bnl.gov/rhic/experiments.htm>", Introduction about RHIC.
- [7] B. B. Back et al., Nucl. Inst. Meth. A 499, 603 (2003) 603.
- [8] B. B. Back et al., Phys. Rev. C 65 (2002) 061901R.
- [9] B. B. Back et al., Phys. Rev. Lett. 91 (2003) 052303.
- [10] B. B. Back et al., Phys. Rev. C 70 (2004) 021902R.
- [11] PHENIX Collaboration, K. Adcox et al., Phys. Rev. Lett. 86 (2001) 3500.
- [12] K. H. Ackermann et al., Nucl. Instr. Meth. A 499, (2003) 624.

- [13] 'Conceptual Design Report for the Solenoidal Tracker At RHIC', The STAR Collaboration, PUB-5347 (1992); J. W. Harris et.al., Nucl. Phys. A 566, 277c (1994).
- [14] R. L. Brown et.al., Proc. 1997 IEEE Particle Accelerator Conf., 3230 (1998) and F. Bergsma et.al., Nucl.Instrum.Meth.A 499, 633-639 (2003).
- [15] J.W.Harris, C.Beckmann, J. Gans and K.H. Gulbrandsen, RHIC physics overview, AIP Conference Proceedings Vol. 631, 533 (2002).
- [16] F. Bergsma et al., Nucl. Instr. Meth. Phys. Res. A 499 (2003) 633.
- [17] The STAR Collaboration, The STAR Conceptual Design Report, June 15, 1992 LBL-PUB-5347.
- [18] The STAR Collaboration, STAR Project CDR Update, Jan.1993 LBL-PUB-5347 Rev.
- [19] <http://www.star.bnl.gov> and references therein. See especially www.star.bnl.gov → Group Documents → TPC → Hardware.
- [20] L. Kotchenda et al., Nucl. Instrum. Meth. A 499, (2003) 703.
- [21] M. Anderson et.al., Nucl.Instrum.Meth.A 499, 659-678 (2003).
- [22] H. Bichsel, "Energy loss in thin layer of argon", STAR note 418.
- [23] H. Zhang, Ph.D. thesis, Yale University, 2003.
- [24] R. Bellweid et al., Nucl. Instr. Meth. Phys. Res. A 499 (2003) 640.
- [25] E. Gatti and P. Rehak, Nucl. Instr. Meth. Phys. Res. A 225 (1984) 608.
- [26] W. Chen et al., IEEE Trans. Nucl. Sci. 41 (1994) 941.
- [27] K.H. Ackermann et al., Nucl. Instr. Meth. Phys. Res. A 499 (2003) 713.

- [28] K.H. Ackermann et al., "The Forward Time Projection Chambers in STAR", Nucl. Instrum. Meth. A 499, 713 (2003).
- [29] S. Klein et al., Front-End Electronics for the STAR TPC, IEEE Trans. Nucl. Sci. 43 (1996) 1768.
- [30] STAR, "Proposal for a silicon strip detector for STAR", STAR note SN-0400.
- [31] L. Arnord et.al. Nucl.Instrum.Meth.A 499, 652-658 (2003).
- [32] "<http://star.in2p3.fr/STAR/technique2.html>", STAR SSD-Technical Info, General Overview.
- [33] C. Adler et al., "The RHIC Zero Degree Calorimeters", Nucl. Instrum. Meth.A 470, 488 (2001).
- [34] M. Beddo et al., Nucl. Instrum. Meth. A 499, (2003) 725.
- [35] M.M. Aggarwal et al., Nucl. Instr. Meth. Phys. Res. A 499,751 (2003); Nucl. Instr. Meth. A 488, 131 (2002).
- [36] Photon Multiplicity Detector for STAR: technical proposal, VECC Internal report VECC/EQC/00-04, May 2000 (revised: January 2001).
- [37] STAR FTPC Proposal, MPI-PhE/98-3 (1998).
- [38] A. Ljubicic et al., IEEE Trans. Nucl. Sci. 47, 99(2000) and J.M.Landgraf et al., 'An Overview of the STAR DAQ System', (this volume).
- [39] F.S. Beiser et al., 'The STAR Trigger', (this volume).
- [40] J.S. Lange et al. IEEE Trans. Nucl. Sci. 48, 3 (2000) and C. Adler et al., 'The STAR Level-3 Trigger System', (this volume).
- [41] H. Zhang, Ph.D. thesis, Yale University, 2003.

Chapter 3

Photon Multiplicity Detector (PMD)

3.1 Introduction

A Photon Multiplicity Detector (PMD) is designed, fabricated and installed as part of STAR collaboration at Brookhaven National Laboratory (BNL), USA by Indian groups from Variable Energy Cyclotron Centre, Kolkata, Institute of Physics, Bhubaneswar, Indian Institute of Mumbai, University of Jammu, Jammu, Panjab University, Chandigarh and Rajasthan University, Jaipur [1, 2, 3]. PMD is designed to measure photon multiplicity in the forward rapidity ($2.3 \leq \eta \leq 3.8$) region where high particle density precludes the use of a calorimeter. It is believed that photons produced at ultra-relativistic heavy-ion collisions form an important signal of the possible formation of Quark-Gluon Plasma (QGP) [4]. The figure 3.1 shows schematically view of Photon Multiplicity Detector (PMD) in STAR setup relative to central detector TPC experiment. It consists of two plane one is charge particle veto (CPV) and second is preshower plane. Both the planes are separated by a lead (Pb) plate of 3 radiation length thickness, used as photon converter and a stainless steel support structure in the form of a 5 mm thick

plate. The sensitive medium is a gas mixture of Ar and CO_2 in the ratio of 70:30 by weight. There are 41472 cells in each plane, which are placed inside 12 high-voltage insulated and gastight chambers called supermodules.

The PMD detector has been placed in the forward rapidity ($2.3 \leq \eta \leq 3.8$) region, at a distance of 540 cm from the center of the Time Projection Chamber (the normal collision point) along the beam axis. After successful completion of data taking by the PMD in WA93, WA98 [5, 6] and in STAR [1, 2, 3] experiment, Indian group also in the process to installed PMD in the ALICE (A Large Ion Collider Experiment) experiment [7, 8] at the Large Hadron Collider (LHC), CERN, Geneva and is expected to start taking data by the end of 2008.

3.2 Physics Goals of STAR PMD

By using the measurement of multiplicity and spatial distribution of photons at Relativistic Heavy-Ion Collider (RHIC) energies on event by event basis, the Photon Multiplicity Detector (PMD) will be capable to address the following broad topics in physics: (a) determination of reaction plane and the probes of thermalization via studies of azimuthal anisotropy and flow, (b) critical phenomena near the phase boundary leading to fluctuations in global observables like multiplicity, pseudorapidity distributions and density fluctuations such as droplet formation and hot spots can be studied by the power spectrum method [9, 10, 11], and (c) signals of chiral symmetry restoration e.g. Disoriented Chiral Condensates (DCC) [12, 13, 14] through the measurement of charged particle multiplicity (N_{ch}) in a common part of phase space and study of the observables N_γ and N_γ/N_{ch} with full azimuthal coverage. The primary signature of DCC is a large event-by-event fluctuation in photon to charged particle multiplicity.

Number of Plane	Two: Veto + Pre Shower
Pseudorapidity (η) Coverage	2.3 to 3.8
Azimuthal (ϕ) Coverage	2π
Area of the Detector	4.2 m^2
Weight of the Detector	900 kg
Gas used in the Detector	70% <i>Ar</i> + 30% <i>CO</i> ₂
Distance from Vertex point	540 cm
Total Number of Cells	82,944
Cell Cross-section	1.0 cm^2
Cell depth	0.8 cm
Total Supermodules	24
Data Readout System	GASSIPLEX + C-RAMS
Total Electronics Chains	48

Table 3.1: **Basic parameters of STAR Photon Multiplicity Detector.**

3.3 Working Principle of PMD

The Photon Multiplicity Detector (PMD) is based on a proportional counter using *Ar* + *CO*₂ in 70:30 ratio gas mixture as the sensitive medium. This gas mixture is preferred because of its insensitivity to neutrons. The basic principle of the measurement of photon multiplicity in PMD is similar to those of preshower detectors used in the earlier experiment like WA93 and WA98 experiments at CERN SPS energies [5, 6]. The principle of a photon detection in PMD is schematically depicted in figure 3.2. It consists of highly segmented detector placed behind a lead converter of suitable thick-

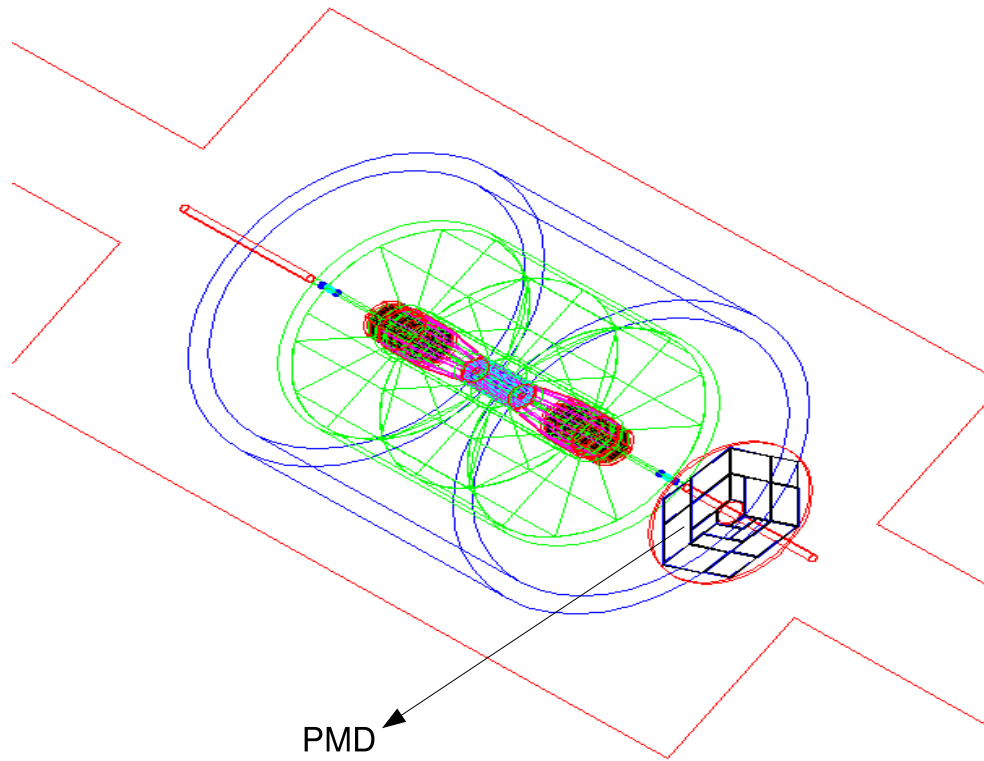


Figure 3.1: Schematic view and Position of Photon Multiplicity Detector in STAR relative to central detector TPC. The PMD is located at 540 cm from vertex and kept outside the STAR magnet.

ness. When photons passing through a converter initiate an electromagnetic shower and produce large signals on several cells of the sensitive volume of the detector. Charged hadrons normally affect only one cell and produce a signal representing minimum ionizing particles (MIP). The thickness of the converter is optimized such that the conversion probability of photons is high and the transverse shower spread is small to minimize the shower overlap in a high multiplicity environment.

The two planes (preshower + charge particle veto) of PMD are so arranged that there is an exact one-to-one correspondance between individual hexagonal detectors in each plane. According to PMD principle, when a photon passes through the converter, it produces signals in more than one cell. On the contrary, charged hadrons deposit very little energy producing signals in just about one cell. This is because of their low interaction cross-section with the converter. The signals produced by charged particles are similar to those given by minimum ionizing particles (MIP). Secondly, charged particles produce signals in about one cell in both CPV as well as the preshower planes. On the contrary photons produce signals in a larger cluster of cells in the preshower plane. These characteristics are used for discriminating between photons and charged particles by using proper energy threshold cut.

3.4 Designing and construction of PMD

At Relativistic Heavy-Ion Collider energies the particle density is very high. So In order to handle the high particle density environment in the forward rapidity region, the detector technology has been chosen with the following considerations that (i) multihit probability should be less, (ii) minimum ionizing particles should be contained in one cell, and (iii) low-energy δ -electrons should be prevented from travelling to nearby cells

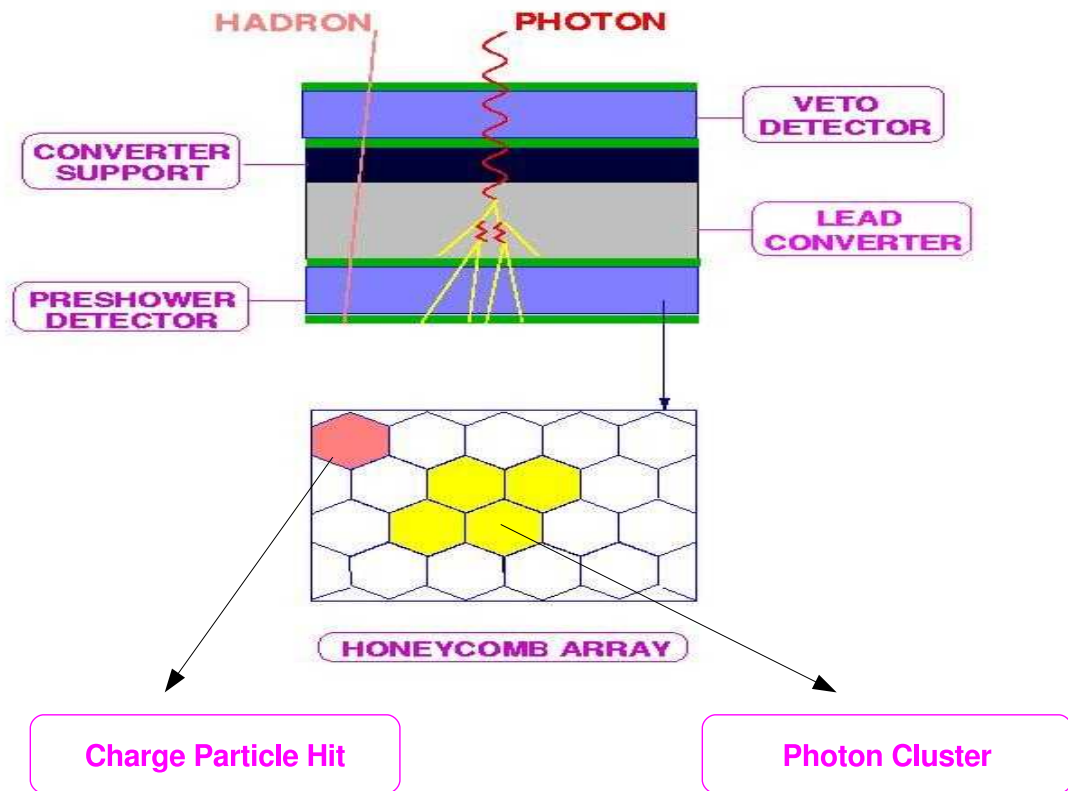


Figure 3.2: The working principle of Photon Multiplicity Detector.

and causing cross-talk among adjacent cells.

Requirement of granularity and isolation of cells require the segmentation of the detector gas volume with material effective for reducing δ -electrons from crossing one cell to other. We have used honeycomb cellular geometry with wire readout. The copper honeycomb body forms the common cathode and is kept at a large negative potential. It also supports the printed circuit boards (PCBs) which are used for signal collection and for extension of the cathode required for proper field shaping [8, 1].

3.4.1 Detector and its components

The preshower plane of Photon Multiplicity Detector (PMD) consists of an array of hexagonal cells. A unit cell is shown schematically in figure 3.3 (a) along with a longitudinal section illustrating the use of extended cathode for field shaping. This design was selected after several simulation studies and prototype tests and ensures uniform charged particle detection efficiency throughout the detector cell [15].

A honeycomb of 24×24 cells forms a unit module. This is a rhombus of side approximately 254 mm having identical boundaries on all the four sides. Cell walls at the boundary are kept half as thick as those inside so that adjacent unit modules join seamlessly. A set of unit modules are enclosed in a gas-tight chamber called supermodules. In one supermodule the number of unit modules varies from 4 to 9. The Photon Multiplicity Detector (PMD) in STAR experiment composed total of 24 supermodules (twelve in each plane) arranged in the form of a hexagon as shown in figure 3.3 (b). This geometry ensures full azimuthal coverage with minimum number of supermodules.

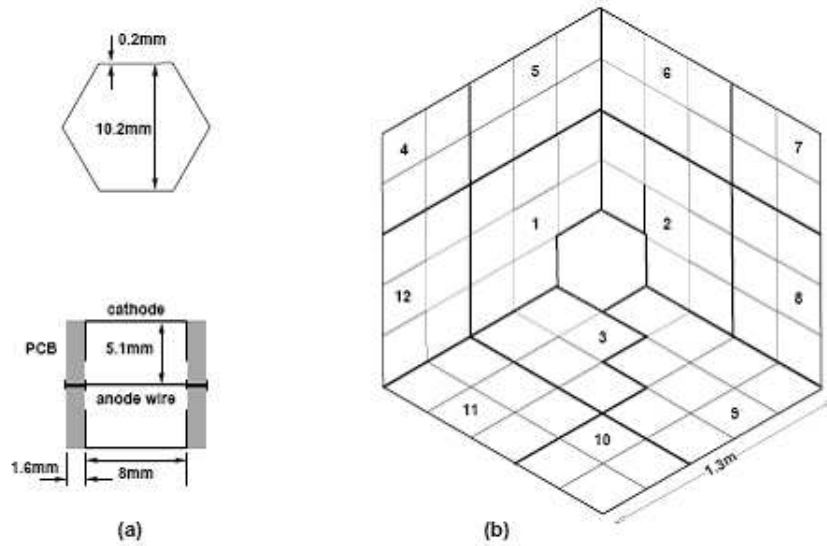


Figure 3.3: (a) Unit cell schematic with cross-section showing the dimensions and the cathode extension, (b) Layout of the STAR PMD. Thick lines indicate supermodule boundaries. There are 12 supermodules each in the preshower plane and the veto plane. Divisions within a supermodule denote unit modules.

The components of a unit module are shown in the figure 3.4. It consists of a custom-built copper honeycomb sandwiched between two PCBs which hold the anode wire and provide extension to cathode. The top PCB, containing the electronics boards, has solder-islands at the centre of each cell with a 0.5 mm diameter gold-plated through hole. Signal tracks from cluster of 64 cells are brought to a 70-pin connector. The PCBs on the bottom side have only soldering islands without signal tracks, serving as anchor points. The inner part of the PCBs are gold-plated, with circular islands near the anode wire and form part of the extended cathode.

A copper unit cell is the building block of the honeycomb. It is fabricated using 0.2 mm thick ETP grade copper sheets which are solder coated on one side. The sheet is cut to precise dimensions along with notches and bent in hexagonal form with precision dies. These are arranged in a 24×24 matrix in a high precision jig of rhombus shape. Hexagonal stainless steel inserts, having dimensions matching the inner dimensions of the cell, are inserted in each cell. The assembly is heated so that soldered surfaces join to form a rigid honeycomb.

The honeycomb, after cleaning, is dip-coated with high conductivity graphite paint having thickness of $\sim 10 \mu\text{m}$. The unit honeycomb module has stiff 1 mm diameter brass screws situated at 24 different locations, which act as guides for attaching the PCBs on both sides, ensuring proper alignment. They are also used to bring out the high voltage connections of the cathode onto the PCBs. The two PCBs are attached on both sides of the honeycomb, aligning with the screws. These screws protrude only 0.5 mm above the PCBs surface and are fixed with thin nuts on the surrounding islands. The islands are covered with plastic caps.

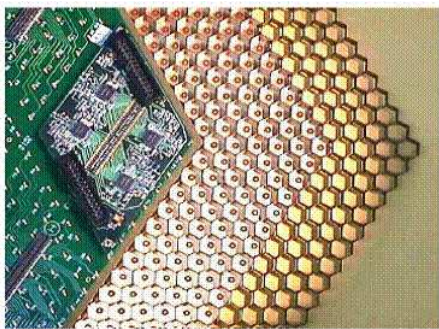


Figure 3.4: **Components of a unit module: Copper honeycomb, placed between two PCBs. The top PCB is seen with connectors and a FEE board. The cathode extension on the inside of the bottom PCB and the island separating the anode wire with the cathode is visible through the honeycomb. The photograph was taken with unassembled components.**

The gold-plated tungsten wires ($20\ \mu\text{m}$ diameter) are inserted through the holes on the PCBs, using a needle and a tensioning jig. After applying tension of $\sim 30\%$ of the elastic limit, the wires are soldered onto the islands on the PCBs about 3 mm away from the hole [8]. The plated through-holes, where wires emerge, are then closed with a tiny amount of fast-setting epoxy to make them gas-tight. This scheme prevents creepage of solder flux into the cell and makes soldering easier. A moulded FR4 edge frame is bonded to the top PCB. This frame has a beveled outer wall which forms a V-shaped groove between the boundaries of the adjoining unit modules.

Quality assessment for the fabrication of the unit module is done by several ways, viz, visual inspection of the solder joints and epoxy filling in the holes and measurement of resistance of each wire to monitor dry-soldering contacts. Resistance measurement shows that the RMS is within 5% for one unit module. In addition, high voltage tests

are also performed after connecting the front-end electronics boards and the pedestals of chips monitored to test stable operation of the detector. As mentioned above PMD composed 24 supermodules and the number of unit module in each supermodules is different. The number of unit module in supermodule depend upon the position of supermodule and detector readout.

A schematic cross-section of a supermodule is shown in figure 3.5. Supermodule is a gas-tight chamber made of 3 mm thick FR4 grade glass epoxy sheet as the base plate and a 7 mm thick and 25 mm high aluminum boundary wall. The opposite sides of the boundary walls have gas-feed channels. Each channel has 24 openings into the chamber. This scheme, along with the notches in the cells, keep the gas flow impedance low. A set of assembled unit modules are placed to fill the inner area of the supermodule enclosure, leaving a gap of 1 mm on all sides to accomodate general assembly tolerance and to provide insulation between the honeycomb cathode and the boundary. Teflon spacers are inserted into this gap all along the boundary to arrest any movement of the unit modules and also to insulate the honeycomb cathode from the walls. The groove formed at the junctions of all the unit modules and between the boundary walls and the unit modules are filled with high viscosity silicone adhesive compound to make the chamber gas-tight.

Gas is fed through the connector at the end of the long gas feed channel. It enters through all the entry points in the channel simultaneously, at the depth of 4 mm from the bottom of the chamber. It then flows through the notches and exits at the other edge of the supermodule through the 24 openings of the output channel. An aluminum enclosure containing one SHV connector, an High Volatge (HV) limiting resistor and decoupling capacitor is now fixed at one corner of the supermodule very close to the HV

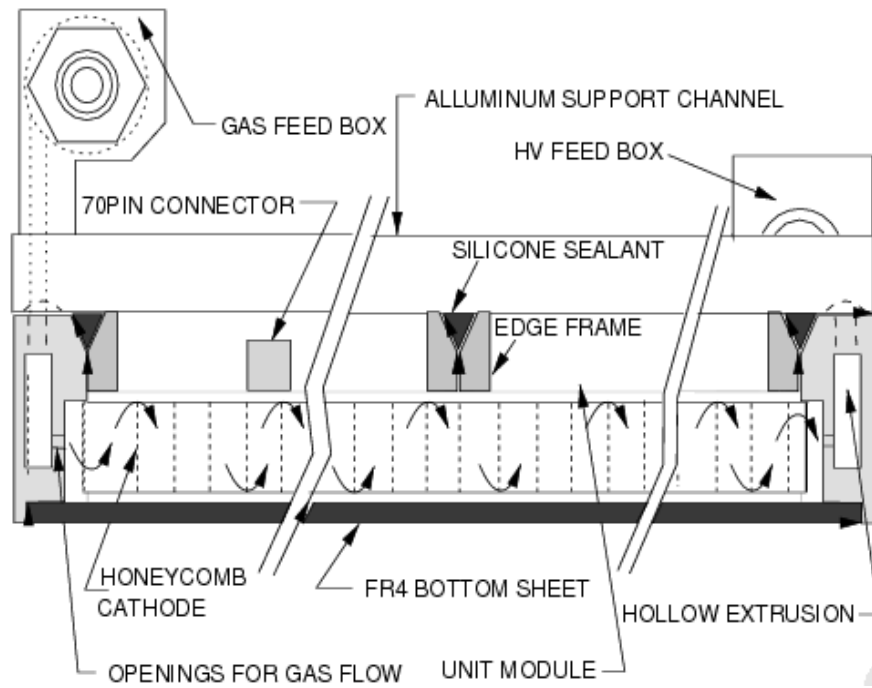


Figure 3.5: Schematic cross-section of a supermodule showing the boundary walls, gas flow channels, high voltage connection and gas-tight sealings.

tapping point.

3.4.2 Support Structure of PMD

The schematic drawing of the support structure for Photon Multiplicity Detector (PMD) in STAR experiment is shown in the figure 3.6. Mainly it consists of two parts: (a) the support plates and (b) the suspension movement mechanisms. A 5 mm thick flat stainless steel plate is used to support the lead converter plates and supermodules in each half of the PMD. It has tapped holes for screws corresponding to hole positions in the lead plates and in the supermodules. The 15 mm thick lead converter plates are sandwiched between two layers of gas detectors. The two halves of the detector are supported on the girders and hang freely in a vertical position. The support structure allows both x and z movements of the detector. Each half of the detector can be separated for access by a smooth independent movement controlled by limit switches. The hanging elements have free swinging pivots, fine adjustments for horizontal motion, and plane position adjustments for alignment of the detector. The services of the two halves are also independent. When fully open, the two halves provide sufficient clearance for the poletip support of the STAR magnet to move in. The edges of the support plate are also used for mounting the gas feed manifolds, show boxes for low voltages supplies and general support for distribution of cables onto the detector.

3.4.3 PMD Electronics and Readout

To read signals recorded by PMD, Front-End electronics (FEE) based on the 16-channel GASSIPLEX chips developed at CERN [16] is used which provide analog multiplexed signals and readout using the custom built ADC board (C-RAMS) which were obtained

from CAEN, Italy. C-RAMS can handle a maximum of 2000 multiplexed signals. Considering the symmetry requirements of the detector hardware, the readout of the entire PMD has been divided into 48 chains. Each chain covers maximum three unit modules and has 1728 channels. Each readout chain is driven by: (i) a translator board, (ii) 27 FEE boards each consisting of four GASSIPLEX chips, and (iii) a buffer amplifier board.

The translator board converts NIM levels of all control signals into the level required for the operation of GASSIPLEX chips. The operating voltage for these chips is ± 2.75 V and hence all the NIM signals are to be translated to 0 to 2.75 V levels.

The cells in the unit modules are arranged in clusters consisting of 8×8 cells connected to a 70-pin connector. This cluster of 64 cells is read out by a Front-End electronics (FEE) having four GASSIPLEX chips. The schematic photograph of a Front-End electronics (FEE) with four GASSIPLEX chips are shown in the figure 3.7. For geometrical considerations the FEE board is also made in rhombus shape. When all the boards are placed on the detector, they almost fully cover the detector area. This arrangement helps to reduce the material and also provides a ground shield for the detector.

In order to reduce voltage drops over a long chain of 1728 channels, a bus-bar like design has been adopted to provide power to the FEE boards. To protect the input channels against high voltage spikes, a provision has been made on the board layout to connect a diode protection circuit. For the transmission of a train of analog multiplexed signals to the readout module via a low impedance cable a buffer amplifier is used.

Digitization using C-RAMS requires that all multiplexed pulses within a chain should have the same polarity. In order to read the full chain, the pedestals in the

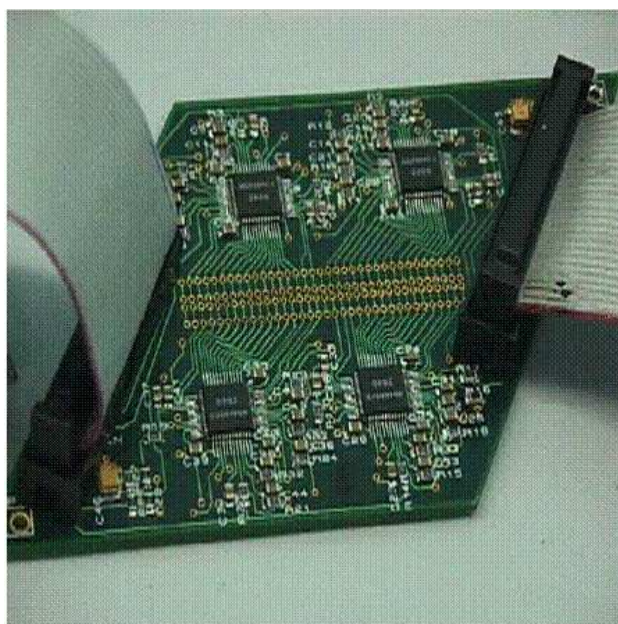


Figure 3.7: **Front-End Electronics (FEE) board with four GASSIPLEX chips.**

chain need to be adjusted to the minimum of the pedestals in the chain. This shifting of the pedestal effectively reduces the dynamic range. To minimize the reduction in dynamic range due to pedestal adjustment, we need to select the chips for a chain having minimum pedestals in very close range.

For proper quality control in the assembly of FEE boards, each GASSIPLEX chip has been tested for full functionality of each channel. In addition the pedestals of all the channels have been measured. The minimum pedestal as well as the spread in pedestal has been determined for each chip. Figure 3.8 shows (a) the distribution of pedestal minima and (b) scatter plot of pedestal minima vs. pedestal spread for 5000 chips. It is seen that we can select chips of four categories having close ranges of pedestal minima and pedestal spreads. The narrow width of the distribution shows that the usable number of chips is a large fraction of the total number of chips tested.

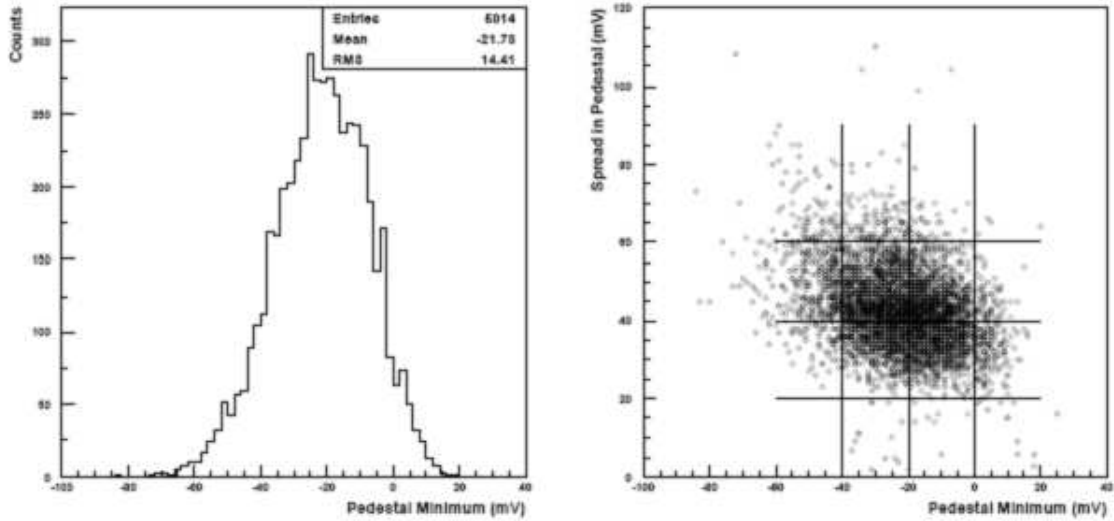


Figure 3.8: (a) Pedestal Minimum values (in mV) for 5000 chips and (b) pedestal minimum vs. pedestal spread for these chips. Lines are drawn to suggest the grouping of chips for a uniform chain.

3.4.4 Trigger and Data Acquisition

Photon Multiplicity Detector (PMD) gets a pretrigger after 500 *ns* of the RHIC collision. PMD requires a pretrigger because of the GASSIPLEX chips used in the FEE boards. These chips need a pick up time of 1.2 μ s. The pretrigger to PMD is issued from Zero Degree Calorimeter (ZDC). As soon as the ZDC gets any signal it sends a pretrigger to PMD and the charge accumulation in the GASSIPLEX chip of the PMD FEE starts. When L0 arrives the signals are read out of the FEE boards as a signal from good event and send to the main data stream for data acquisition system.

Now as per our electronics requirement we have implemented the following trigger

scheme. As soon as we get the pretrigger we send the BUSY signal and after 814 ns (after the RHIC collision) we send the Track/Hold signals (T/H) to the FEE. Now there are two conditions:

(i) L0 has not arrived within the pre-defined time. In this case we clear the signals T/H and BUSY. BUSY is cleared after 4.5 μ s, from its start, as the baseline recovery time of FEE is 4.5 μ s.

(ii) L0 arrived within its pre-defined time. We send signals T/H and BUSY and then check if for this L0 a corresponding pre-trigger exists. If this is true then, we send Trigger signal to Sequencer and in turn Sequencer generates the signals Clocks, T/H, CLR, BUSY, and CONV. The clock signals are then sent to FAN IN and FAN OUT modules and distributed to various chains. Similar distributions is done for T/H and CLR signals. The CONV has to pass through the delay module and feed to CRAMS. CRAMS will then digitize the analog signal and send the ready signal to Sequencer and the readout of this digitized signal starts. After the readout, the FEE clear signal is sent and also the software BUSY (VME_{BUSY}) is withdrawn. If there no pre-trigger corresponding to the L0, then we clear the BUSY.

3.5 PMD Gas System

In STAR PMD, a mixture of Ar and CO_2 in the 70:30 ratio at a pressure of 1 bar is used. With this mixture a good proportionality for charge particle detection was observed at applied voltages between 1400 to 1600 V. In view of this a two component gas-flow and control system has been designed. This gas flow control system, for the PMD, consists of a single pass design that distributes gas to all the super modules.

A schematic diagram of the PMD gas system in STAR experiment is shown in figure

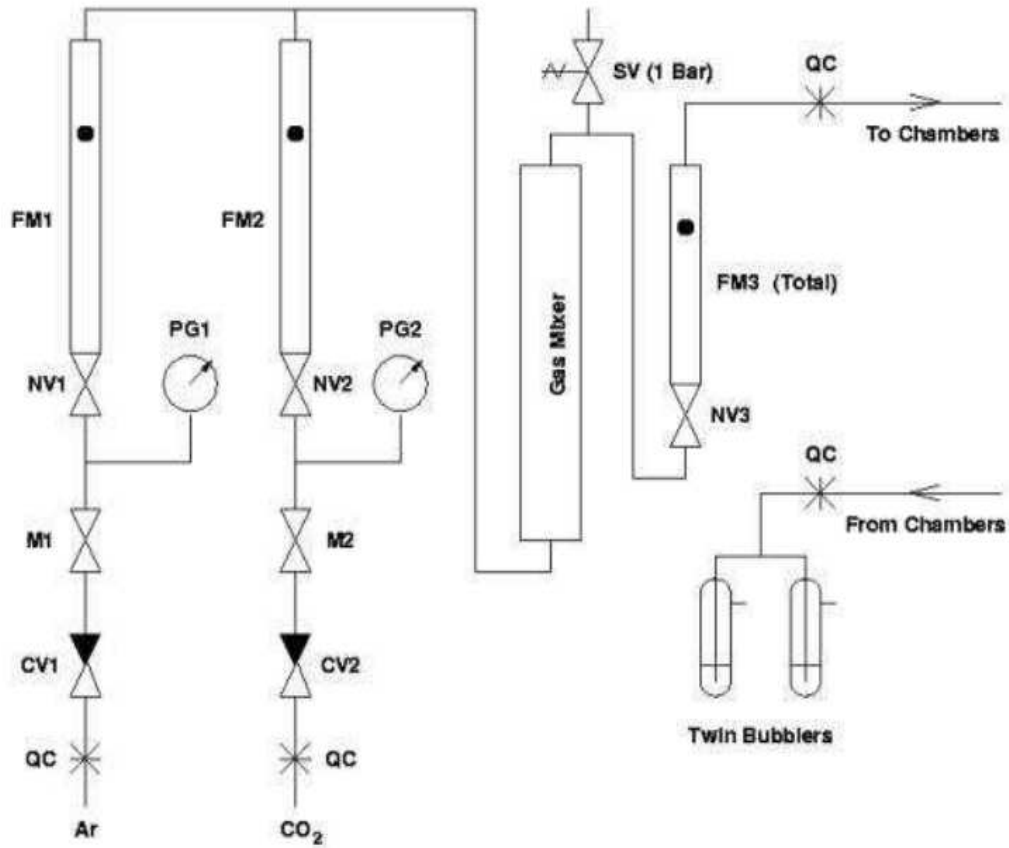


Figure 3.9: Schematic layout of Gas system for Photon Multiplicity Detector (PMD) in STAR experiment.

3.9. In the gas flow system, individual gas components argon and carbon dioxide enter the corresponding flow meters through the one way circle seal check valves (CV1,CV2) and manual control valves (M1,M2). Flow rates can be adjusted by the two needle valves (NV1, NV2) located on the bottom part of the flow meter. The gases enter the gas mixing tube and due to a concentric tube arrangement inside the mixer, their flow direction changes thrice for achieving the required mixing. In the case of excess pressure, above 1 bar, in order to protect the chambers, there is a safety valve at the exit of the mixing tube to vent out the excess gas. Flow meter FM3 indicates the total flow of mixed gases into the chambers. The normal flow rates used are about 30 litres/hour. The gas which returns from the chambers is vented out after passing through two bubblers.

3.6 Detector Performance

Before taking the final run various detailed tests was performed with STAR PMD prototype detector using pion beams in the range of 3 to 30 GeV at the CERN SPS for the study of the response of the minimum ionizing particle (MIP) and charged hadrons. For preshower applications, the performance of the detector characteristics were studied using electron beams with various converter (Pb) thickness. The gas mixtures, and operating bias voltage were the other two paramrters which were optimized using the data [2]. The GEANT simulation has been performed to study the effect of upstream material on the physics performance of the PMD. We presents and discuss here some of the results below.

3.6.1 Response to Charged Particles

Figure 3.10 (a) shows a typical pulse height spectrum, taken with a STAR PMD prototype, with 5 GeV pions, at an applied voltage of -1500 V. The spectrum has been fitted

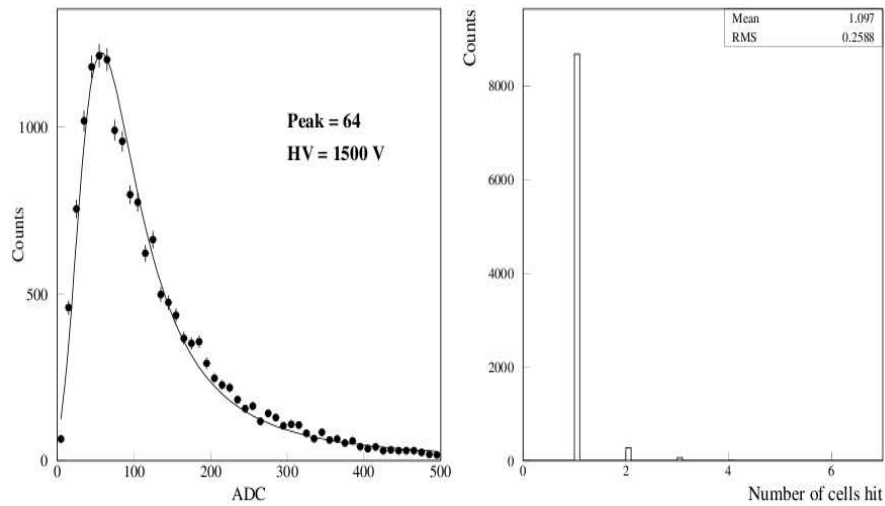


Figure 3.10: (a) Typical MIP spectra for cells with -1500 V, fitted with Landau distribution, (b) Distribution of the number of cells hit by MIP, it is seen that MIP is contained mostly in one cell.

with a Landau distribution characteristic of a MIP. Figure 3.10 (b) shows a distribution of the number of cells hit by a MIP. One can see the most of the signal is confined to one cell which satisfies one of the main design goals of the detector.

The efficiency for charged particles detection and cell to cell gain variation for the prototype has been determined for a number of cells chosen randomly in the prototype. The detection efficiency corresponds to the fraction of charged particles detected with respect to their incident number. The cell to cell gain variation or the so called relative gain is defined as the ratio of the mean pulse height in a cell to the value of the mean pulse height taken over a large number of cells. In figure 3.11 (top) shows the histogram of the relative gains for a total of 40 cells. The overall gain of the prototype chamber was found to be quite uniform, the distribution showing a narrow width with a $\sigma \sim 6\%$. In figure 3.11 (bottom) the efficiency measured over the same 40 cells is plotted. The

average value of the efficiency was found to be 90%. The efficiency was also found to be uniform over the cross-section of a single cell, varying within a narrow range of 93-99%, the lower value being at the edges of the cell.

3.6.2 Preshower Characteristics

Preshower behaviour is characterised by: (a) the transverse spread of the shower, which is given by the size of the cluster of hit cells, and (b) by the energy deposition expressed in terms of the cluster signal (i.e. the total signal in all the hit cells, in ADC units). These have been determined using 1-6 GeV electrons and a three radiation length ($3\times_0$) thick lead converter kept in front of the prototype detector. A typical preshower spread for 3 GeV electron is shown in left panel of figure 3.12. One can see a 3 GeV electron incident on the STAR PMD prototype produces clusters of all sizes ranging from one to about 12 hit cells. On the average a cluster of five cells are hit whose signals are to be added to get the value of energy deposited by the showering particle. Earlier simulations studies indicate that the cluster size obtained from the test data very closely resembles to that obtained from GEANT simulation thereby suggesting that the occupancy of the detector for a given multiplicity can be obtained reliably with GEANT simulation.

The energy deposition spectra for electrons at various energies as obtained from the test data and those obtained from the GEANT simulation at corresponding energies are shown in the right panel of figure 3.12. Even though the shapes look similar, the relative widths in the preshower spectra are larger in test data compared to those in simulation. This difference is due to the fluctuations in gas ionization, signal generation and transmission processes associated in data, which are not accounted for in simulation. It was therefore, necessary to estimate this and introduce the same in simulations regarding a

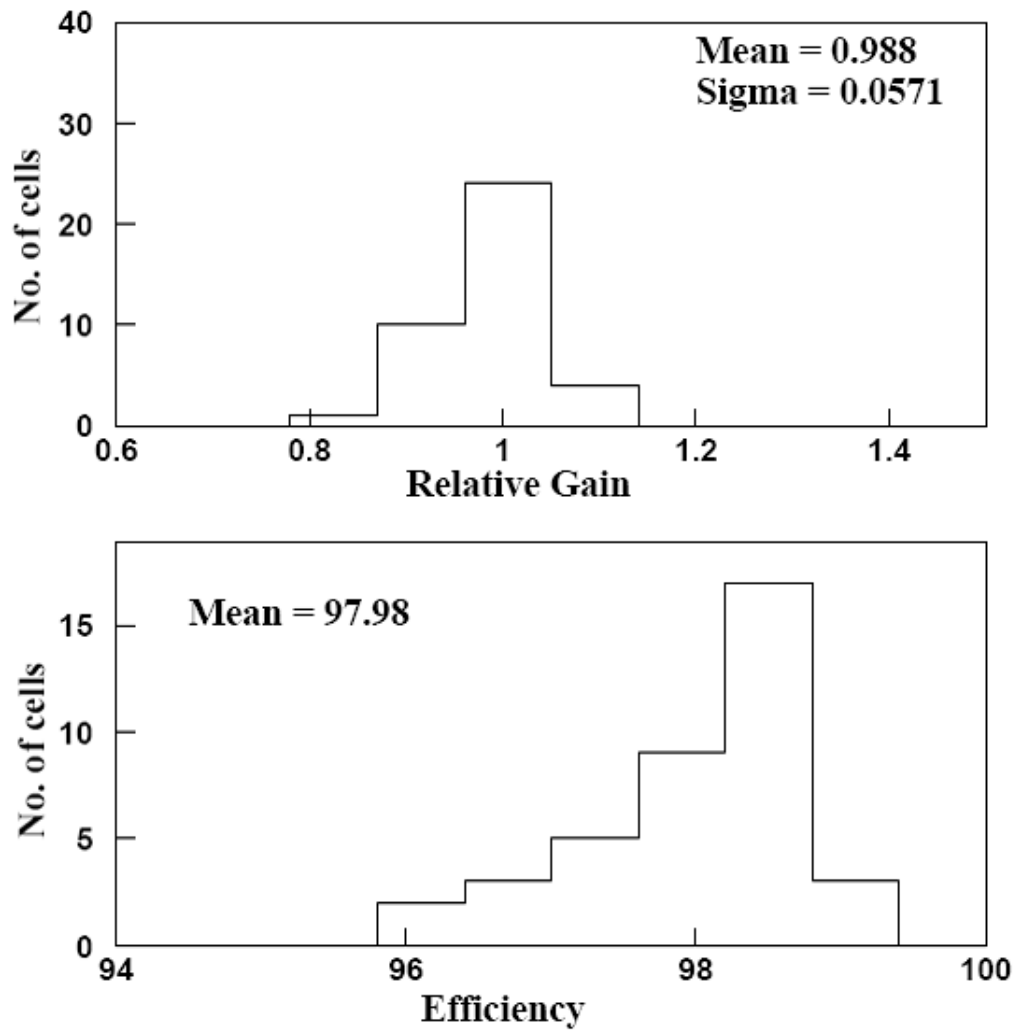


Figure 3.11: Distribution of gain (top) and efficiency (bottom) for randomly selected 40 cells from the prototype chamber.

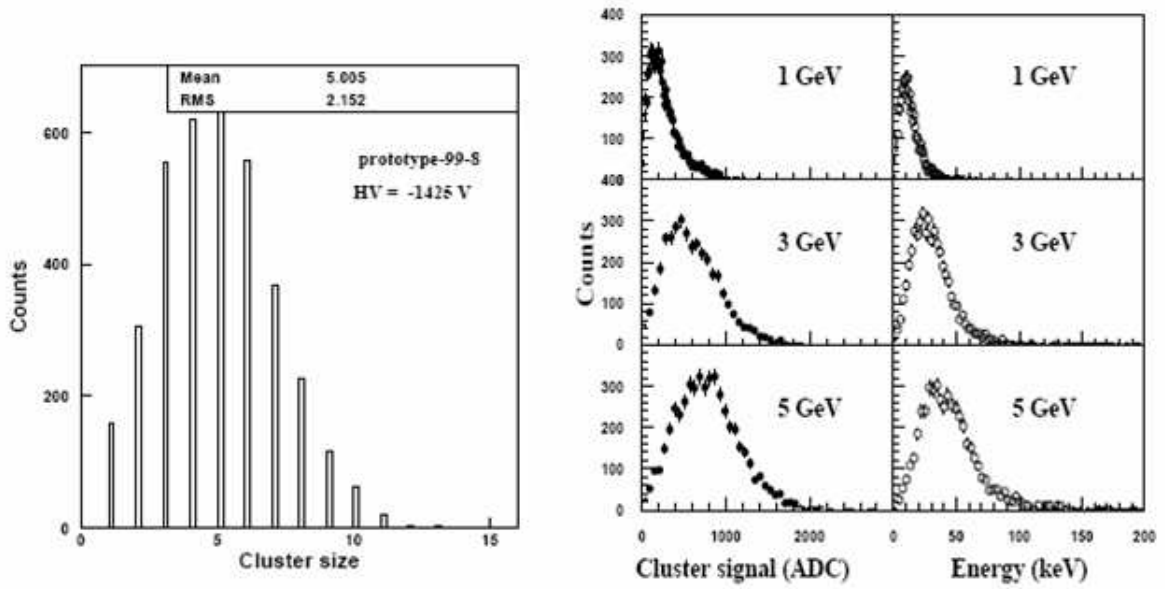


Figure 3.12: (left panel) Typical cluster size for preshower expressed in terms of the cells affected by electron, (right panel) filled circles represent energy deposition (in terms of cluster ADC) spectra for electrons with three energies, open circles represent the simulated energy deposition (in KeV) for electrons with corresponding energies. Width of simulated spectra is smaller compared to test data.

proper modeling of width of energy deposition. This extra width is called the readout width.

3.7 Photon Clustering

In order to find the energy deposited by a photon or a hadron one needs to add the signals obtained from the associated cluster of cells. The particle hit position can be

determined from the centroid of the cluster of cells hit. But to determine whether the particle was a photon or a charged hadron one needs to apply some kind of a discrimination on the obtained signal. One of the oldest methods [5, 17, 18] has been to apply a 3 MIP cut on the signal. Anything above this can be considered, with certain probability, as that due to a photon. Therefore, the first thing to do with the ADC signal is to employ some kind of a clustering and find out the total ADC contained. When multiplicity is very high then clusters start overlapping and it becomes difficult to employ a simple procedure. In such a case, one can construct superclusters consisting of a large number of cells. The reconstruction procedure involves two steps: (a) breaking of large clusters into smaller clusters each of which represents one incident particle and (b) remove the clusters formed by charged particles from the reconstructed clusters using some energy threshold.

The first step involves arranging the energy deposited in each cell in descending order. The super clusters are then formed beginning at the cell having largest energy deposition and collecting all cells contiguous to it. This process is repeated with decreasing order of energy deposition till all the cells are exhausted. This completes the formation of superclusters. Each supercluster is then examined to determine whether it can be broken up into smaller clusters. If the cluster consists of one cell, the center of the cluster is identified with the center of the cell and the strength of the cluster is identified with the energy deposition of the cell. For two cell clusters, the center of the cluster is defined to be the sum of the energy deposited in the two cells. If the supercluster has more than two cells, then one has to break the large clusters into smaller clusters. The centres of the clusters are expected to be near the cells corresponding to the peaks in energy deposition. The justification for the above procedure is as follows:

A weak peak close to a strong peak may not be considered as a separate cluster. Because

we expect that there would be nonzero energy deposition in cells neighboring the peaks. If the peak is strong the neighboring cells will have relatively large energy deposition. Unless another peak close to the strong peak is strong enough, one may consider it to be associated with the strong peak.

There will be fluctuations in the actual energy deposition. These fluctuations may produce fictitious peaks, particularly for cells close to the cell having large energy deposition. In order to accommodate these points, the peaks neighboring a peak having a large energy deposition are not considered as independent cluster centres if the corresponding peak strengths are below a certain fraction of that for the strong peak. The condition adopted at the moment is that the second next nearest neighbour (which is at a distance of $\sqrt{3}$ cell units) must have energy deposition greater than 25% to be considered as a separate centre in addition the third next nearest (which is at a distance of 2 cell units) must have an energy deposition greater than 10% of the main peak energy deposition value.

Having determined the possible cluster centres, a minimization procedure is used to optimize the position and strength of the cluster. For this, we assume that each cluster has a Gaussian shape. The centres, heights and widths of these Gaussians are then varied for optimization. The output from the above clustering procedure are x,y, position, η , ϕ , of the clusters, number of cells in each cluster and the energy deposition (ADC) of the clusters. Then one has to separate the charged particle clusters and identify the photon like clusters using different procedure. One of the procedures is based on the fact that photon clusters are expected to deposit larger amount of energy compared to hadron clusters. So, one can tag the clusters having energy greater than some predetermined threshold energy value as photon clusters and others as non-photon clusters.

In the present case, we use 3 MIP signal as the energy cut off for photon like clusters. However, it is possible that some of the hadrons would deposit enough energy to be misidentified as photons. Their fraction and the photon detection efficiency and purity for the PMD is estimated from simulations.

3.8 STAR Simulation

From the test beam studies, details about the detector response to both hadrons and photons are investigated. The various steps used in generating the simulated data, regarding a photon or charge particle hit, from an event generator (or from single particle input) along with a GEANT simulation are shown in the flow chart in figure 3.13. In STAR simulation framework, this flow chart includes both the GEANT simulation for STAR (GSTAR) and the chain used for reconstruction, which is the Big Full Chain (BFC). For the present study, with Cu+Cu interactions at $\sqrt{S_{NN}} = 62.4$ and 200 GeV, events from HIJING event generator have been used.

GSTAR is a simulation framework designed for the STAR detector using the GEANT simulation package Geant3.21. The GSTAR package consists of a set of .g modules, each providing the description of the geometry for different subsystems of the STAR detector, like: beam pipe, TPC, SVT, FTPC, PMD etc. Also it performs particle generation with on-flight analysis. The PMD geometry has been implemented in the GSTAR framework considering each plane (preshower and veto) of the PMD to be consisting of 17 super-modules (SMs). In order to simplify the implementation of SMs of different sizes, there are more number of SMs in GEANT compared to their actual number (12). Figure 3.14 shows the layout of the PMD in GSTAR framework.

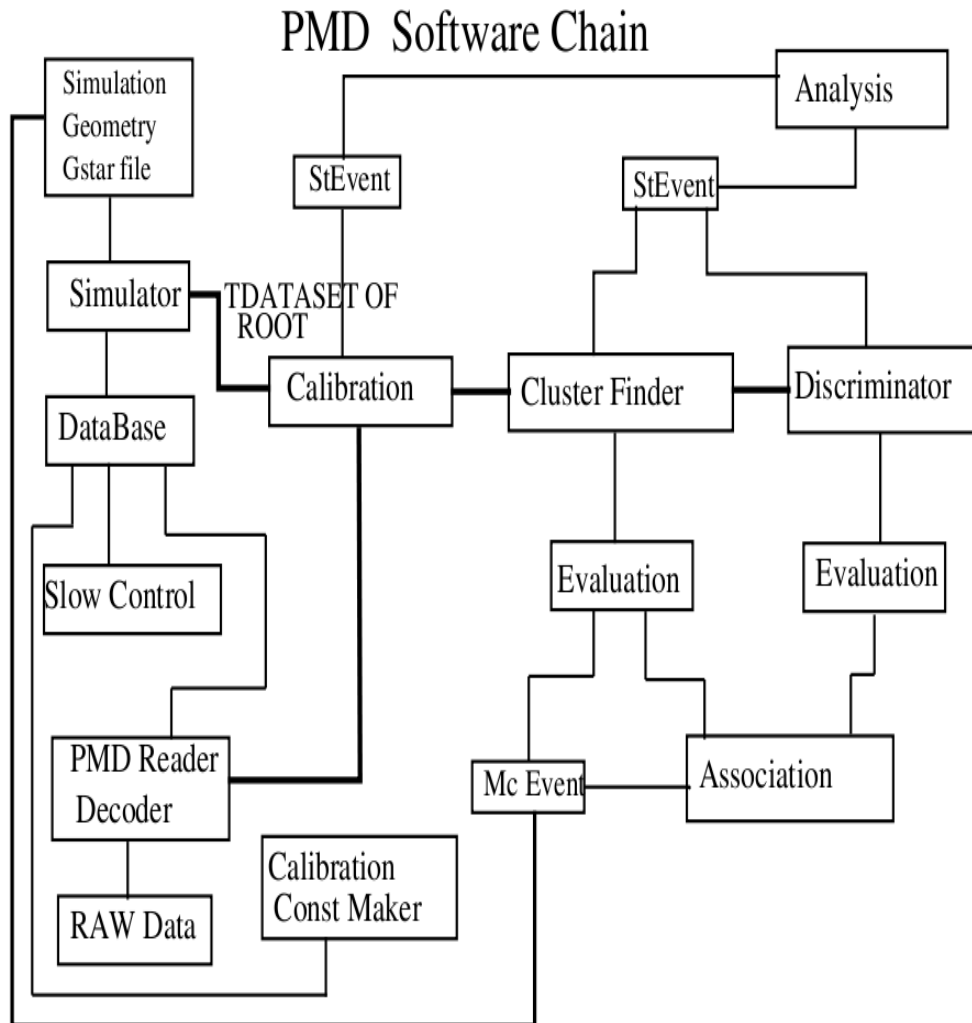


Figure 3.13: Flow chart showing the steps in generating simulated events.

In GSTAR framework the PMD is implemented in the following manner. First we divide the PMD volume into three sectors. Sector 1 and 2 are divided into 5 volumes with sector 3 divided into 7 volumes which are of same size as the SMs. Each volume has been placed independently inside the sector. Then, we place an aluminium frame inside each volume which corresponds to the outer frames of the SMs. In the next step, for each SM, a PCB board (G10 material, density 1.7) which corresponds both the FEE plane and the first layer of PCB on the chamber. The next layer of material corresponds to the active volume made out of gas filled honeycomb array of detectors. The implementation of the honeycomb array is done as follows. The material volume available inside the SM is broken up into rows of strips in air which are then filled with hexagonal cells of Cu with inner and outer radii 0.53 cm and 0.55 cm respectively. The volume is then filled with a mixture of Ar and CO_2 in the ratio 70:30. Having formed gas filled array of cells, we now place another layer of PCB material of thickness (density 1.7) to simulate the back plane of the chamber. This is done for all the 17 SMs in the CPV plane. Having constructed the CPV plane, we now include a Pb plane of thickness 15 mm on top of which we place an support structure plane of thickness 5 mm. Several processes have been implemented for different SMs e.g. applying calibration constants to outputs of each SMs, finding clusters from the hits over the SMs and associating hits/clusters from the SMs to reconstruct particle tracks etc. The STAR reconstruction process includes all the above processes in the proper ordering in the BFC. Each process is designated as a derived class (or maker) from an abstract base class.

The physics performance of the Photon Multiplicity Detector (PMD) is characterized in terms of following two quantities, (i) photon counting efficiency (ε_γ) and purity (f_p)[6] described in chapter fifth.:

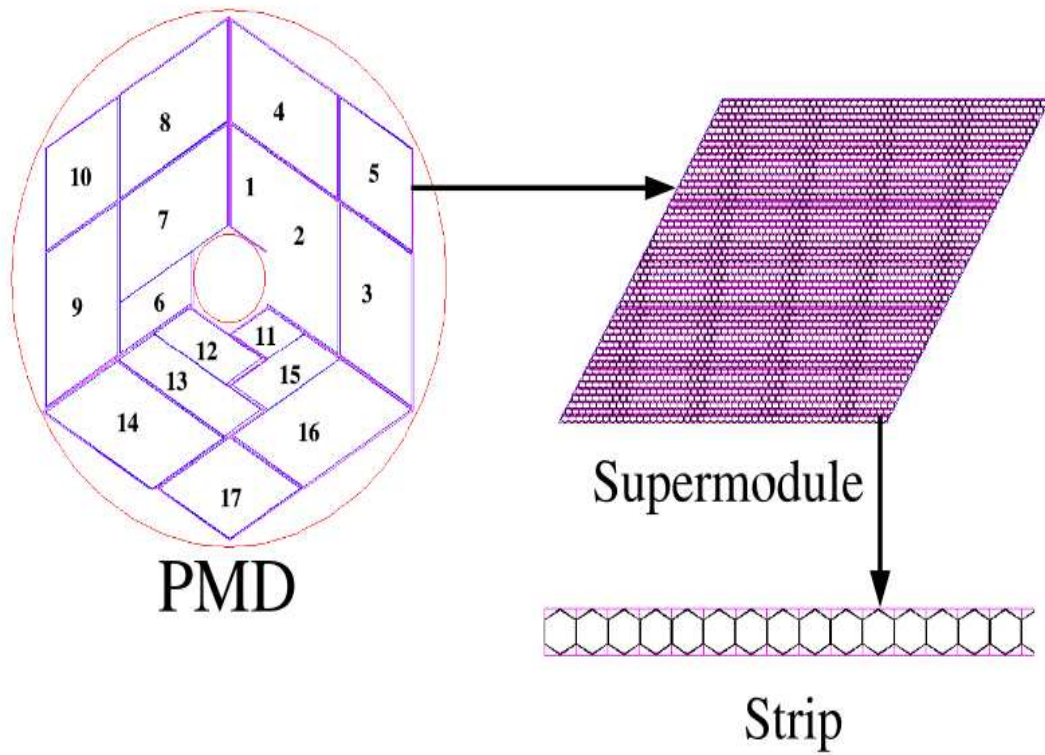


Figure 3.14: Layout of Photon Multiplicity Detector (PMD) in GSTAR framework.

Bibliography

- [1] "Photon Multiplicity Detector for STAR: Technical Proposal", VECC Internal Report VECC/EQG/00-04, May 2000, revised : Jan.2001.
- [2] M. M. Aggarwal et.al. Nucl.Instrum.Meth.A 499, 751-761 (2003); Nucl. Instr. Meth. A 488, 131 (2002).
- [3] M.M. Aggarwal et al., Nucl. Instr. Meth. Res. 13636 (2002).
- [4] J.D. Bjorken, Phys. Rev. D27, 140 (1983); J.W. Harris and B. Muller, Ann. Rev. Nucl. Part. Sci. 46, 71 (1996) and references therein.
- [5] M.M. Aggarwal et al., Nucl. Instr. Meth. A372 (1996) 143.
- [6] M.M. Aggarwal et al., Nucl. Instr. Meth. A421 (1999) 558.
- [7] ALICE PMD Technical Design Report, CERN/LHCC-32 (1999).
- [8] ALICE PMD Technical Design Report, CERN/LHCC 99-32 (1999).
- [9] F. Takasi, Phys. Rev. Lett. 53 (1984) 427.
- [10] M.M. Aggarwal, V.S. Bhatia, A.C. Das and Y.P. Viyogi, Phys. Lett. B 438 (1998) 357.
- [11] A.C. Das and Y.P. Viyogi, Phys. Lett. B 380 (1996) 437.
- [12] B. Mohanty and B. Serreuu, Phys. Rept. 414 (2005) 263.

- [13] M.M. Aggarwal et al., (WA98 Collaboration), Phys. Lett. B 420 (1998) 169.
- [14] T.K. Nayak et al., (WA98 Collaboration), Nucl. Phys. A 638 (1998) 2496.
- [15] M.M. Aggarwal et al., Nucl. Instr. Meth. sec. A, (in press), nucl-ex/0112016.
- [16] ALICE HMPID Technical Design Report, CERN/LHCC 98-19 (1998).
- [17] M. M. Aggarwal et al ., Phys. Rev. Lett. 85, 3595 (2000).
- [18] C. Adler, Phy. Rev. C66, 061901(R) (2002).

Chapter 4

Event-by-Event Fluctuations in Kaon to Pion ratio (K/π) at RHIC

4.1 Introduction

Any physical quantity in an experiment is subject to fluctuations. In general these fluctuations depend on the properties of the system and may contain important information about that system. In the context of relativistic heavy-ion collisions, the system under consideration is a dense and hot fireball consisting of hadronic or possibly partonic matter. The obvious challenge is to positively identify the existence of a state of partonic matter early in the life of the fireball. The study of fluctuations may help in this task. In thermal system, fluctuations are directly related to its various susceptibilities [1], which in turn are good indicators for possible phase changes. Basically in system, fluctuations have contributions of different nature. Some fluctuations are ‘trivial’ due to a finite number of particles used to define a particular observable in a given event. These fluctuations due to finite multiplicity are called as statistical fluctuations. Statistical fluctuations can be evaluated by considering the production of all particles as totally independent. All other fluctuations are of dynamical in nature and shall be called as dy-

namical fluctuations. Dynamical fluctuations are further subdivided into two classes (i) fluctuations which do not change event-by-event (for example two particle correlations due to Bose-Einstein statistics or due to resonance decays) and (ii) fluctuations which occur on an event-by-event basis, call it as event-by-event fluctuations. For example fluctuations arise in the ratio of charged to neutral particle multiplicities due to creation of regions of domains of Disoriented Chiral Condensate (DCC) or the fluctuations in anisotropic flow due to creations of regions with unusually soft or hard equation of state.

4.2 Earlier Measurements and Motivation

The unique opportunity to create extended regions of superdense deconfined matter in the laboratory is one of the most fascinating motivations for relativistic heavy-ion collisions. Various experiments have been performed to investigate whether such high-energy-density matter can actually be formed.

Also Quantum Chromodynamics (QCD) predicts that at sufficiently high energy density strongly interacting matter will undergo a phase transition from hadronic matter to a deconfined state of quarks and gluons, the Quark-Gluon Plasma (QGP) state [2, 3]. To create and study this state of matter in the laboratory collisions of heavy-ions are studied at various laboratories worldwide. A key question of the heavy-ion collision at Relativistic Heavy-Ion Collider (RHIC) at Brookhaven National Laboratory (BNL), USA is to understand whether the hot matter produced in the midst of heavy-ion collisions undergoes a transition to and from a Quark-Gluon Plasma (QGP) phase before it hadronizes. One of the signal of such a QGP phase transition could be a strong modification in the fluctuations of specific observables measured event-by-event basis in a collision [4].

Analysis of the event wise ratio of charged kaons to charged pions was performed in central Pb+Pb collisions at 158 A GeV by NA49 collaboration [5, 6, 7]. The non-statistical fluctuations of 2.8% observed in the data were found to be significantly smaller than those expected for an independent superposition of nucleon-nucleon collisions [5]. This supports the interpretation that at the top SPS energy each collision samples the same flavour ratios as described in a grand canonical ensemble, combined with a smooth transition from a possible partonic state to the final-state hadronic particle composition. The minimal fluctuations expected due to production of the final-state hadrons via resonances completely exhaust the observed fluctuation signal [8].

NA49 experiment also reported strength of dynamical fluctuations on event-by-event basis in the kaon to pion ratio in central Pb+Pb collisions at $\sqrt{S_{NN}} = 6.3, 7.6, 8.8, 12.3$ and 17.3 GeV by using the variable σ_{dyn} [5, 9]. The observed strength of dynamical fluctuations are positive and decrease with beam energy. They observed a energy dependence fluctuation signal. Dynamical fluctuations for the kaon to pion ratio at $\sqrt{S_{NN}} = 7$ GeV are larger than those predicted by the transport model UrQMD. Recently a horn like structure in the excitation function for the ratio of K^+/π^+ has been observed in central Pb+Pb collisions near $\sqrt{S_{NN}} = 7$ GeV [10]. Whereas step like structure in the excitation function for the ratio K^-/π^- was observed around the same energy. These observations have generated speculation that a phase transition from hadronic matter to quark-gluon matter may be taking place at SPS energy regime [11, 12].

Also enhanced production of strangeness has been suggested to be a signature of phase transition and the same is observed through K/ π ratio at SPS [13] energies. The frequency of production and size of Quark-Gluon Plasma (QGP) droplets depends upon

collision impact parameter. We expect larger and more frequent Quark-Gluon Plasma (QGP) droplets production in central collisions. An increase in the size and production frequency of QGP droplets with increasing collision centrality might then be signaled by sudden change in the fluctuations of produced particles such as kaons and pions. Theoretical investigation carried out by J. Kapusta and A. Mekjian [14] suggested that fluctuations in the kaon-to-pion total-yield ratio, due to supercooling-reheating fluctuations produced by a predicted large enthalpy difference in the two phases. The kaon to pion ratio was shown to fluctuate by about 10%, over the domain of conceivable hadronization temperatures ($140 < T < 200$) MeV [15]. This prediction would be experimentally testable if the K/π ratio could be quantified for individual central collision events [16].

In this chapter data is analysed on event-by-event basis for fluctuations in kaon to pion (K/π) ratio for central Cu+Cu interactions at $\sqrt{S_{NN}} = 62.4$ and 200 GeV recorded by Time Projection Chamber (TPC) [17] in hybrid STAR experiment at Relativistic Heavy-Ion Collider (RHIC) BNL, New-York, USA. Results are discussed, based on two different measures of fluctuations providing information of dynamical fluctuations after correcting for the statistical fluctuations. Fluctuations strength measured by the quantity called ν_{dyn} [18] are discussed. The centrality and energy dependence of these fluctuations strengths and comparison with theoretical model predictions are described.

An attempt also has been made to compare the observed K/π dynamical fluctuations in central Cu+Cu interaction at $\sqrt{S_{NN}} = 62.4$ and 200 GeV with the measurements reported by NA49 collaboration in the central Pb+Pb interactions [5, 6, 7, 9] at SPS energies and STAR collaboration in central Au+Au interactions at RHIC energies [19, 20, 21].

4.3 Data Analysis

The details of analysis procedures followed are described below.

4.3.1 Data Set Used

For the present analysis we used a data set of Cu+Cu interactions at $\sqrt{S_{NN}} = 62.4$ and 200 GeV recorded by Time Projection Chamber (TPC) in the STAR experiment collected in the year 2005 at the relativistic Heavy-Ion Collider (RHIC) at Brookhaven National Laboratory (BNL), USA. All the data sets used for the present analysis were taken by using a minimum biased trigger.

4.3.2 Data Quality Cuts

For physics analysis we have used several quality cuts on the data to remove bad events from the available experimental data. Only those events are accepted that took place within ± 15 cm of the center of the STAR detector in the beam direction. All tracks were required to have originated within 3 cm of the measured event vertex. Only charged particle tracks having more than 15 space points along the trajectory were accepted. The ratio of reconstructed space points to possible space points along the track was required to be greater than 0.52 to avoid double tracks. As described in chapter two that charged kaons and charged pions were identified using the specific energy loss, dE/dx along the track and the momentum of the track. Charged kaons and pions were measured with transverse momentum $0.2 < p_t < 0.6$ GeV/c and pseudorapidity $|\eta| < 1.0$. Particle

identification was accomplished by selecting particles whose specific energy losses were within two standard deviations of the range-energy expectations for a given particle type and momentum. Particle identification for pions and kaons also included a condition that the specific energy loss should be more than two standard deviations away from the loss expected for a kaon (pion). In addition, electrons were also excluded from the data. Particles were excluded as electrons if the specific energy losses were within one standard deviation of the range-energy predictions for electrons. All data quality cuts are summarized in the table 4.1 for quick reference.

Parameter	Cut Value
Z Vertex	-15 to 15 cm
Transverse Momentum (Pt)	200 MeV to 600 MeV
Pseudorapidity(η)	$ \eta < 1.0$
DCA (Primary Track to Vertex)	3.0 cm
nHits	> 15
nFits/nHits	> 0.52
nSigmaElectron	> 1.0
Kaons	nSigmaKaon < 2 and nSigmaPion > 2
Pions	nSigmaPion < 2 and nSigmaKaon > 2

Table 4.1: **Data quality cuts used for analysis.**

4.4 Dynamical Fluctuations in Cu+Cu

Strange particle production is an important experimental observable that allows the study of the strongly interacting matter created in relativistic heavy-ion collisions. The unique capability of STAR experiment at RHIC of measuring identified strange particles over a wide range of acceptance to investigate the strength of dynamical fluctuations in kaon to pion ratio on event-by-event basis for the central Cu+Cu interactions. The dynamical fluctuations is equal to the difference between total fluctuations and statistical fluctuations. For measuring dynamical fluctuations it is necessary to estimate the statistical fluctuations which arises due to finite number density of the produced particles and experimental resolution in dE/dx . To estimate the strength of dynamical fluctuations in the distribution of a quantity, it is important to know the contribution from the statistical fluctuations into it. One of the ways to obtain this is to compare the distribution with a distribution of events with statistical fluctuations only. The technique of event mixing has been proved very useful in producing the reference points with statistical variation from event to event.

Mixed events are constructed by taking one track from each event randomly, reproducing the multiplicity distributions of the real events. All the parameters of the track is kept in the mixed event array and using the same cuts as the real events. By construction, the mixed events on average have the same multiplicity as that of real events and also have the same kaon to pion ratio as the real events, but devoid of internal correlations.

Also due to the constraint on the overall multiplicity distributions the mixed data gave an accurate estimate of finite-number fluctuations in the kaon and pion multiplicities. The mixed events therefore automatically include all the effects of detector

resolution. These are subjected to the same maximum likelihood fit procedure as the real events, allowing a direct comparison with the real data.

Centrality	$\langle \text{Pion} \rangle$ Multiplicity (Real)	$\langle \text{Pion} \rangle$ Multiplicity (Mixed)
0-10%	$\langle 102.2 \rangle$	$\langle 102.2 \rangle$
10-20%	$\langle 73.71 \rangle$	$\langle 73.73 \rangle$
20-30%	$\langle 51.66 \rangle$	$\langle 51.66 \rangle$
30-40%	$\langle 35.18 \rangle$	$\langle 35.18 \rangle$
40-50%	$\langle 26.08 \rangle$	$\langle 26.06 \rangle$
Centrality	$\langle \text{Kaon} \rangle$ Multiplicity (Real)	$\langle \text{Kaon} \rangle$ Multiplicity (Mixed)
0-10%	$\langle 4.92 \rangle$	$\langle 4.91 \rangle$
10-20%	$\langle 3.56 \rangle$	$\langle 3.55 \rangle$
20-30%	$\langle 2.47 \rangle$	$\langle 2.46 \rangle$
30-40%	$\langle 1.67 \rangle$	$\langle 1.67 \rangle$
40-50%	$\langle 1.21 \rangle$	$\langle 1.21 \rangle$

Table 4.2: **Average Pion and Kaon multiplicities values for Cu+Cu interactions at $\sqrt{S_{NN}} = 62.4$ GeV from real and mixed event data.**

Figure 4.1 and 4.2 shows the event-by-event pion and kaon multiplicity distributions for top (0-10%) central Cu+Cu interactions at $\sqrt{S_{NN}} = 62.4$ and 200 GeV for both data and mixed events respectively. For different centrality classes, in table 4.2 and 4.3 we listed the average pion and kaon multiplicities values for Cu+Cu interactions at $\sqrt{S_{NN}} = 62.4$ and 200 GeV respectively from both real and mixed events data. It is observed that the average multiplicities values from both real and mixed events data are very close to each other and indicating that mixed events were correctly constructed.

Centrality	$\langle \text{Pion} \rangle$ Multiplicity (Real)	$\langle \text{Pion} \rangle$ Multiplicity (Mixed)
0-10%	$\langle 140.0 \rangle$	$\langle 140.0 \rangle$
10-20%	$\langle 98.92 \rangle$	$\langle 98.87 \rangle$
20-30%	$\langle 70.59 \rangle$	$\langle 70.55 \rangle$
30-40%	$\langle 49.06 \rangle$	$\langle 49.09 \rangle$
40-50%	$\langle 32.95 \rangle$	$\langle 32.96 \rangle$
Centrality	$\langle \text{Kaon} \rangle$ Multiplicity (Real)	$\langle \text{Kaon} \rangle$ Multiplicity (Mixed)
0-10%	$\langle 6.55 \rangle$	$\langle 6.55 \rangle$
10-20%	$\langle 4.72 \rangle$	$\langle 4.71 \rangle$
20-30%	$\langle 3.38 \rangle$	$\langle 3.40 \rangle$
30-40%	$\langle 2.41 \rangle$	$\langle 2.40 \rangle$
40-50%	$\langle 1.58 \rangle$	$\langle 1.58 \rangle$

Table 4.3: **Average Pion and Kaon multiplicities values for Cu+Cu interactions at $\sqrt{s_{NN}} = 200$ GeV from real and mixed event data.**

The statistical fluctuations are measured from the width of the distributions obtained from mixed events data. The statistical contributions are subtracted from the real data to estimate the measure of strength of dynamical fluctuations in terms of a variable called sigma dynamical (σ_{dyn}) obtained as :

$$\sigma_{dyn} = \sqrt{\sigma_{data}^2 - \sigma_{mixed}^2} \quad (4.1)$$

where $\sigma_{data} = RMS_{data}/Mean_{data}$ is the width of the distributions of real experimental data and $\sigma_{mixed} = RMS_{mixed}/Mean_{mixed}$ is the width of the mixed event dis-

tributions. Figure 4.3 and 4.4 shows the K/π ratio distributions for central Cu+Cu interactions at $\sqrt{S_{NN}} = 62.4$ and 200 GeV respectively and their comparison with mixed events. In the figure the solid line represent mixed events and filled circles corresponds to experimental data.

The observed width of the real data distributions for Cu+Cu at $\sqrt{S_{NN}} = 62.4$ GeV is 47.04 % and for Cu+Cu at $\sqrt{S_{NN}} = 200$ GeV is 40.96 %. The width of the mixed event distributions for Cu+Cu at $\sqrt{S_{NN}} = 62.4$ GeV is 46.96 % and for Cu+Cu at $\sqrt{S_{NN}} = 200$ GeV is 40.65 %. The small difference between data and mixed events illustrates that any quantum of correlations or anticorrelations in the final multiplicities is very small. The measured strength of dynamical fluctuations in Cu+Cu data and their comparison with earlier results are discussed in the following section.

4.4.1 Comparison with NA49 (SPS) and Au+Au (STAR RHIC)

The measured dynamical fluctuations obtained from equation (4.1) for central Cu+Cu interactions at $\sqrt{S_{NN}} = 62.4$ and 200 GeV are compared with NA49 results for central Pb+Pb interactions at $\sqrt{S_{NN}} = 6.3, 7.6, 8.8, 12.3$ and 17.3 GeV in figure 4.5. The STAR results for central Au+Au interactions at $\sqrt{S_{NN}} = 20, 130, 62.4$ and 200 GeV [19, 20, 21] are also plotted in figure 4.5 as a function of beam energy.

The error bar shown in the present analysis for Cu+Cu collisions are sum of the statistical and systematic errors. The systematic errors of the fluctuations measurements is estimated by varying sets of data quality cuts. The number of events analyzed are very large (~ 6 million for 200 GeV and ~ 5 million for 62.4 GeV), so statistical errors are very small. The statistical errors corresponding to theoretical model predictions shown

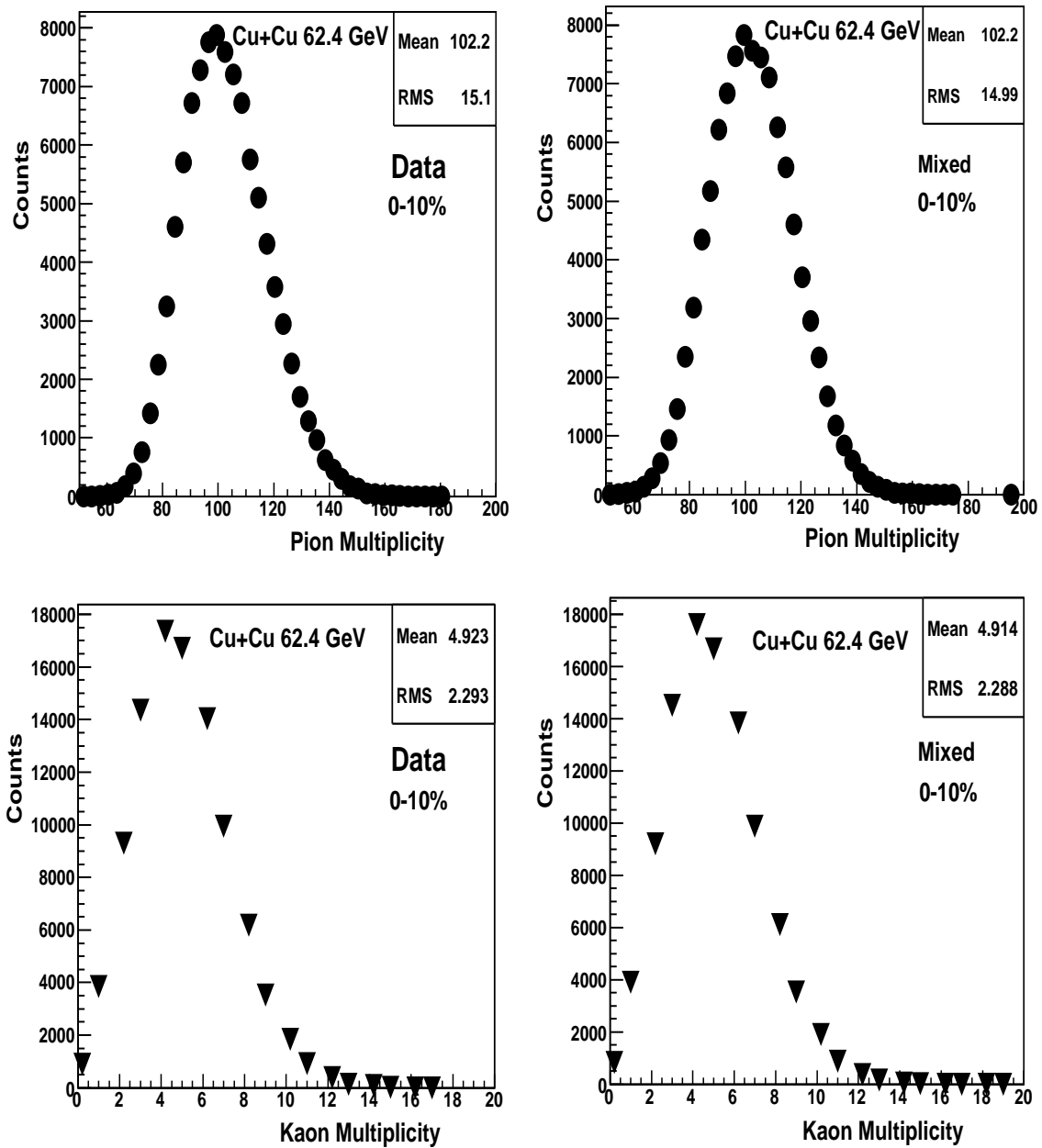


Figure 4.1: The multiplicity distributions for real and mixed events for Cu+Cu interactions at $\sqrt{s_{NN}} = 62.4$ GeV. The mean multiplicity values for both data and mixed events are in close agreement.

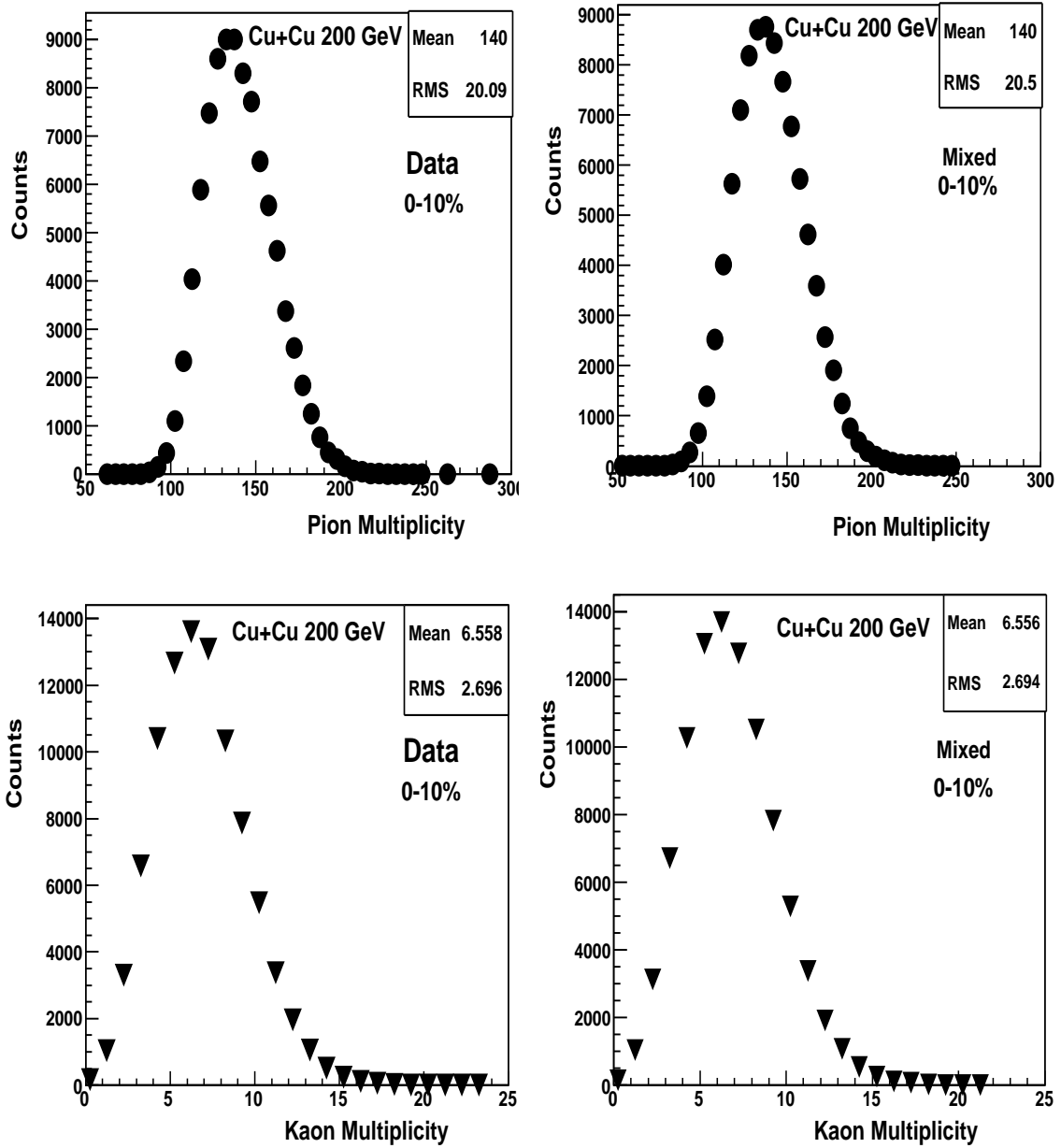


Figure 4.2: The multiplicity distributions for real and mixed events for Cu+Cu interactions at $\sqrt{s_{NN}} = 200$ GeV. The mean multiplicity values for both data and mixed events are in close agreement.

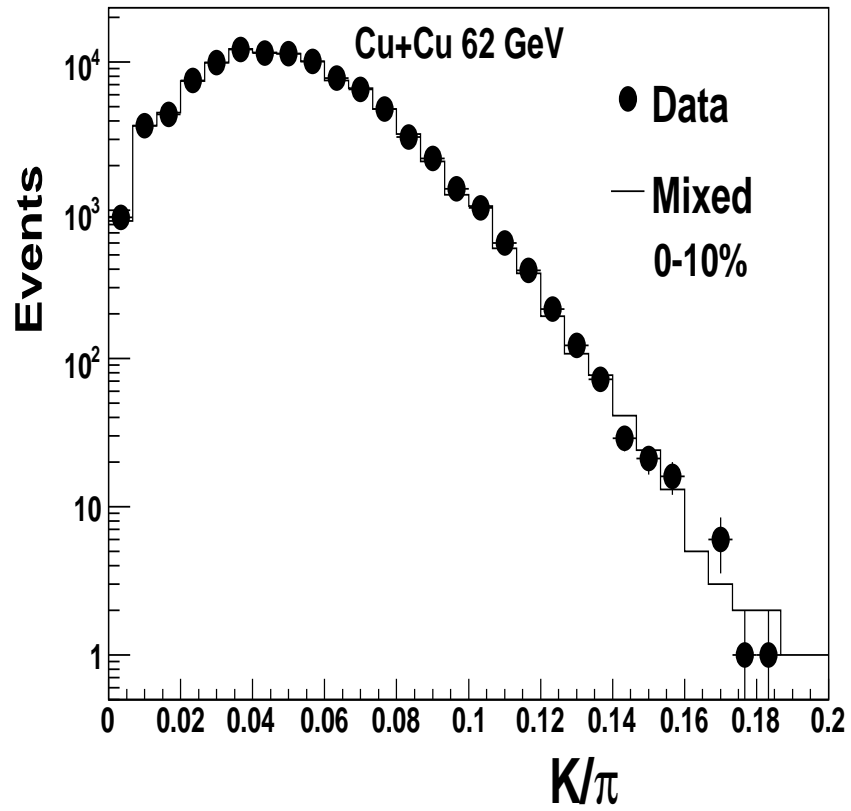


Figure 4.3: The event-by-event k/π ratio for Cu+Cu interactions at $\sqrt{S_{NN}} = 62.4$ GeV compared with the same quantity calculated from mixed events.

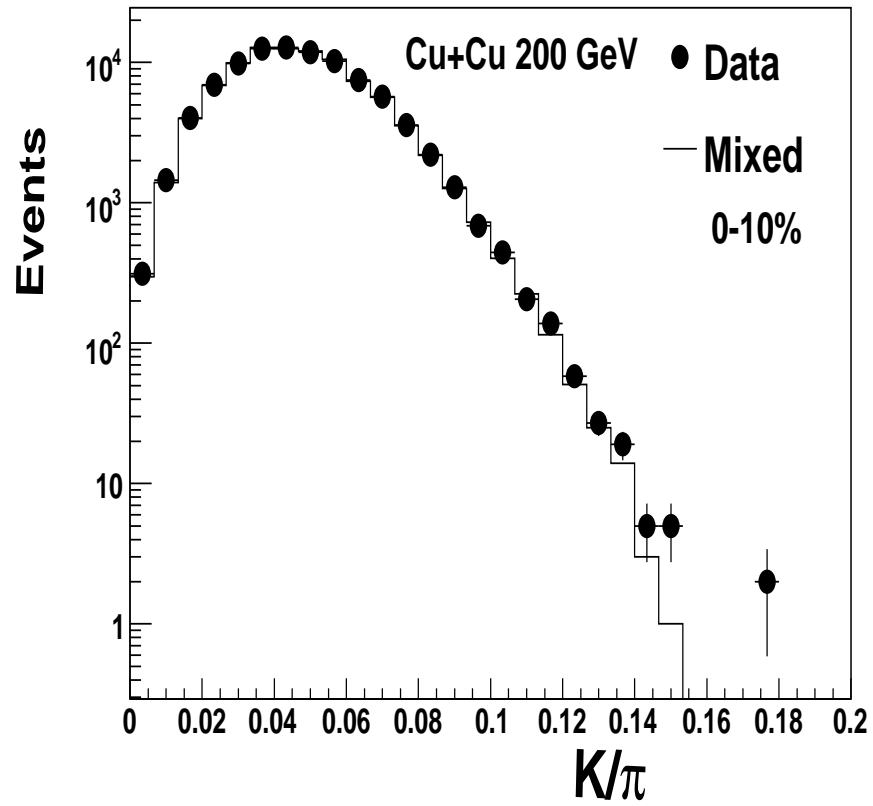


Figure 4.4: The event-by-event k/π ratio for Cu+Cu interactions at $\sqrt{s_{NN}} = 200$ GeV compared with the same quantity calculated from mixed events.

in various figures are within symbol size.

The following observations can be made: where as NA49 results indicate strong decrease in the dynamic fluctuation component with increase in the beam energy in the region $6.3 \text{ GeV} \leq \sqrt{S_{NN}} \leq 17.3 \text{ GeV}$. STAR data for Au+Au collisions in the energy range $20 \text{ GeV} \leq \sqrt{S_{NN}} \leq 200 \text{ GeV}$ show near constant values for $\sigma_{dyn}(\%)$ within large errors. No dependence of $\sigma_{dyn}(\%)$ is however seen on the size of the collision system when results from Cu+Cu interactions compared with Au+Au interactions.

4.4.2 Comparison with Statistical Hadronization Model

The observed strength of dynamical fluctuations in kaon to pion (K/π) ratio compared with Statistical Hadronization (SH) model [22] is shown in figure 4.6. It is observed that when the light quark phase space occupancy, $\gamma_q = 1$, corresponding to equilibrium scenario, the kaon to pion ratio calculations underestimate the experimental results at all energies. The calculations incorporating a fitted γ_q , corresponding to $\gamma_q > 1$ (non-equilibrium or over saturation at RHIC energies), are consistent with dynamical fluctuations at the higher energies but shows disagreement with the data at the lower energies of $\sqrt{S_{NN}} < 15 \text{ GeV}$.

4.5 $\nu_{dyn}(K\pi)$ Variable Study in Cu+Cu

The event-by-event fluctuations in any observable can be expressed in terms of inclusive multiparticle production. This approach was first proposed in [23], is derived from single and two particle distribution functions. In this method the dynamical fluctuations have been expressed as [18]:

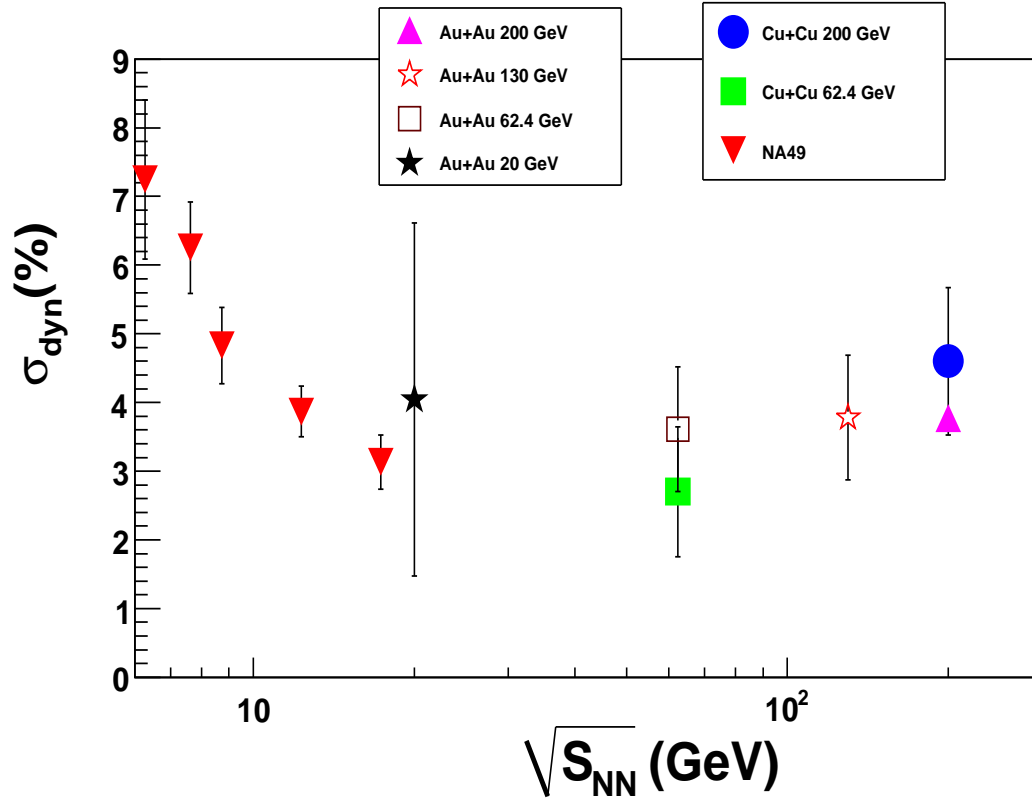


Figure 4.5: Measured dynamical K/π fluctuations in terms of σ_{dyn} for central Cu+Cu interactions at $\sqrt{S_{NN}} = 62.4$ and 200 GeV and compared with the earlier measurements as a function of beam energy.

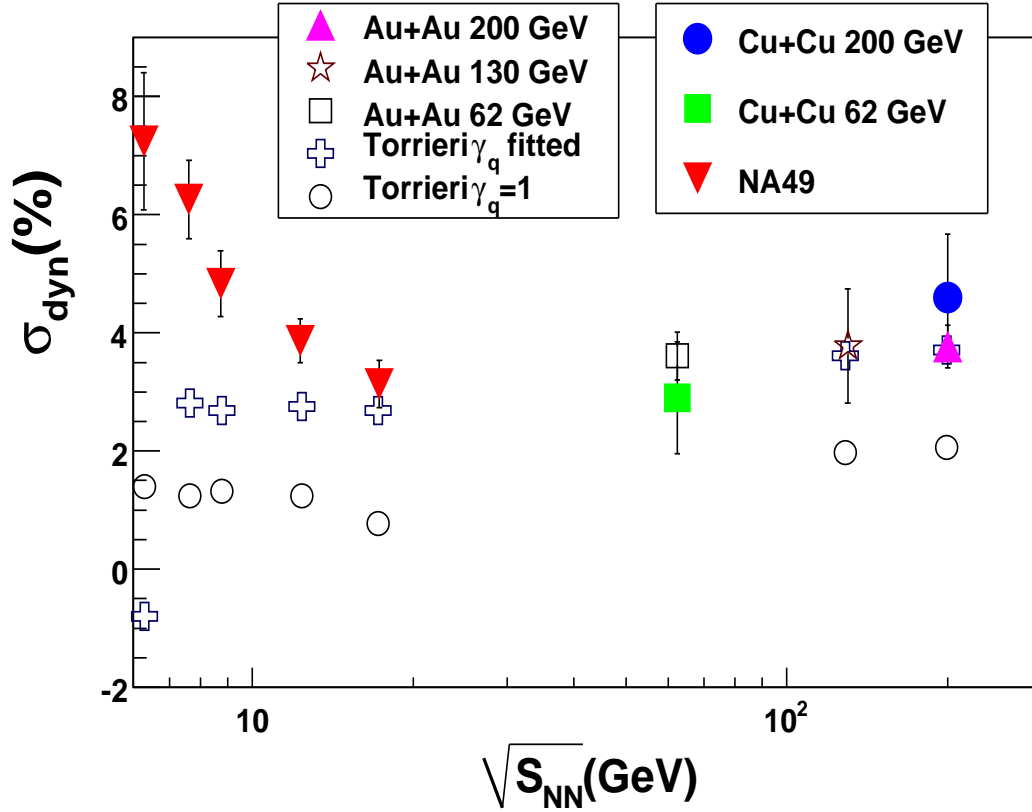


Figure 4.6: The measured dynamical K/π fluctuations in terms of σ_{dyn} for central Cu+Cu interactions at $\sqrt{S_{NN}} = 62.4$ and 200 GeV compared with results from NA49, STAR Au+Au and statistical hadronization (SH) model.

$$\nu_{+-,dyn} = \overline{R}_{++} + \overline{R}_{--} - 2\overline{R}_{+-} \quad (4.2)$$

where \overline{R}_{ab} with $a, b = +, -$ are the averages of the correlation functions often used in multiparticle production analysis [24, 25, 26]. The three terms in the above equation are constructed as:

$$\overline{R}_{ab} = \frac{\int_{\Delta\eta} R_{2,ab}(\eta_a, \eta_b) \rho_{1,a}(\eta_a) \rho_{1,b}(\eta_b) d\eta_a d\eta_b}{\int_{\Delta\eta} \rho_{1,a}(\eta_a) d\eta_a \int_{\Delta\eta} \rho_{1,b}(\eta_b) d\eta_b} \quad (4.3)$$

where, $R_{2,ab} = \rho_2(\eta_a, \eta_b) / [\rho_{1,a}(\eta_a) \rho_{1,b}(\eta_b)] - 1$, $\rho_1(\eta) = dn/d\eta$, and $\rho_2(\eta_a, \eta_b) = d^2n/d\eta_a d\eta_b$ are single, and two-particle pseudorapidity densities respectively. The integrals could most generally be taken over the full particle phase space (d^3p). In cases where the produced particles are totally uncorrelated, two particle densities can be factorized as products of two single particle densities. The correlators \overline{R}_{ab} shall then vanish, and the measured dynamical fluctuations $\nu_{+-,dyn}$ should be identically zero. A deviation from zero thus should indicate correlations in particle production. If correlations are due to production via many subcollisions, localized sources, or clusters, one should further expect the strength of the correlation to be finite but increasingly diluted with increased number of production clusters or subcollisions. The correlators \overline{R}_{ab} will be inversely proportional to the multiplicity of clusters, and thus also inversely proportional to the total measured multiplicity of charged particles [18].

Similar approach has been used in the measurement of the net charge fluctuation analysis by STAR collaboration [27] where $\nu_{+-,dyn}$ takes a form like

,

$$\nu_{+-,dyn} = \frac{\langle N_+(N_+-1) \rangle}{\langle N_+ \rangle^2} + \frac{\langle N_-(N_- -1) \rangle}{\langle N_- \rangle^2} - 2 \frac{\langle N_+ N_- \rangle}{\langle N_+ \rangle \langle N_- \rangle} \quad (4.4)$$

where N_+ and N_- are respectively the multiplicities of positive and negative particles.

Since the variable σ_{dyn} has the disadvantage of involving the K/π ratio directly and therefore has difficulties at low multiplicities. This necessitates the study of K/π fluctuations using a variable called ν_{dyn} defined above that does not involve the K/π ratio directly and properly deals with low multiplicity events. By replacing the event-by-event multiplicities of positive and negative charges by those of kaon (K) and pion (π), the equation (4.4) takes the following form

$$\nu_{dyn}(K\pi) = \frac{\langle N_K(N_K-1) \rangle}{\langle N_K \rangle^2} + \frac{\langle N_\pi(N_\pi-1) \rangle}{\langle N_\pi \rangle^2} - 2 \frac{\langle N_K N_\pi \rangle}{\langle N_K \rangle \langle N_\pi \rangle} \quad (4.5)$$

where N_K and N_π is the number of kaons and pions respectively in each event. The first term in the right side of above equation (4.5) represents the correlation among the kaons only, second term represents the correlation among the pions only and the third term represents the correlations among the kaons and pions. The variable $\nu_{dyn}(K\pi)$ quantifies the difference between the observed K/π fluctuations and those expected from Poisson statistics. The significance of using this variable $\nu_{dyn}(K\pi)$ is discussed in detail in Ref.[18]. One important advantage of this variable is that this does not require mixed events.

In figure 4.7 and 4.8, we have plotted $\nu_{dyn}(K\pi)$ for Cu+Cu interactions at $\sqrt{S_{NN}} = 62.4$ and 200 GeV as a function of number of participating nucleons (N_{part}) and as a function of pseudorapidity density ($dN/d\eta$) respectively. We observed that the variation of $\nu_{dyn}(K\pi)$ for both the energies are consistent within the systematic errors and shows

energy independence of the colliding system. However, a strong dependence is seen on the centrality of the events. The variable shows sensitivity for peripheral interactions and sharply falls in value with increase in overlap region of interaction.

The solid line in the figures are from fit functions $a+b/N_{part}$ and $c+d/dN/d\eta$, where a,b,c and d are constants. The various fit parameters are listed in the table 4.4. From fit parameters it is observed that the fit for $\nu_{dyn}(K\pi)$ versus $dN/d\eta$ is better than the fit for $\nu_{dyn}(K\pi)$ versus N_{part} . It is observed that the fluctuations strength measured by ν_{dyn} variable decreases with increasing centrality. This is due to the fact that the correlation strength gets diluted at higher multiplicity environment.

System	Energies (GeV)	Fit Function	a	b	χ^2/ndf
Cu+Cu	62.4, 200	$a + b/N_{part}$	0.001578	0.1618	2.572/2
System	Energies (GeV)	Fit Function	c	d	χ^2/ndf
Cu+Cu	62.4, 200	$c + d/dN/d\eta$	0.002008	0.1882	2.407/2

Table 4.4: Listed fitting parameter.

4.5.1 Comparison with Au+Au (STAR) and NA49 (SPS)

In figure 4.9 $\nu_{dyn}(K\pi)$ for Cu+Cu interactions data is plotted as a function of pseudo-rapidity density ($dN/d\eta$). The results are compared with Au+Au collisions at $\sqrt{S_{NN}} = 62.4$ and 200 GeV and the NA49 results using the identity $\sigma_{dyn}^2 = \nu_{dyn}(K\pi)$. The measured dynamical fluctuations strength is observed to be independent of colliding system and energy.

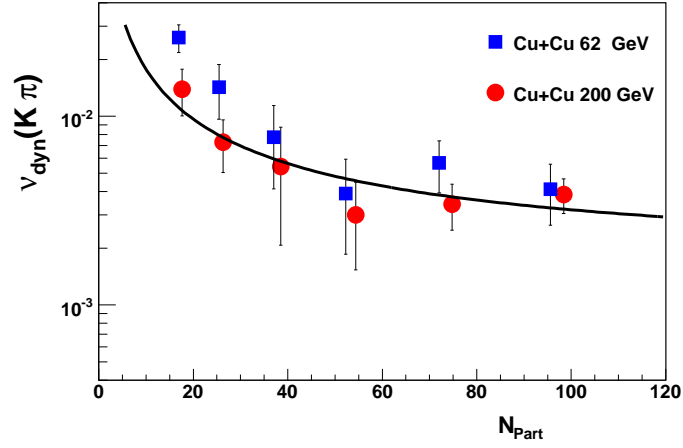


Figure 4.7: The measured dynamical K/π fluctuations in terms of $\nu_{dyn}(K\pi)$ for Cu+Cu interactions at $\sqrt{S_{NN}} = 62.4$ and 200 GeV as a function of number of participating nucleons (N_{part}). The solid line is drawn from fit function $a+b/N_{part}$.

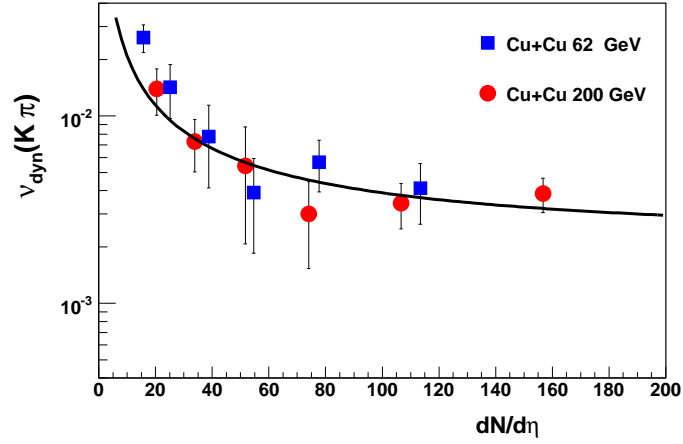


Figure 4.8: The measured dynamical K/π fluctuations in terms of $\nu_{dyn}(K\pi)$ for Cu+Cu interactions at $\sqrt{S_{NN}} = 62.4$ and 200 GeV as a function of pseudorapidity density ($dN/d\eta$). The solid line is drawn from fit function $c+d/dN/d\eta$.

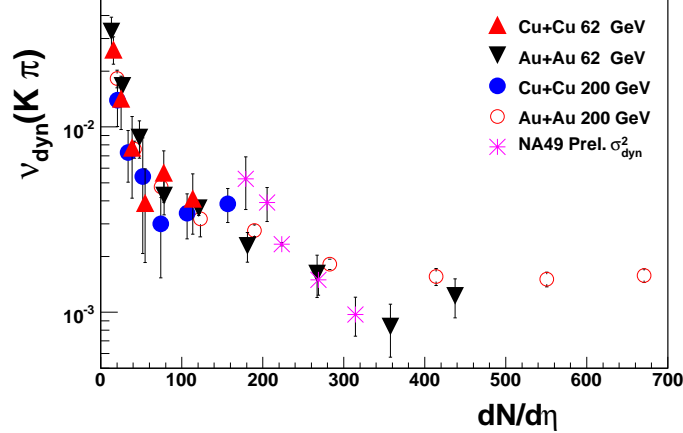


Figure 4.9: The measured dynamical K/π fluctuations in terms of $\nu_{dyn}(k\pi)$ for Cu+Cu interactions at $\sqrt{S_{NN}} = 62.4$ and 200 GeV as a function of pseudorapidity density ($dN/d\eta$) and their comparison with STAR Au+Au and NA49 Pb+Pb results.

4.5.2 $\nu_{dyn}(K\pi)$ Variable Study From Theoretical Model

An attempt has been made to calculate $\nu_{dyn}(K\pi)$ from theoretical model and compared with the experimental observations. Here, we used Heavy-Ion Jet Interaction Generator (HIJING)[28] and A Multi-Phase Transport (AMPT) model [29] event generator by using the same kinematic cuts as used for the experimental data. The AMPT model uses HIJING as initial particle production in addition to hadronic evolution (multiple re-scattering).

The $\nu_{dyn}(K\pi)$ for Cu+Cu interactions at $\sqrt{S_{NN}} = 62.4$ and 200 GeV are shown in figure 4.10 and 4.11 as a function of number of participating nucleons (N_{part}) and pseudorapidity density ($dN/d\eta$) respectively from HIJING.

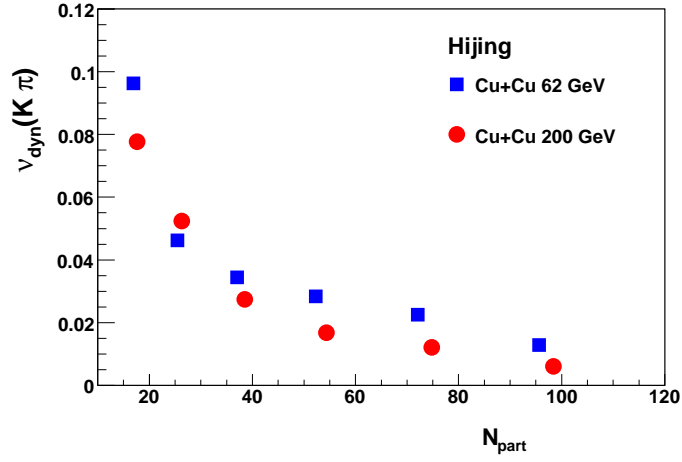


Figure 4.10: Shows the measured dynamical K/π fluctuations in terms of $\nu_{dyn}(K\pi)$ for Cu+Cu interactions at $\sqrt{S_{NN}} = 62.4$ and 200 GeV as a function of number of participating nucleons (N_{part}) from theoretical model (HIJING).

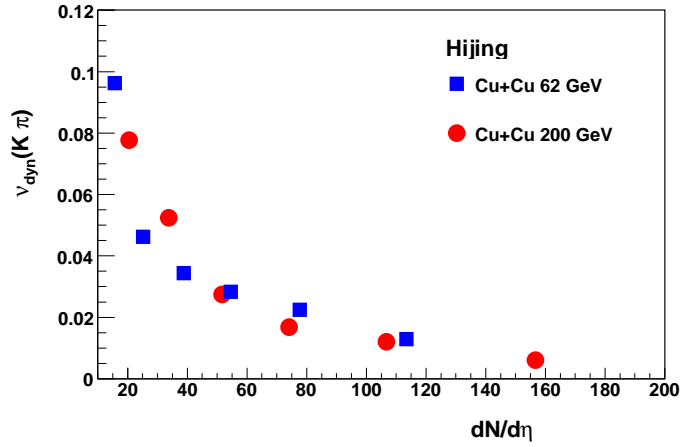


Figure 4.11: Shows the measured dynamical K/π fluctuations in terms of $\nu_{dyn}(K\pi)$ for Cu+Cu interactions at $\sqrt{S_{NN}} = 62.4$ and 200 GeV as a function of pseudorapidity density ($dN/d\eta$) from theoretical model (HIJING).

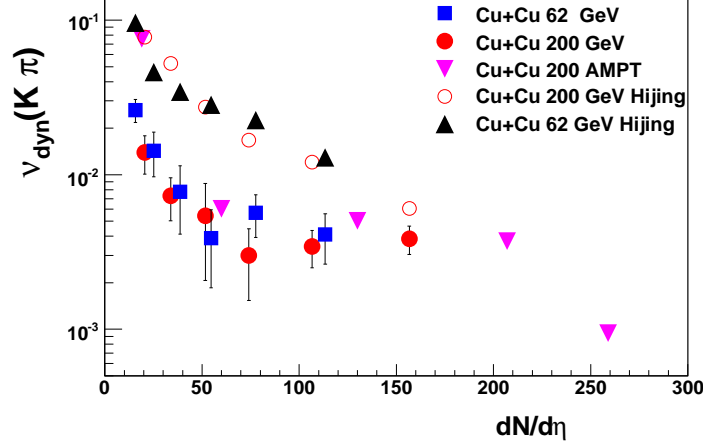


Figure 4.12: The measured dynamical K/π fluctuations in terms of $\nu_{dyn}(K\pi)$ for Cu+Cu interactions at $\sqrt{S_{NN}} = 62.4$ and 200 GeV as a function of pseudorapidity density ($dN/d\eta$) compared with HIJING and AMPT Model.

4.5.3 $\nu_{dyn}(K\pi)$ Comparison with HIJING and AMPT Model

In figure 4.12 we plotted measured dynamical K/π fluctuations in terms of $\nu_{dyn}(K\pi)$ for Cu+Cu interactions at $\sqrt{S_{NN}} = 62.4$ and 200 GeV as a function of pseudorapidity density ($dN/d\eta$) compared with the results from theoretical predictions (HIJING and AMPT Model). It is observed that the HIJING model over-predicts the experimentally measured K/π fluctuations whereas AMPT model predictions (HIJING+ re-scattering) are in better agreement with experimental data. This indicates that particle production in nucleus-nucleus collision is not simple superposition of nucleon-nucleon collisions.

4.5.4 $\nu_{dyn}(K\pi)$ for Same and Opposite signs

In order to gain insight into the origin of these $\nu_{dyn}(K\pi)$ fluctuations, we also calculate $\nu_{dyn}(K\pi)$ for other combinations like K^+/π^+ , K^-/π^- , K^+/π^- , K^-/π^+ . In figure 4.13 and 4.14 we have plotted $\nu_{dyn}(K\pi)$ for different combinations as a function of

pseudorapidity density ($dN/d\eta$) for Cu+Cu interactions at $\sqrt{S_{NN}} = 62.4$ and 200 GeV respectively. Similar exercise is carried out for theoretical model predictions (HIJING) and plotted in figure 4.15 and 4.16. We observed higher $\nu_{dyn}(K\pi)$ in summed charge than same and opposite sign in both data and HIJING. We also observe negative values of ν_{dyn} for some combinations (K^+/π^- , K^-/π^+) for lower $dN/d\eta$. This may arise if resonances (K^* decay into $K\pi$, $K\pi\pi$) are considered to be the sources of these particles. As one approaches towards the higher $dN/d\eta$, the role of resonances may get diluted and the values of ν_{dyn} move close to zero.

4.5.5 $\nu_{dyn}(K\pi)$ Scaled results

In order to understand and study centrality dependence behaviour of $\nu_{dyn}(K\pi)$, we scale it with pseudorapidity density ($dN/d\eta$). In figure 4.17 we have plotted $\nu_{dyn}(K\pi)$ scaled with $dN/d\eta$ for Cu+Cu interactions at $\sqrt{S_{NN}} = 62.4$ and 200 GeV and their comparison with Au+Au interactions at $\sqrt{S_{NN}} = 62.4$ and 200 GeV as a function of $dN/d\eta$. The data shows a steep rise in the scaled $\nu_{dyn}(K\pi)$ for higher particle density region obtained in Au+Au collisions. In figure 4.18 comparison of scaled $\nu_{dyn}(K\pi)$ fluctuations with HIJING and AMPT model is plotted. It is observed that HIJING fluctuations signal over predicts the experimental results, whereas AMPT model predictions are observed to be in better agreement with our experimental data results.

An attempt has also been made to plot the measured dynamical K/π fluctuations in terms of $\nu_{dyn}(K\pi)$ for Cu+Cu interactions at $\sqrt{S_{NN}} = 62.4$ and 200 GeV scaled with pseudorapidity density ($dN/d\eta$) as a function of pseudorapidity density ($dN/d\eta$) for different species of kaons and pions (K^+/π^+ , K^-/π^- , K^+/π^- , K^-/π^+) in figure 4.19 and 4.20 respectively. Similar exercise from HIJING are plotted in figure 4.21 and 4.22.

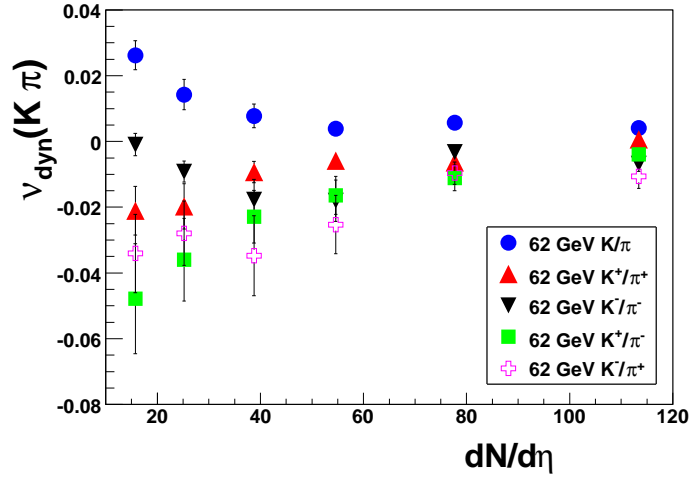


Figure 4.13: Measured dynamical K/π fluctuations in terms of $\nu_{dyn}(K\pi)$ for Cu+Cu interactions at $\sqrt{S_{NN}} = 62.4$ GeV for different combinations as a function of pseudorapidity density ($dN/d\eta$) from real data.

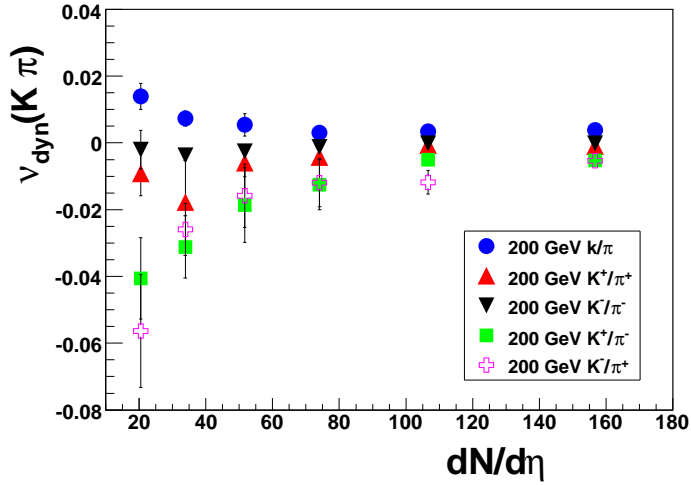


Figure 4.14: Measured dynamical K/π fluctuations in terms of $\nu_{dyn}(K\pi)$ for Cu+Cu interactions at $\sqrt{S_{NN}} = 200$ GeV for different combinations as a function of pseudorapidity density ($dN/d\eta$) from real data.

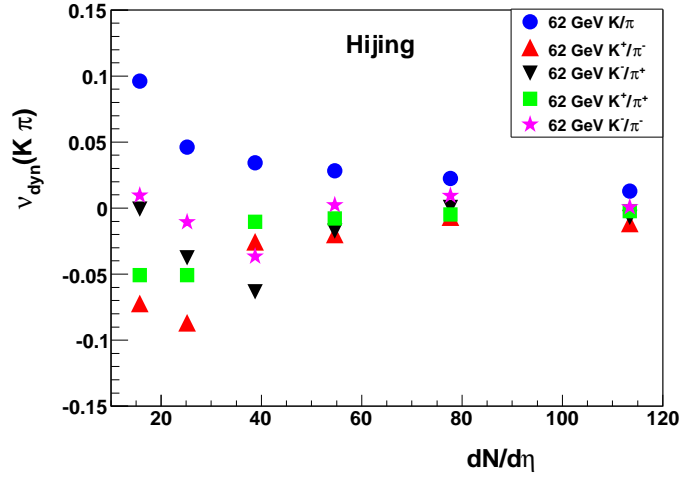


Figure 4.15: Shows the measured dynamical K/π fluctuations in terms of $\nu_{dyn}(K\pi)$ for Cu+Cu interactions at $\sqrt{S_{NN}} = 62.4$ GeV for different combinations as a function of pseudorapidity density ($dN/d\eta$) from HIJING.

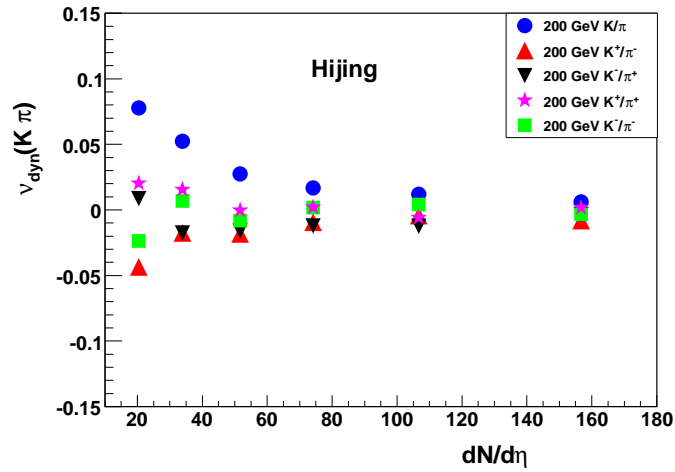


Figure 4.16: Shows the measured dynamical K/π fluctuations in terms of $\nu_{dyn}(K\pi)$ for Cu+Cu interactions at $\sqrt{S_{NN}} = 200$ GeV for different combinations as a function of pseudorapidity density ($dN/d\eta$) from HIJING.

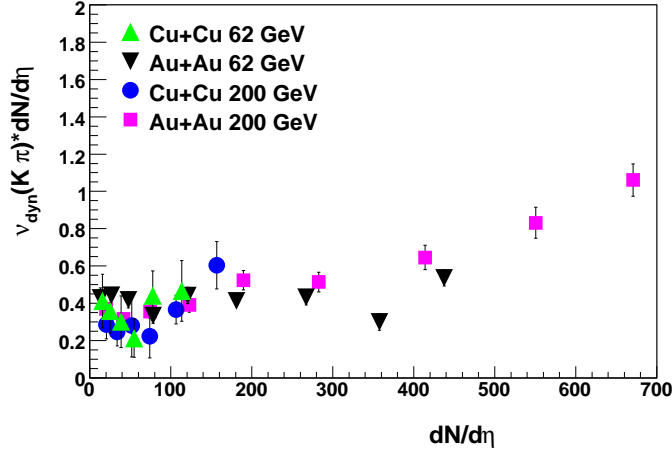


Figure 4.17: Measured dynamical K/π fluctuations in terms of $\nu_{dyn}(K\pi)$ for Cu+Cu interactions at $\sqrt{S_{NN}} = 62.4$ and 200 GeV scaled with pseudorapidity density ($dN/d\eta$) and their comparison with Au+Au study as a function of pseudorapidity density ($dN/d\eta$).

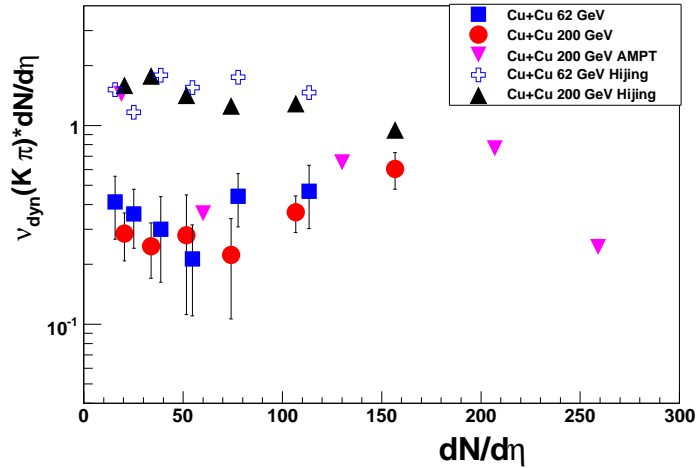


Figure 4.18: Measured dynamical K/π fluctuations in terms of $\nu_{dyn}(K\pi)$ for Cu+Cu interactions at $\sqrt{S_{NN}} = 62.4$ and 200 GeV scaled with pseudorapidity density ($dN/d\eta$) and their comparison with HIJING and AMPT model as a function of pseudorapidity density ($dN/d\eta$).

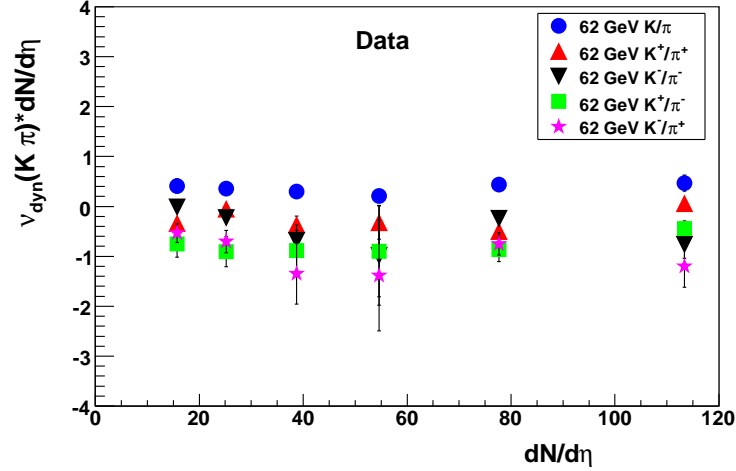


Figure 4.19: Measured dynamical K/π fluctuations in terms of $\nu_{dyn}(K\pi)$ for Cu+Cu interactions at $\sqrt{S_{NN}} = 62.4$ GeV scaled with pseudorapidity density ($dN/d\eta$) for K/π , K^+/π^+ , K^-/π^- , K^+/π^- , K^-/π^+ as a function of pseudorapidity density ($dN/d\eta$).

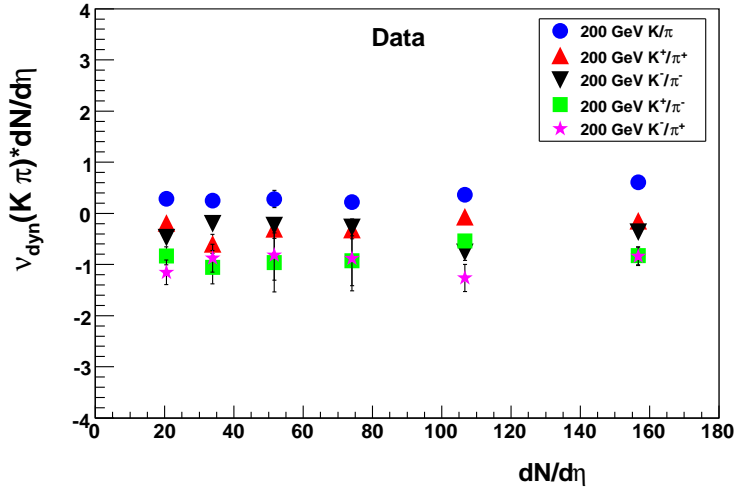


Figure 4.20: Measured dynamical K/π fluctuations in terms of $\nu_{dyn}(K\pi)$ for Cu+Cu interactions at $\sqrt{S_{NN}} = 200$ GeV scaled with pseudorapidity density ($dN/d\eta$) for K/π , K^+/π^+ , K^-/π^- , K^+/π^- , K^-/π^+ as a function of pseudorapidity density ($dN/d\eta$).

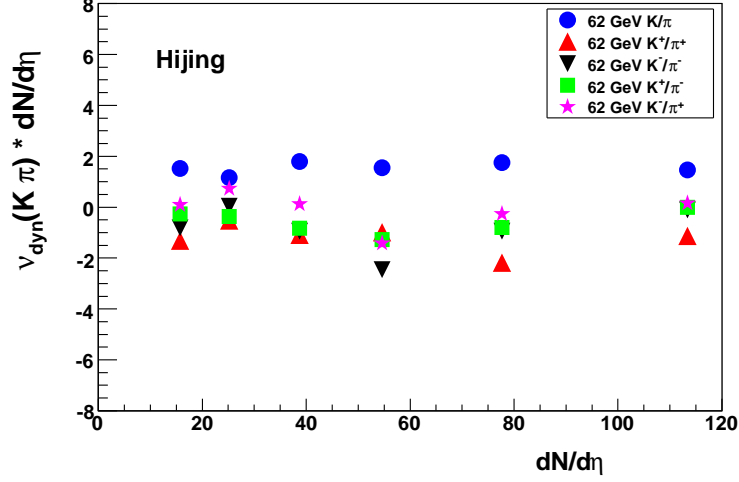


Figure 4.21: Measured dynamical K/π fluctuations in terms of $\nu_{dyn}(K\pi)$ for Cu+Cu interactions at $\sqrt{S_{NN}} = 62.4$ GeV scaled with pseudorapidity density ($dN/d\eta$) for K/π K^+/π^+ , K^-/π^- , K^+/π^- , K^-/π^+ as a function of pseudorapidity density ($dN/d\eta$) from theoretical model calculations .

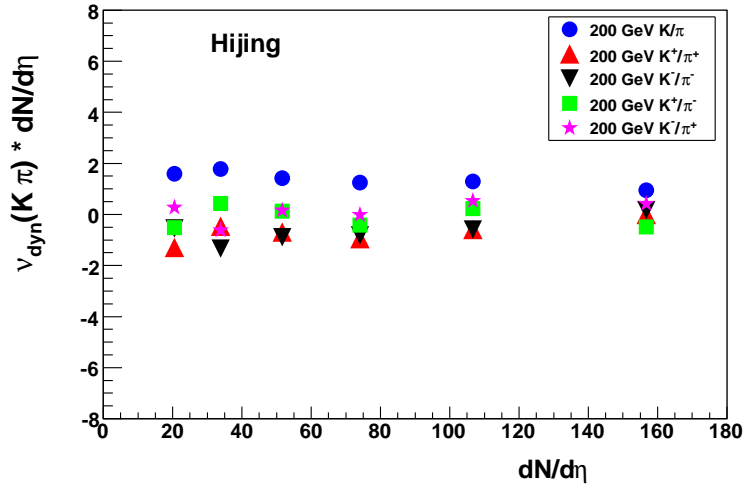


Figure 4.22: Measured dynamical K/π fluctuations in terms of $\nu_{dyn}(K\pi)$ for Cu+Cu interactions at $\sqrt{S_{NN}} = 200$ GeV scaled with pseudorapidity density ($dN/d\eta$) for K/π K^+/π^+ , K^-/π^- , K^+/π^- , K^-/π^+ as a function of pseudorapidity density ($dN/d\eta$) from theoretical model calculations .

Bibliography

- [1] L.L.Landau and E.M. Lifshitz, Statistical Physics, Progamon Press, 1958.
- [2] See e.g. E. Laermann, Nucl. Phys. A610 (1996) 1; F. Karsch, Nucl. Phys. A590 (1995) 367.
- [3] Proceedings of Quark Matter'99 Nucl. Phys. A661(1999).(1995) 367.
- [4] E.V. Shuryak, Phys. Lett. B 423, 9 (1998), K. Rajagopal, Nucl. Phys. A661, 150 C (1999), M. Asakawa, U. Heinz, and B. Muller, Phys. Rev. Lett. 85, 2072 (2000).
- [5] Afanasiev S V et al 2001 Phys. Rev. Lett.86 1965.
- [6] C. Roland, (for the NA49 Collaboration), J.Phys. G: Nucl. Part. Phys. 30 (2004) S1381-S1384.
- [7] C. Roland, (for the NA49 Collaboration), J.Phys. G: Nucl. Part. Phys. 31 (2005) S1075-S1078.
- [8] Jeon S and Koch V 1999 Phys. Rev. Lett.83 5435.
- [9] C. Blume (NA49 Collaboration), hep-ph/0505137 (2005).
- [10] M. Gazdzicki (NA49 collaboration), J. Phys. G: Nucl. Part. Phys. Lett. B 585, 237 (2004).
- [11] P. Seyboth (NA49 collaboration), Acta Phys. Hung. A 25, 259 (2006).

- [12] M. Gazdzicki (NA49 collaboration), nucl-ex/0612007 (2007).
- [13] Stephanov M, Rajagopal K and Shuryak E 1998 Phys. Rev. Lett. 81, 4816.
- [14] J.I. Kapusta, A. Mekjian, Univ. of Minnesota Supercomputer Inst. preprint 85/8 (1985), and Phys. Rev. D33 (1986) 1304.
- [15] F. Becattini, private communication.
- [16] R. Stock, Proceedings of a NATO Advanced Research Workshop on Hot Hadronic Matter: Theory and Experiment, 1994, Divonne, France.
- [17] arXiv:nucl-ex/0301015 v1, 2003.
- [18] C. Pruneau, S. Gavin and S. Voloshin Phys. Rev. C.66, 044904 (2002).
- [19] Z. Ahammed (STAR Collaboration); STAR's Measurement of Energy and System Size Dependence of K/π Fluctuations at RHIC; Quark Matter 2008, Jaipur, India.
- [20] S. Das (STAR Collaboration); Event-by-Event Fluctuation in K/π ratio at RHIC; SQM, March 2006, UCLA, USA.
- [21] S. Das (STAR Collaboration); Strangeness Fluctuations at RHIC; Quark Matter 2006, Shengai, China.
- [22] Giorgio Torrieri, nucl-th/0702062 (2007).
- [23] Voloshin S 2002 Proc. International Nuclear Physics Conference 610 591.
- [24] L. Foa, Phys. Rep., Phys. Lett. 22, 1 (1975).
- [25] J. Whitmore, Phys. Rep., Phys. Lett. 27, 187 (1976).
- [26] H. Boggild and T. Ferbel, Annu. Rev. Nucl. Sci. 24. 451 (1974).
- [27] J. Adams et al (STAR Collaboration), Phys. Rev. C68, 044905 (2003).

[28] X. N. Wang and M. Gyulassy, version 1.38 Phys. Rev. D44, 3501 (1991).

[29] B. Zhang, C. M. Ko, B. A. Li, and Z. Lin, Phys. Rev. C 61, 067901 (2000).

Chapter 5

Photon Multiplicity Distributions in Forward Rapidity Region

5.1 Introduction

In the last two decades the rapid growth of interest in the study of ultra-relativistic heavy-ion collisions has resulted from the motivation that hadronic matter may undergo a phase transition to Quark-Gluon Plasma (QGP) if the energy density attained in the collision zone is sufficiently high [1, 2]. For creating and studying such a new state of matter in the laboratory various experiments were undertaken worldwide at various energies. The energy density can be estimated from the measurement of the transverse momentum (P_t) of produced particles [3]. Multiplicity and pseudorapidity (η) distributions of neutral and charged particles produced in ultra-relativistic heavy-ion collisions also provide important information on the geometry and the dynamics of the collision [1, 2]. Understanding the effects of geometry in terms of the basic nucleon-nucleon and nucleon-nucleus processes is crucial to the isolation of collective effects which might be responsible for the phase transition. Also detailed study of pseudorapidity distributions is necessary to study fluctuations, flow [4], intermittency effects and other special event

characteristics supposedly accompanying the phase transition [5, 6].

Measurement of photon multiplicity have also become increasingly important because of the recent interest in simultaneous measurements of the multiplicity of photons and charged particles in the search for Disoriented Chiral Condensates (DCC) [7, 8]. The formation of a DCC is expected to give rise to large fluctuations in the relative number of emitted neutral particles like photon and charged particles. Also important information about multiparticle production and the evolution of the system formed in the collision can be obtained from the measurements of multiplicity and pseudorapidity distribution of the photons. Multiplicity distributions have been used to understand the particle production mechanism based on participant scaling, two component model [9] and recently by invoking the Color Glass Condensate (CGC) [10] model.

Photons are considered as one of the most valuable probes of the dynamics and properties of the matter formed in the relativistic heavy-ion collisions as they interact only electromagnetically [11, 12]. Photons, being electromagnetic signal, emerges from the fireball with almost no interactions with the other particles produced. This property of photons may provide us information from all the stages of the collisions. The multiplicity and spatial distribution of photons can be used to extract the information about characteristics of the system. Also photons have a large mean free path and hence carry the first hand information of their origin. There are predictions of more direct photon production specifically associated to QGP formation in the heavy-ion collisions [13]. Of all the photons produced in relativistic heavy-ion collisions that one measures experimentally a large part comes from the background sources e.g. hadronic decays like neutral pion ($\pi^0 \rightarrow 2\gamma$), ($\eta \rightarrow 2\gamma$) and ($\eta \rightarrow \pi^0$). The systematic study of pseudorapidity distributions of photons are used in validating the theoretical models attempting to

describe the conditions in the early state of the collision [14, 15].

5.2 Some Earlier measurements

An extensive program on experimentation has been undertaken at the Relativistic Heavy-Ion Collider (RHIC) at Brookhaven National Laboratory (BNL), New York, USA and at Super Proton Synchrotron (SPS), CERN, Geneva with different species at different energies to study the nuclear matter under extreme conditions, in which hadronic matter is expected to undergo a phase transition to a new state of matter, Quark-Gluon Plasma (QGP) [16].

The multiplicity of photons that come mostly from the decay of π^0 are complementary to the charged pion measurements. Extensive results on the analysis of measurements of charged particles produced in heavy-ion collisions covering complete pseudorapidity region has been reported in recent literature [17, 18] but due to the difficulties in precise measurements very limited information is available on photons production [12, 19] in such collisions at forward rapidity region.

The forward rapidity region where the presents analysis on photon multiplicity measurements have been carried out, constitutes an environment which precludes the use of a calorimeter because of enormous overlap of fully developed showers. Measurements of photon multiplicity distribution in the forward rapidity region reported by WA93 and WA98 collaboration in the preshower detector [20] at the Super Proton Synchrotron (SPS) energies, resulting in the study of various aspects of the reaction mechanism in heavy-ion collisions [12, 19, 21].

Recently STAR collaboration at Relativistic Heavy-Ion Collider (RHIC) has reported measurements of the photon pseudorapidity distributions in the forward rapidity region ($2.3 \leq \eta \leq 3.7$) in Au+Au collisions at $\sqrt{S_{NN}} = 62.4$ GeV by using preshower Photon Multiplicity Detector (PMD) [15, 22]. Experimental photon pseudorapidity distributions are observed to be systematically lower than HIJING predictions at mid-central and peripheral events. It is observed that the total number of photons produced per participant pair stays independent of the centrality of collisions.

Further it is observed that the number of charged particles produced per participant pair as a function of $\eta - Y_{beam}$, (where Y_{beam} is the beam rapidity) is independent of beam energy [15, 18]. This phenomenon is known as limiting fragmentation (LF) [23]. There have been contradictory results reported from inclusive charged particle measurements regarding the centrality dependence of the limiting fragmentation behaviour, results from PHOBOS [18] experiment, show a centrality dependence while BRAHMS [17] and STAR [15, 22] experiment observed centrality independent behaviour. The total photon yield scales with the number of participating nucleons and follow longitudinal pseudorapidity scaling away from the mid-rapidity which is independent of energy. Limiting Fragmentation (LF) hypothesis [23] is used to explain this, but recently Color Glass Condensate [10] is also used to understand the effect at forward rapidities. There is therefore a strong case for undertaking comprehensive analysis on photon production to have conclusive inferences on the physics issues.

In this chapter measurements on photon multiplicity distributions in the forward rapidity ($2.3 \leq \eta \leq 3.8$) region and their fluctuations are reported. The data is obtained using highly granular preshower Photon Multiplicity Detector (PMD) [24] for Cu+Cu interactions at $\sqrt{S_{NN}} = 62.4$ GeV. These studies have been carried out for different

collision centralities. Experimental results have been compared with HIJING (version 1.38) event generator [25] modelled to the geometrical environment of the detector.

5.3 Preshower Configuration During Data Taking

As we described in chapter three, that preshower plane of the Photon Multiplicity Detector (PMD) contains 12 supermodules (SMs, numbering from 13-24) with 24 FEE chains (numbering from 25-48). Figure 5.1 shows the preshower plane view from tunnel, numbering and layout of the supermodules (SMs) and FEE chains used during RHIC Run V. During the Run V the operating voltage of the detector was at -1400 Volts, except SM 24. The SM 24 was operated at -1350 Volts. Also some area of the preshower plane was not working during data taking because some FEE chains boards were kept off from operation due to their high electronics noise and other functional problems.

5.4 Data Set Selection for Analysis

For the present studies we use data set recorded by Photon Multiplicity Detector (PMD) in STAR experiment for Cu+Cu interactions at $\sqrt{S_{NN}} = 62.4$ GeV taken in the year 2005. Most of the data run numbers selected from day 78. Only those data run numbers are included in the analysis in which maximum number of cells are working in the preshower plane. Approximately two million minimum bias events are used for the present studies which was obtained by coincidence between two Zero Degree Calorimeters (ZDCs) and a minimum signal from Central Trigger Barrel (CTB). Only those events are selected which were produced within ± 50 cm of the center of the Time Projection Chamber (TPC) along the beam axis. The centrality determination of this analysis uses

PMD – Preshower Plane – 2005
View from Tunnel

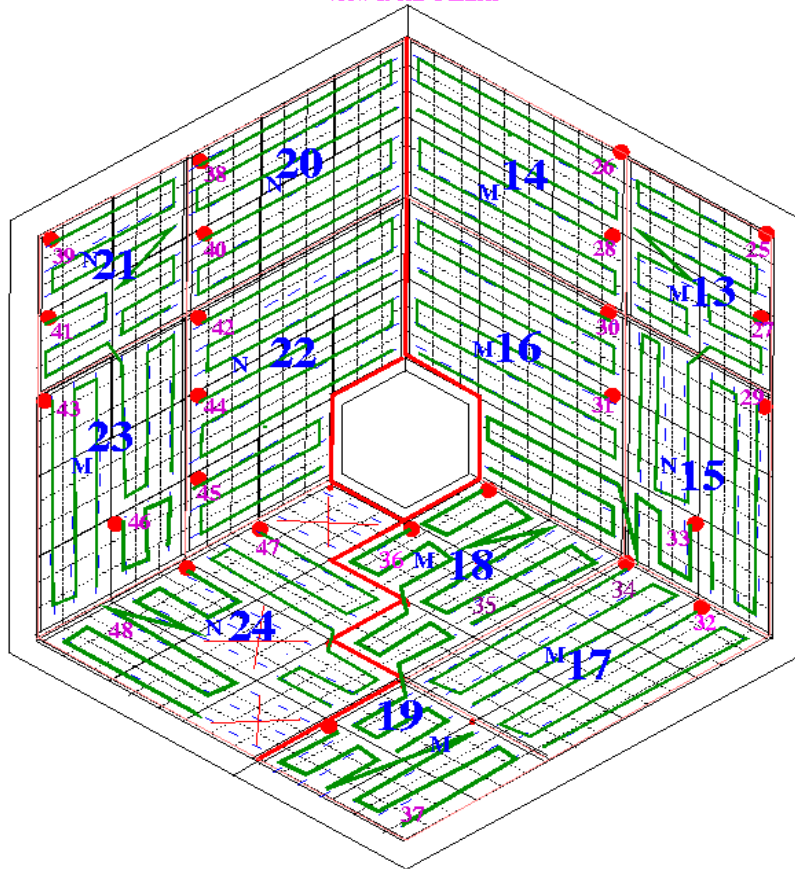


Figure 5.1: Schematic view of preshower plane, numbering and layout of the Supermodules (13-24) and FEE chains (25-48) during RHIC Run V.

the multiplicity of charged particles in the pseudorapidity $|\eta| < 0.5$, as measured by Time Projection Chamber (TPC).

5.5 Discrimination and Gain Calibration

Photon Multiplicity Detector (PMD) is a highly segmented gaseous detector on a plane placed behind a lead converter plate of 3 radiation length ($3\times_0$) [24]. In order to reject the charged particles another plane called veto is placed in front of the lead converter. Each planes are further sub-divided into 12 gas tight entities, known as supermodules (SMs). Discrimination between photons and charged hadrons is done by their difference in response e.g., charged hadrons affect mostly one cell with Minimum Ionising Particle (MIP) like energy deposition, whereas the number of cells affected and signal from photon are large. The uniformity of the detector is obtained by finding MIP-response from each cell. MIP response of each cell is obtained by selecting cells having a signal surrounded by six cells without any signal representing an isolated cell. Figure 5.2 shows the ADC distribution of an isolated cell fitted with Landau distribution.

For uniform response of the detector cell to cell gain calibration is done. The relative gain for each cell is computed by dividing the cell ADC mean by the average mean of all cells in a supermodule. Figure 5.3 shows a typical cell to cell gain distribution for one supermodule of the preshower plane.

After gain calibration, the number of photons in an event are counted by finding clusters from cells with non-zero signal and applying a suitable cut on the cluster signal and number of cells to reject charged hadrons. Following criteria is evolved to select photon like clusters ($N_{\gamma-like}$) using the HIJING Monte Carlo event generator [25] and

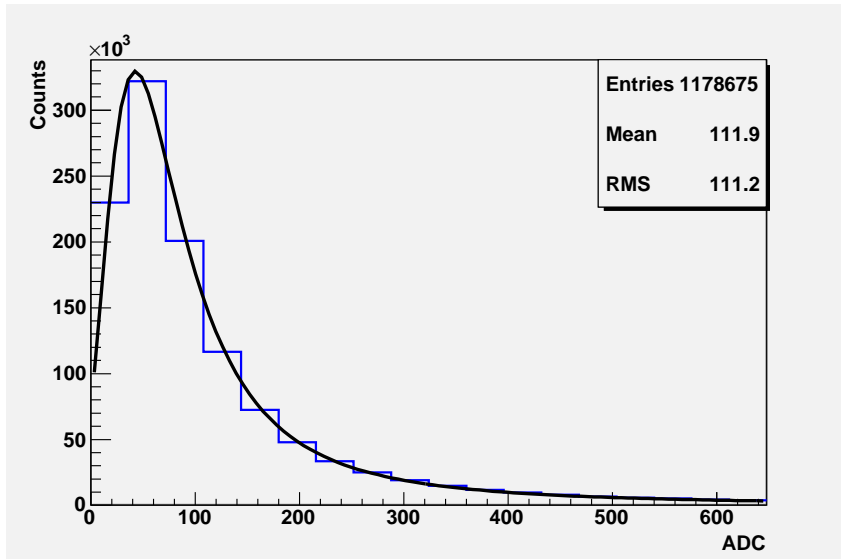


Figure 5.2: The isolated cell ADC distribution for one of the supermodule in the preshower plane

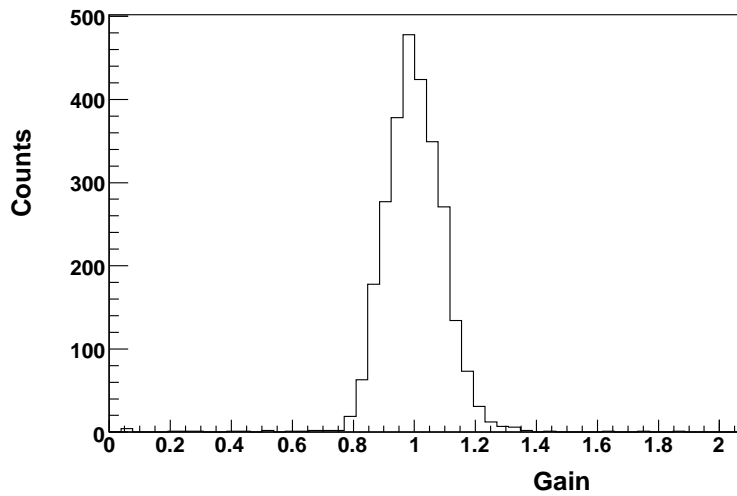


Figure 5.3: The Relative cell to cell gain distribution for one of the supermodule in the preshower plane.

GEANT [26] : (a) the number of hit cells in a cluster >1 and (b) the cluster signal is 3 times or more than the average response of all isolated cells in a supermodule. The choice of the conditions is based on a detailed study of simulations [15, 22, 24]. The number of selected clusters, called γ -like cluster ($N_{\gamma-like}$) in different supermodules of the preshower plane for the same pseudorapidity (η) coverage are used to evaluate the effect of possible non-uniformity in the response of the detector. Similar threshold is also applied in experimental data to count number of photon like clusters event-by-event.

5.6 Efficiency and Purity

Experimental measurements of photon multiplicity (N_γ) depends upon the detection efficiency, purity and geometrical acceptance of the detector. For obtaining photon efficiency (ϵ_γ) and purity (f_p) detailed simulations have been performed by running full GEANT [26] with STAR geometry (GSTAR, SLO5D) using HIJING event generator [25] with default parameter. The physics performance of the detector is characterized in terms of photon counting efficiency (ϵ_γ) and purity (f_p) defined [19] by the following relations:

$$\text{efficiency } (\epsilon_\gamma) = N_{cls}^{\gamma,th} / N_{inc}^\gamma$$

$$\text{purity } (f_p) = N_{cls}^{\gamma,th} / N_{\gamma-like}$$

where N_{inc}^γ is the number of incident photons from the event generator, $N_{cls}^{\gamma,th}$ is the number of photon clusters above the hadron rejection threshold and $N_{\gamma-like}$ is the total number of clusters above the hadron rejection threshold. The optimal value for threshold cut is determined from detailed simulation in terms of MIP energy units. The photon counting efficiency (ϵ_γ) and purity (f_p) depend on the several factors like the conversion probability, criteria applied for hadron rejection threshold, granularity and

the track reconstruction efficiency. Because of the change in particle multiplicity and the energy, these factors also depend on the centrality and pseudorapidity.

Figure 5.4 and 5.5 shows the photon counting efficiency (ϵ_γ) and purity (f_p) respectively extracted from simulated data. Both photon efficiency (ϵ_γ) and purity (f_p) varies with pseudorapidity window. This is due to variations in particle density, upstream material from other STAR detectors, a part of photons may get converted and fall on the PMD as charged particles. In figure 5.4 and 5.5, it is seen that both photon efficiency (ϵ_γ) and purity (f_p) almost consistent with centrality for Cu+Cu interactions at $\sqrt{S_{NN}} = 62.4$ GeV. The observed photon counting efficiency (ϵ_γ) is within the range of 30% to 35% and purity is (f_p) is 55% to 60%. After calculating photon efficiency (ϵ_γ) and purity (f_p) the number of photon (N_γ) from the ($N_{\gamma-like}$) are obtained as:

$$N_\gamma = N_{\gamma-like} * \frac{f_p}{\epsilon_\gamma}$$

5.7 Detector Acceptance Factor

Like efficiency and purity one more important factor called acceptance (i.e. detector acceptance) is necessary to get correct photon multiplicity distributions, because out of the total 41,472 cells in the preshower plane, only 31674 cells were working for the data set used for the present study. Figure 5.6 shows ideal complete working two dimensional picture of preshower plane. But during experiment all the cells of the detector are not working because of several reason, so we need to calculate the geometrical acceptance of the detector. Figure 5.7 shows the actual working cell picture for the data set used for the present analysis. Out of 12 supermodule only seven supermodule are used for the present analysis as the rest of the supermodule had very low gain. The geometrical acceptance factors are obtained pseudorapidity bin wise for the supermodules used in

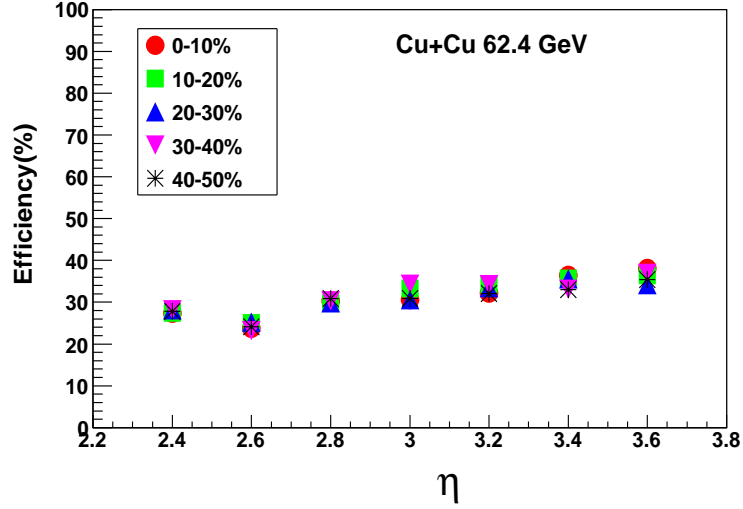


Figure 5.4: Photon reconstructed efficiency (ϵ_γ) as a function of pseudorapidity (η) window for different centrality classes in Cu+Cu interactions at $\sqrt{S_{NN}} = 62.4$ GeV.

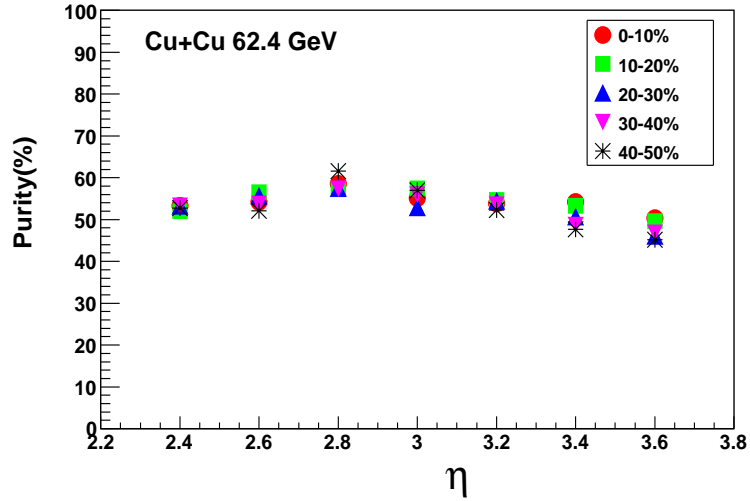


Figure 5.5: Purity (f_p) of Photon sample as a function of pseudorapidity (η) window for different centrality classes in Cu+Cu interactions at $\sqrt{S_{NN}} = 62.4$ GeV.

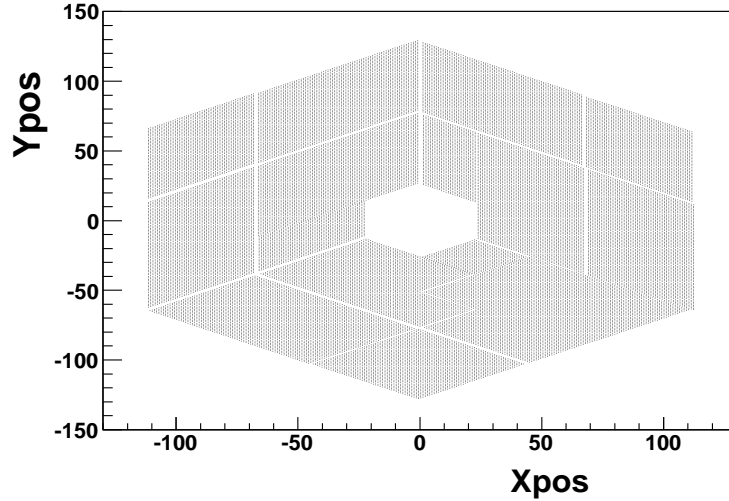


Figure 5.6: **Two dimensional picture of Preshower plane.**

the present analysis. The geometrical acceptance calculated as: total number of cells within the pseudorapidity bin divided by total number of working active cells. In figure 5.8 we plotted acceptance factor for the preshower plane as a function of pseudorapidity (η). The acceptance factor is observed to vary with eta bin. Finally the number of photon (N_γ) from the ($N_{\gamma-like}$) are obtained as:

$$N_\gamma = N_{\gamma-like} * \left(\frac{f_p}{\epsilon_\gamma}\right) * \text{Acceptance}$$

5.8 Photon Multiplicity Distributions

The conventional way of describing particle production in relativistic heavy-ion collisions is by measuring the particle density in pseudorapidity (η). Within the framework of certain model assumptions, it provides information on energy density, initial temperature and velocity of sound in the medium formed in the collisions [3, 27]. The variation of

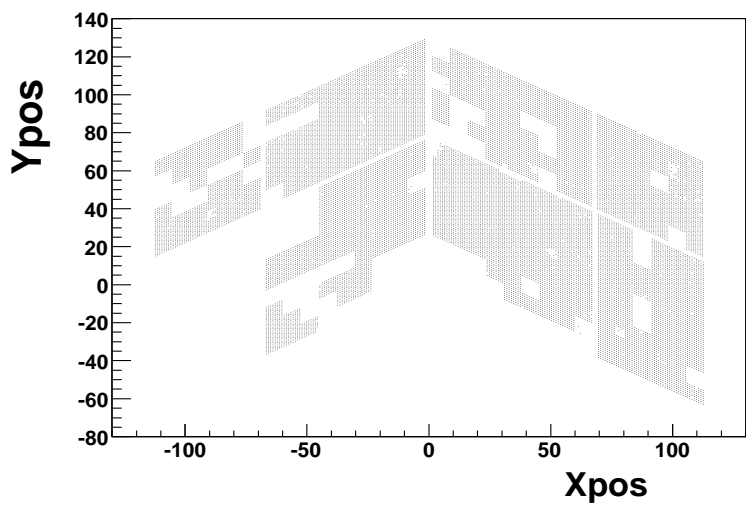


Figure 5.7: Supermodule in preshower plane that used in the present analysis.

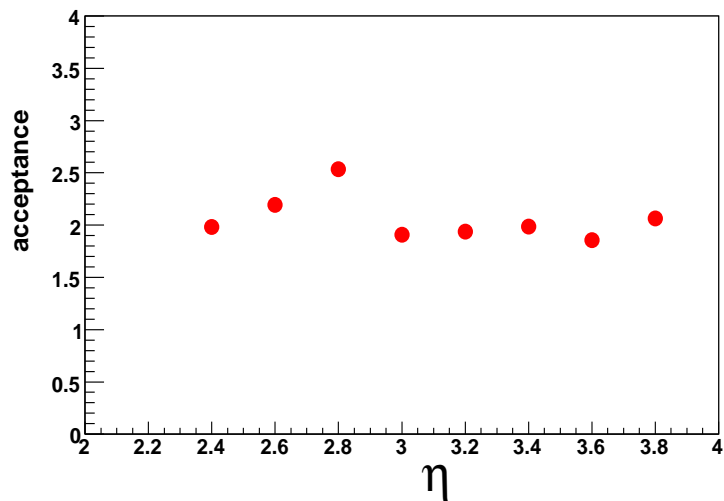


Figure 5.8: Pseudorapidity (η) wise geometrical acceptance factor for the preshower plane.

particle density in pseudorapidity (η) with collision centrality, expressed in terms of the number of participating nucleons (N_{Part}), can shed light on the relative importance of soft versus hard processes in particle production. The particle density in pseudorapidity (η) also provides a test ground for various particle production models, such as those based on ideas of parton saturation [28] and semi-classical QCD, also known as the color glass condensate (CGC) [29]. In the environment of RHIC energies the mechanisms of particle production could not be uniform i.e. it could be different in different regions of pseudorapidity (η). At midrapidity a significant increase in charged particle production normalized to the number of participating nucleons (N_{Part}) has been observed for central Au+Au collisions compared to peripheral Au+Au collisions [30]. This has been attributed to the onset of hard scattering processes, which scale with the number of binary collisions. Alternatively in the scenario of CGC [31], the centrality dependence of particle production at midrapidity reflects the increase of gluon density due to the decrease in the effective strong coupling constant. It will be interesting to see how the photon production scales with the number of participating (N_{Part}) nucleons at forward rapidity.

The Photon Multiplicity Detector (PMD) in STAR experiment [32] at the Relativistic Heavy-Ion Collider (RHIC) at Brookhaven National Laboratory (BNL) has the unique capability of measuring the photon multiplicities in the forward rapidity region. By using this capability we can carry out the study of photon production in Cu+Cu interactions at $\sqrt{S_{NN}} = 62.4$ GeV. The figure 5.9 shows the minimum bias event-by-event photon multiplicity distributions in Cu+Cu interactions at $\sqrt{S_{NN}} = 62.4$ GeV. In figure the open circles correspond to the photons multiplicity (N_γ) for top 10% central events. The solid curve is the Gaussian fit to the data points. The multiplicity distribution have a characteristic shape with a steep rise that corresponds to the most peripheral events.

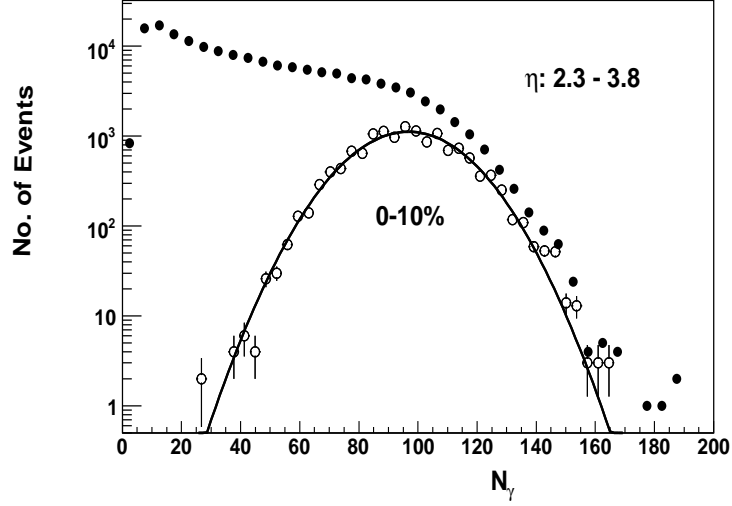


Figure 5.9: Minimum Bias N_γ Multiplicity Distributions for Cu+Cu interactions at $\sqrt{S_{NN}} = 62.4$ GeV. The N_γ multiplicity for top 10% central events are shown in open circles. The solid curve is the Gaussian fit to the data points.

The plateau in the multiplicity distribution correspond to mid-central events and the fall off region reflects the intrinsic fluctuations of the measured quantities and the limited acceptance of the detectors.

5.8.1 Centrality Wise Photon Pseudorapidity Distributions

For different centrality classes, the measured photon pseudorapidity distributions in Cu+Cu interaction at $\sqrt{S_{NN}} = 62.4$ GeV recorded by Photon Multiplicity Detector (PMD) in STAR experiment in the forward rapidity ($2.3 \leq \eta \leq 3.8$) region are plotted in figure 5.10. It is observed that the particle density of photon is found to decrease as we scan pseudorapidity window from $\eta = 2.4$ to $\eta = 3.8$ in steps of $\eta = 0.2$ units. The

effect becomes more pronounced with increase in centrality.

5.8.2 Comparison with Model Predictions (HIJING)

An attempt is made to understand experimental photon pseudorapidity distributions in Cu+Cu interactions at $\sqrt{S_{NN}} = 62.4$ GeV comparison with simulated distributions obtained from theoretical model HIJING [25] trained to experimental environment for different centrality classes. The plot is shown in figure 5.11.

It is observed that comparison with HIJING prediction is not satisfactory. Not only that estimations of pseudorapidity density for photons from model code are consistently lower than experimental values but the extent of disagreement is more pronounced in the η region of $3.2 \leq \eta \leq 3.6$. However, in top central collisions (0-10%) the comparison is reasonably comfortable and becomes worse for peripheral events. The observations in current experiment are consistent to the results from Au+Au collisions at $\sqrt{S_{NN}} = 62.4$ GeV already reported by STAR collaboration [15, 22].

The indicated errors on the distribution are systematic. The systematic errors on the photon pseudorapidity distributions ($dN_\gamma/d\eta$) are due to (i) uncertainty in estimates of efficiency (ϵ_γ) and purity (f_p) values, arising from splitting of clusters and the choice of photon-hadron discrimination conditions (ii) uncertainty in N_γ arising from the non-uniformity of the detector primarily due to cell-to-cell gain variation. The errors found to be $\sim 14\%$ for central and $\sim 15.3\%$ for peripheral collisions respectively. The total errors are obtained by adding systematic and statistical errors in quadrature. Because of large statistics, the statistical errors are very small.

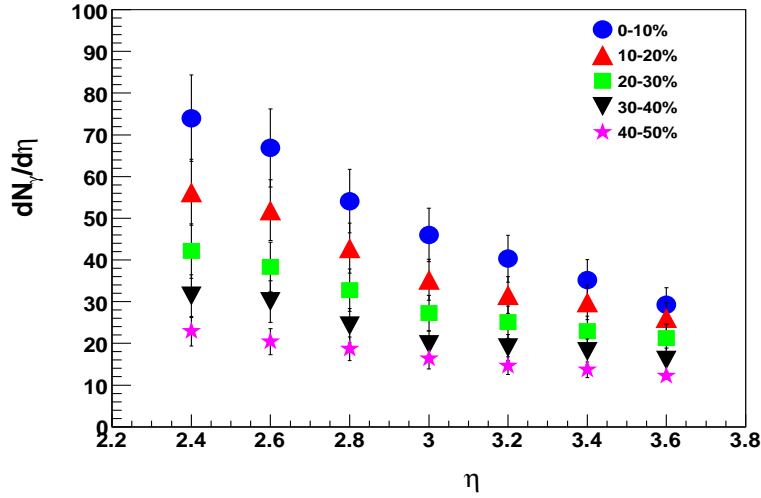


Figure 5.10: Experimental measured photon pseudorapidity ($dN_\gamma/d\eta$) distributions for different centrality classes as a function of pseudorapidity (η).

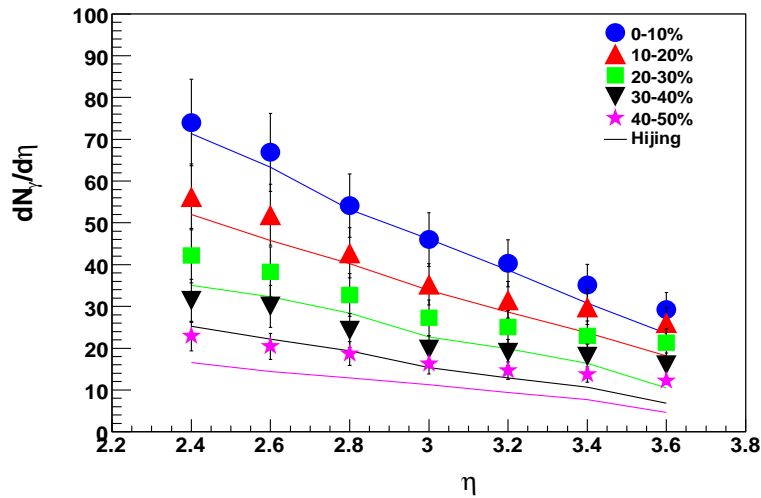


Figure 5.11: Comparison of experimental measured photon pseudorapidity ($dN_\gamma/d\eta$) distributions for different centrality classes as a function of pseudorapidity (η) with HIJING predictions.

5.8.3 Photon Production as a function of N_{Part}

The experimental data on photon multiplicity is analysed in terms of collision centrality expressed in terms of number of participating nucleons (N_{Part}). In figure 5.12, the variation of total number of photons normalized to the number per participant pair in the pseudorapidity (η) coverage ($2.3 \leq \eta \leq 3.8$) in Cu+Cu interactions at $\sqrt{S_{NN}} = 62.4$ GeV is plotted as a function of number of participant nucleons (N_{part}). The measured distributions are scaled by number of participant nucleons to remove the effect of the different number of nucleons participating in collisions with different centralities. The number of participant nucleons (N_{part}) are obtained from HIJING for appropriate centrality classes. Higher values of N_{part} corresponds to more central collisions, or collision with small impact parameter. The data is compared with predictions from HIJING. It is observed that the variations in photon multiplicity per participant pair is consistent with model predictions only for top centrality (0-10%) data. The incompatibility of data with model predictions increases with increase in impact parameter.

In figure 5.13, photons pseudorapidity distributions per participant pair $(dN_\gamma/d\eta)/0.5 * N_{part}$ as a function of pseudorapidity (η) are plotted for different centrality classes and compared with HIJING model predictions. It is observed that photon yield normalized to the number of participating nucleons (N_{part}), as a function of pseudorapidity (η) is independent of centrality and similar trend is seen in HIJING but agreement is quantitatively poor.

5.8.4 Limiting Fragmentation in Photon Production

The particle production in heavy-ion collisions at high energy is observed to be associated with smaller transverse momenta of the produced particles compared to the beam

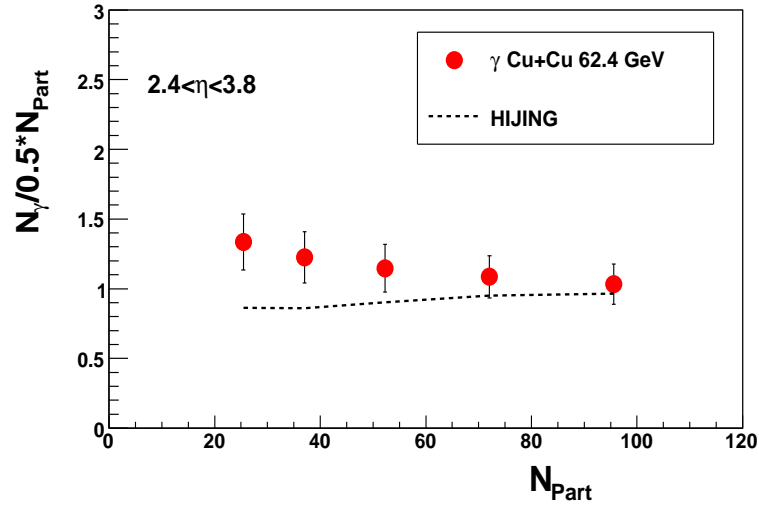


Figure 5.12: Measured variation in N_γ per participant pair as a function of number of participant nucleons (N_{part}) and their comparison with HIJING.

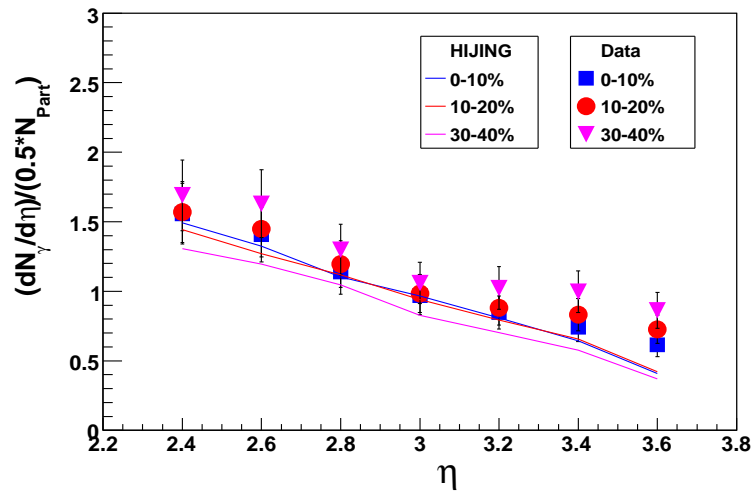


Figure 5.13: Photon pseudorapidity distributions per participant pair, $(dN_\gamma/d\eta)/0.5 * N_{part}$ for different centrality classes as a function of η and their comparison with HIJING predictions.

momentum. The colliding particles in a collider have large longitudinal momenta. These breaks apart in the collision process, producing particles, some of which carry a large longitudinal momentum. These outgoing particles would prefer to travel in the beam momentum direction. The produced particle distribution when plotted as a function of $Y - Y_{beam}$, where Y_{beam} is the beam rapidity, for various center-of-mass energies approach limiting distributions. This intuitive picture of a high energy heavy-ion collision process has two extended objects going through each other, breaking into fragments in the process, is described within the framework of a hypothesis of Limiting Fragmentation [33, 34].

In the present analysis an attempt has been made to study the limiting fragmentation behaviour for photon production in Cu+Cu interactions at $\sqrt{S_{NN}} = 62.4$ GeV collected by PMD in STAR experiment. Photon pseudorapidity distribution scaled to the number of participating nucleons (N_{part}) as a function of $\eta - Y_{beam}$ for central (0-10%) Cu+Cu interactions at $\sqrt{S_{NN}} = 62.4$ GeV is plotted in figure 5.14.

Energy and system size dependence of the particle production is investigated by comparing the results with photon data from central (0-5%) Au+Au interactions [15] at $\sqrt{S_{NN}} = 62.4$ GeV, central (0-10%) Cu+Cu interactions [35, 36] at $\sqrt{S_{NN}} = 200$ GeV, central Pb+Pb interactions at 17.3 A GeV in WA98 experiment [19] and the UA5 [37] data for $p\bar{p}$ at 540 A GeV.

It is observed from figure 5.14 that photon production from Pb+Pb interactions in WA98 experiment at SPS and in Au+Au, Cu+Cu interactions in STAR experiment at RHIC are consistent with each other, suggesting that photon production follows an energy as well as system independent limiting fragmentation behaviour.

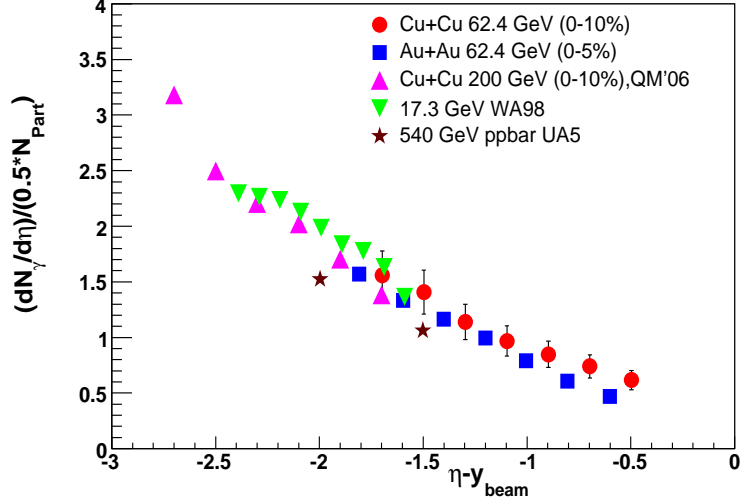


Figure 5.14: Measured photon pseudorapidity distributions scaled to number of participant nucleons $((dN_\gamma/d\eta)/(0.5*N_{part}))$ as a function of $\eta - Y_{beam}$.

5.8.5 Fluctuations in Photon Production

The event-by-event measurements of photon production in heavy-ion collisions can be used to study multiplicity fluctuations [21]. Fluctuations in physical observables in heavy-ion collisions may provide important information regarding the deconfined state of quarks and gluons and also help to address the question of thermalization [38]. One of the main advantage of heavy-ion collisions at higher energies is a large multiplicity of produced particles enabling the studies observables on an event-by-event basis. Event-by-event analysis has an added advantage as it can unmask the signals of fluctuations which can otherwise get lost in the normal processes of averaging in data [39, 40].

Various methods have been proposed to study event-by-event fluctuations in various

global observables [41, 42]. Here sub-event method [43] is used to gauge the strength of dynamical fluctuations in photon production by using the variable ν_{dyn} [44] in Cu+Cu interactions at $\sqrt{S_{NN}} = 62.4$ GeV collected by Photon Multiplicity Detector (PMD) in STAR experiment. It is useful in collecting fluctuations which affect the entire event.

The sub-event method permits one to avoid some problem of the “direct” computation of the event-by-event fluctuations. In particular the problems related to the separation of the event-by-event fluctuations from dynamical effects, such as Bose-Einstein correlations (the HBT effects). It is not possible to avoid the HBT correlations in the direct approach and one can only perform a rather complicated estimate of its contribution [45]. In the sub-event method [43] one can define the sub-events on different regions, so that particles from two regions are not correlated and the problem simply disappears. For example one can define sub-events on rapidity regions separated by 0.2 unit of rapidity. The same trick can be used to get rid of the two track resolution problem which is quite serious problem in many experiments.

To get the strength of dynamical fluctuations by using the concept of sub-event method in photon production as a two particle correlation, we can divide pseudorapidity window (η) shown in figure 5.15 into two different regions. The photon multiplicity falls in the pseudorapidity (η) range of $-2.8 \leq \eta \leq -3.18$ consider as γ_1 and those falls in the pseudorapidity (η) range of $-3.22 \leq \eta \leq -3.6$ consider as γ_2 .

In terms of γ_1 and γ_2 we can rewrite the equation 4.5 in chapter four, page 127 as:

$$\nu_{dyn}(\gamma_1, \gamma_2) = \frac{\langle N_{\gamma_1}(N_{\gamma_1}-1) \rangle}{\langle N_{\gamma_1} \rangle^2} + \frac{\langle N_{\gamma_2}(N_{\gamma_2}-1) \rangle}{\langle N_{\gamma_2} \rangle^2} - 2 \frac{\langle N_{\gamma_1} N_{\gamma_2} \rangle}{\langle N_{\gamma_1} \rangle \langle N_{\gamma_2} \rangle}$$

By making use of above equation, we calculated dynamical fluctuations in terms of $\nu_{dyn}(\gamma_1, \gamma_2)$ variable. In figure 5.16 and 5.17, experimentally calculated values of $\nu_{dyn}(\gamma_1, \gamma_2)$ is plotted as a function of pseudorapidity density ($dN/d\eta$) and number of participant nucleons (N_{part}) respectively. The observed behaviour of data is compared with data from HIJING model predictions. It is observed that the dynamical fluctuations measured by $\nu_{dyn}(\gamma_1, \gamma_2)$ is inversely proportional to rapidity density ($dN/d\eta$), and number of participant nucleons (N_{part}), indicating that the fluctuation strength gets diluted in high multiplicity environment. It is also observed that model predictions (HIJING) reproduces the experimental data in high multiplicity events only.

An attempt has also been made to see the scaled behaviour of observed dynamical fluctuation strength. In figure 5.18 is plotted scaled $\nu_{dyn}(\gamma_1, \gamma_2) * dN/d\eta$ as a function of pseudorapidity density ($dN/d\eta$). It is observed that the scaled fluctuations increase with increase in pseudorapidity density quickly, and saturate at higher pseudorapidity density.

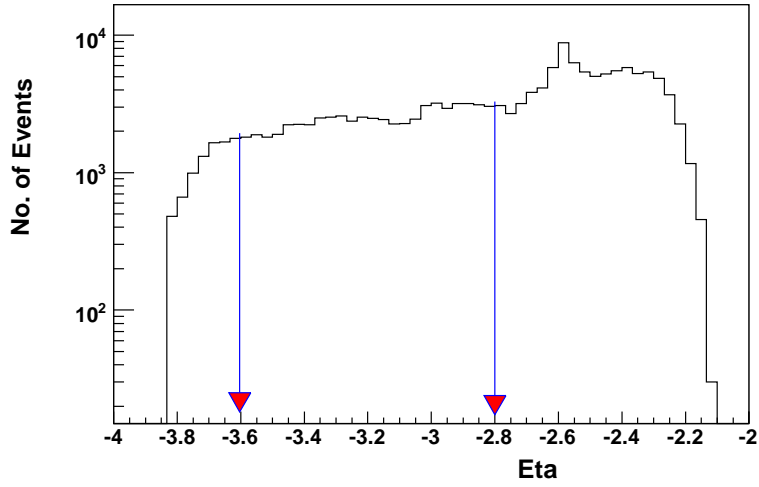


Figure 5.15: Pseudorapidity (η) distribution recorded by Photon Multiplicity Detector (PMD) for Cu+Cu interactions at $\sqrt{S_{NN}} = 62.4$ GeV.

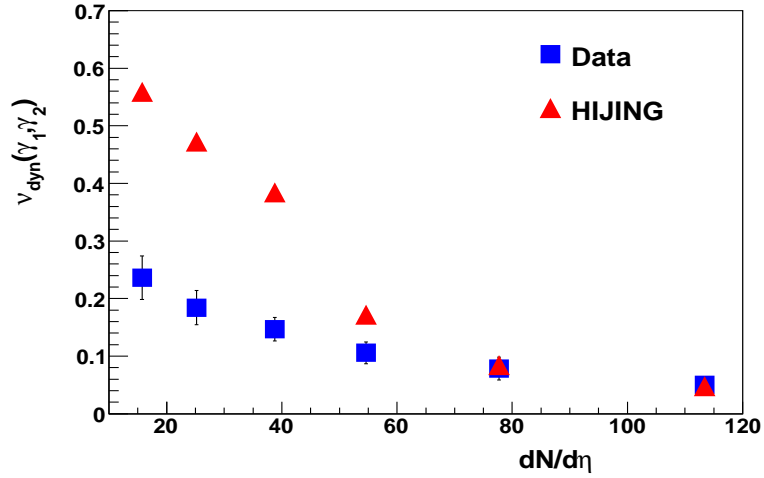


Figure 5.16: $\nu_{dyn}(\gamma_1, \gamma_2)$ as a function of pseudorapidity density ($dN/d\eta$) for Cu+Cu interactions at $\sqrt{S_{NN}} = 62.4$ GeV compared with HIJING model predictions.

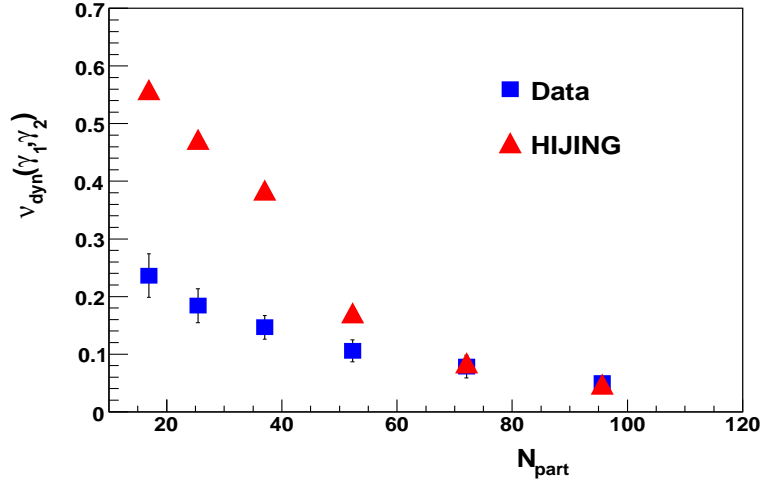


Figure 5.17: $\nu_{dyn}(\gamma_1, \gamma_2)$ as a function of number of participant nucleons (N_{part}) for Cu+Cu interactions at $\sqrt{S_{NN}} = 62.4$ GeV compared with HIJING model predictions.

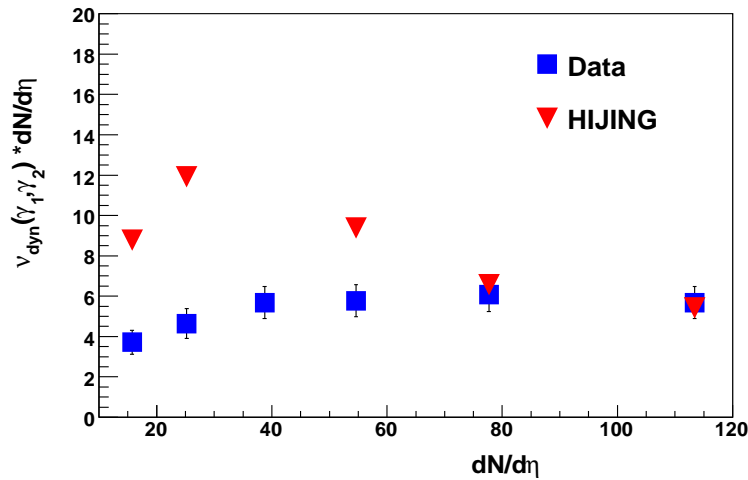


Figure 5.18: Scaled $\nu_{dyn}(\gamma_1, \gamma_2)$ with pseudorapidity density ($dN/d\eta$) as a function of number of $dN/d\eta$ for Cu+Cu interactions at $\sqrt{S_{NN}} = 62.4$ GeV compared with HIJING model predictions.

Bibliography

- [1] J. Schukraft and H.R. Schmidt, J. Phys. G 19, 1705 1993 ; J.Stachel and G.R. Young, Annu. Rev. Nucl. Part. Sci. 44, 537 1994 ; M.J. Tannenbaum, Int. J. Mod. Phys. A 4, 3377 1989 .
- [2] M.M. Aggarwal and S. I. A. Garpman, Int. J. Mod. Phys. E 4,477 1995 .
- [3] J.D. Bjorken, Phys. Rev. D 27, 140 1983 .
- [4] M.M. Aggarwal et al., WA93 Collaboration, Phys. Lett. B403 (1997) 390.
- [5] A. Bialas and R. Peschanski, Nucl. Phys. B273, 703 1986 .
- [6] A. C. Das and Y. P. Viyogi, Phys. Lett. B 380, 437 1996 ; S.K. Nayak and Y.P. Viyogi, ibid. 367, 386 1996 .
- [7] J.D. Bjorken, K.L. Kowalski, C.C. Taylor, Baked Alaska,SLAC-PUB-6109, 1993 and hep-ph/9309235; K. Rajagopal,F. Wilczek, Nucl. Phys. B 399 Z1993. 395.
- [8] M.M. Aggarwal et al., WA98 Collaboration, Phys. Lett. B 420 1998. 169; T.K. Nayak et al., WA98 Collaboration,Z Nucl. Phys. A 638 1998. 249c.
- [9] M.Biyajima et al., Phys. Rev. Lett. B 515 (2001) 470-476.
- [10] J.J.Marian, J. Phys. G,30 (2004) S751-S758.

- [11] R.C. Hwa and K. Kajanti, Phys. Rev. D32 (1985) 1109; B. Sinha, Physica Scripta T32 (1990) 1847.
- [12] M.M. Aggarwal et al., (WA93 Collaboration), Phys.Rev. C 58, 1146 (1998); Phys. Lett. B 403, 390 (1997); M.M. Aggarwal et al., (WA98 Collaboration), Phys. Rev. C 64, 011901(R) (2001).
- [13] M.M. Aggarwal et al., (WA98 Collaboration), Phys. Rev. Lett. 85 (2000) 3595
- [14] K.J. Eskola Nucl. Phys. A698 (2002) 78c.
- [15] J. Adams et al., (STAR Collaboration) Phys. Rev. Lett. 95 (2005) 062301.
- [16] Proceeding of Quark Matter 2004 (Jour. of Phys. G 30(2004)).
- [17] I.G.Bearden et al., (BRAHMS Collaboration), Phys. Rev. Lett. 88 (2002) 202301, Phys. Lett. B 523 (2001) 227.
- [18] B.B. Back et al., (PHOBOS Collaboration), Phys. Rev. Lett. 91(2003) 052303, Phys. Rev. Lett. 87 (2001) 102303, Nucl. Phys. A757 (2005) 28.
- [19] M.M. Aggarwal et al., (WA98 Collaboration), Phys. Lett. B 458, 422 (1999).
- [20] M.M.Aggarwal et al., Nucl. Instr. and Meth. A 372, 143 (1996); Nucl. Instr. and Meth. A 424, 395 (1999).
- [21] M.M. Aggarwal et al., (WA98 Collaboration), Phys. Rev. C. 65 (2002) 054912.
- [22] J. Adams et al., (STAR Collaboration) Phys. Rev. C. 73 (2006) 034906.
- [23] J. Benecke et al., Phys. Rev. 188, 2159 (1969); R. Beckmann, S. Raha, N.Stelte and R.M. Weiner, Phys. Lett. B 105, 411 (1981).
- [24] M.M. Aggarwal et al.,Nucl. Instr. Meth. A 499, 751(2003); Nucl. Instr. Meth. A 488, 131 (2002).

- [25] X-N. Wang and M. Gyulassy, Phys. Rev. D 44, 3501 (1991).
- [26] V. Fine and P. Nevski, in proceeding of CHEP-2000, Padova, Italy.
- [27] L. D. Landau, Izv. Akad. Nauk Ser. Fiz. 17, 51(1953); S. Belenkij and L. D. Landau, Usp. Fiz. Nauk. 56, 309 (1955); Nuovo Cim. Suppl. 3S10, 15 (1956); R. C. Hwa and K. Kajantie, Phys. Rev. D32, 1109 (1985); J. Alam et al., Annals of Phys. 286, 159 (2000); B. Mohanty and J. Alam, Phys. Rev. C 68, 064903 (2003).
- [28] L. V. Gribov, E. M. Levin and M. G. Ryskin, Phys. Rep. 100, 1 (1983); J. P. Blaizot and A. H. Mueller, Nucl. Phys. B 289, 847 (1987).
- [29] L. McLerran and R. Venugopalan, Phys. Rev. D49, 2233 (1994); L. McLerran and R. Venugopalan, Phys. Rev. D 50, 2225 (1994); Y. V. Kovchegov, Phys. Rev. D 54, 5463 (1996); E. Iancu and L. McLerran, Phys. Lett. B 510, 145 (2001); A. Krasnitz and R. Venugopalan, Phys. Rev. Lett.84, 4309 (2000).
- [30] K. Adcox et al., (PHENIX Collaboration), Phys. Rev. Lett. 86, 3500 (2001).
- [31] D. Kharzeev and Marzia Nardi, Phys.Lett. B 507, 121, (2001); E. Iancu, A. Leonidov and L. McLerran, hep-ph/0202270.
- [32] K.H. Ackermann et al., Nucl. Instr. Meth. A 499, 624 (2003).
- [33] J. Benecke and T. T. Chou, C. N. Yang and E. Yen, Phys. Rev. 188 (1969) 2159.
- [34] R. Beckmann, S. Raha, N. Stelte and R. M. Weiner, Phys. Lett. B 105, (1981).
- [35] M. Sharma, N.Gupta , S.M. Dogra ,Int. Journal of Mod. Phys. E. Vol. 16, Nos.7 and 8 (2007) 1845-1851.
- [36] M. Sharma, N. Gupta, S.M. Dogra, Proceeding of Quark Matter, Shanghai, China, 2006.

- [37] K. Alpgard et al., (UA5 Collaboration), Phys. Lett. B 115 (1982) 71; G.J. Alner et al., Z. Phys. C 33 (1986) 1.
- [38] H. Heiselberg, Phys. Rep. 351, (2001) 161.
- [39] E.V. Shuryak, Phys. Lett. B 423, 9 (1998).
- [40] K.Rajagopal, Nucl. Phys. A 661, 150c (1999).
- [41] M.Stephanov, K. Rajagopal and E. Shuryak, Phys. Rev. Lett. 81, 4816 (1998); Phys. Rev. D61, 114028 (1999).
- [42] S. Jeon and V. Koch Phys. Rev. Lett. 83, 5435 (1999); Phys. Rev. Lett. 85, 2076 (2000).
- [43] S.A. Voloshin, V. Koch, H.G. Ritter, Phys. Rev. C60, 024901,(1999).
- [44] J.Adams et al.,(STAR Collaboration), Phys. Rev. C68, 044905 (2003).
- [45] G. Roland for the NA49 Collaboration, Nucl. Phys. A 638 (1998) 91c; H. Appelshauser et al., NA49 Collaboration, to be published.

Chapter 6

Conclusions

The present thesis comprised of two analysis aimed to identify experimental signals from the extremely hot and dense matter expected to be produced in ultra-relativistic heavy-ion collisions. One is based on fluctuations studies in Kaon to pion (K/π) ratio on event-by-event basis in central Cu+Cu interactions at $\sqrt{S_{NN}} = 62.4$ and 200 GeV recorded by Time Projection Chamber (TPC) and another one is study of photon pseudorapidity distributions and their fluctuations in Cu+Cu interactions at $\sqrt{S_{NN}} = 62.4$ GeV collected by Photon Multiplicity Detector (PMD) in hybrid STAR experiment at RHIC, BNL, USA. The explored pseudorapidity region for TPC data is ± 1.8 , whereas PMD collected data in $2.3 \leq \eta \leq 3.8$ region.

6.1 Event-by-Event K/π Ratio Fluctuations

By Using particle identification by dE/dx in the STAR Time Projection Chamber (TPC) the strength of dynamical fluctuations is measured using the sigma dynamical (σ_{dyn}) and ν_{dyn} variables.

The strength of dynamical fluctuations in Cu+Cu interactions at $\sqrt{S_{NN}} = 62.4$ and 200 GeV are compared with the results reported by NA49 in Pb+Pb collision at $\sqrt{S_{NN}} = 6.3, 7.6, 8.8, 12.3$ and 17.3 GeV and STAR in Au+Au collision at $\sqrt{S_{NN}} = 20, 62.4, 130,$ and 200 GeV. NA49 results indicate strong decrease in the dynamic fluctuation component with increase in the beam energy, whereas our results for Cu+Cu collisions shows energy independence. No dependence of $\sigma_{dyn}(\%)$ is seen also on the size of the colliding system in STAR experiment.

Also the experimentally observed strength of dynamical fluctuations is compared with Torreiri Statistical Hadronization (SH) model. It is observed that corresponding to equilibrium ($\gamma_q = 1$) scenario, the fluctuations strength underestimate the experimental results at all energies, while corresponding to non-equilibrium ($\gamma_q > 1$) scenario the SH model predictions are consistent at the higher energies only.

The strength of dynamical fluctuations is measured by making use of ν_{dyn} variable for Cu+Cu interactions at $\sqrt{S_{NN}} = 62.4$ and 200 GeV. We observed that the variation of $\nu_{dyn}(K\pi)$ for both the energies are consistent within the systematic errors and shows energy independence of the colliding system. It is also observed that the fluctuations strength measured by ν_{dyn} variable decreases with increasing centrality. This is due to the fact that the correlation strength gets diluted at higher multiplicity environment.

The centrality dependence of K/π fluctuations signal for Cu+Cu interactions at $\sqrt{S_{NN}} = 62.4$ and 200 GeV as characterized by the variable $\nu_{dyn}(K/\pi)$ seems to scale better with pseudorapidity density ($dN/d\eta$) than number of participant nucleons (N_{part}).

In contrast to experimental results, HIJING model predictions over-predicts the ob-

served signal of fluctuations, whereas the the AMPT (HIJING + re-scattering) is in better agreement with the experimental measurement.

6.2 Photon Pseudorapidity Distributions

The Photon Multiplicity Detector (PMD) at RHIC in STAR experiment is capable of detecting the photons in forward rapidity region. By making use of this capability we studied the photon pseudorapidity distributions in Cu+Cu interactions at $\sqrt{S_{NN}} = 62.4$ GeV in the forward rapidity ($2.3 \leq \eta \leq 3.8$) region for different centrality classes. The centrality wise particle density of photon is found to decrease as we scan pseudorapidity window from $\eta = 2.3$ to $\eta = 3.8$ in steps of $\eta = 0.2$ units.

The experimentally observed photon pseudorapidity distributions is compared with the theoretical predictions (HIJING model). HIJING predictions are not satisfactory with the experimental results, not only that estimations of pseudorapidity density of photons from HIJING are consistently lower than experimental values. However, for more central collisions the comparison is reasonably comfortable and becomes worse for peripheral collisions.

The measured photon pseudorapidity distributions is characterized in terms of collision centrality expressed in terms of number of participating nucleons (N_{part}). It is seen that the variations in photon multiplicity per participant pair is consistent with model predictions only for more central events. The incompatibility of data with model predictions increases with increase in impact parameter. It is seen that the photon yield in the forward rapidity region normalized to per participant pair is independent of centrality.

Energy and system size dependence of photon pseudorapidity distribution scaled to the number of participating nucleons as a function of $\eta - Y_{beam}$ is studied. It is observed that photon production in Pb+Pb interactions at SPS, Au+Au and Cu+Cu interactions at RHIC are consistent with each other, suggesting that photon production follows an energy as well as system independent limiting fragmentation behaviour.

The strength of dynamical fluctuations in the production of photon multiplicity in Cu+Cu interaction at $\sqrt{S_{NN}} = 62.4$ GeV is characterized by using the variable ν_{dyn} . It is found out that strength of fluctuation signal gets diluted in high multiplicity environment. We also observed scaled $\nu_{dyn}(\gamma_1\gamma_2)*dN/d\eta$ increases with increases pseudorapidity density ($dN/d\eta$) quickly, and saturate at higher pseudorapidity density ($dN/d\eta$).

6.3 Summary

Measurement of multiplicity distributions and its fluctuations have been carried out in Cu+Cu collisions at $\sqrt{S_{NN}} = 62.4$ and 200 GeV. The contributions from dynamical fluctuations gauged through the parameters studied have found to be very small. The models incorporating the re-scattering have been seen to better explain the experimental results.

The analysis has resulted in useful experimental observations which can be used as input to the models leading to the better understanding of physics of collision of ultra-relativistic heavy-ions.